



# UNIVERSITY OF TWENTE.

Faculty of Engineering Technology

*Document number: 382*

## Computational modelling of flow in the liver vasculature using the Lattice Boltzmann method to study microsphere distribution

Jan L. Van der Hoek

M.Sc. Thesis

21<sup>st</sup> July, 2021

---

**Supervisor:**  
dr. K. Jain

Engineering Fluid Dynamics Group  
Faculty of Engineering Technology  
University of Twente  
P.O. Box 217  
7500 AE Enschede  
The Netherlands

---

# Abstract

Radioembolization is a non-ablative selective procedure that is used for the treatment of advanced stage liver cancer and liver metastases. In this procedure, radioactive microspheres are administered to blood flow in the liver arteries by catheter injection, which embolize in narrower vessels near the malignant tissue. This study focusses on radioembolization in the right hepatic artery with Holmium-166 microspheres. More insight into microsphere distribution and factors that could influence this can improve Holmium-166 radioembolization and enhance patient lives.

The Lattice-Boltzmann method is used to study flow in a simplified model of the right hepatic artery. The Lattice-Boltzmann method is a CFD method that originates from statistical mechanics, in which a version of the Boltzmann transport equation is solved. The method is very suitable for simulating flow in complex geometries and with its high parallelization capabilities, interest in the method is increasing with the ongoing evolution of High Performance Computing (HPC). The general flow distribution is predicted in this study by analysing the flow behaviour during the cardiac cycle. Flow results are obtained that are in agreement with in-vitro experimental work that is also conducted at the university. A foundation is laid for future research on the behaviour and distribution of active particles like the Holmium-166 microspheres, with initial results showing that some particle distributions can already be predicted using simulations.

Next to the flow behaviour analysis, a qualitative study into catheter injection has been conducted by analysing the impact of catheter angle and injection location. In the analysis it is shown that the catheter setup changes the streamlines. It is expected that the catheter setup will have a large impact on the distribution of microspheres.

**Keywords:** Lattice Boltzmann Method; Radioembolization; Right Hepatic Artery; Computational Fluid Dynamics; Musubi; Streamlines; Distribution Maps; Catheter Injection;

# Acknowledgements

In the last year of working on this thesis, I have received a lot of support and assistance. Especially with the circumstances regarding Covid-19 I couldn't have wished for better support. In this computational work you don't work closely to a lot of people, which makes the collaboration that you do have even more invaluable. First, I want to thank my supervisor Kartik Jain for all of his advice, dedication and kind words throughout this project. In the early stages in particular your expertise helped me a lot in understanding the problems, but also later your insights helped me to not get confused by all the information and to maintain an overview. Your quick insights on Teams together with the regular meetings have really defined the shape of this thesis. But most importantly, your friendly and kind words during this period really kept my spirits up!

Next I would like to thank everyone involved in the ULTIMO project. Although the meetings only took place once a month, I really looked forward to these meetings and I got a lot of motivation from them. The feedback, discussions and presented work from others have been helpful and it feels special to have contributed to such a large project on radioembolization. A special thank you to Hadi Mirgolbabaee, Romaine Kunst, Tim Bomberna and Nathalie Saikali, who are also part of this project and provided the experimental and simulation results that I have also used in this thesis.

Last but not least, I want to thank my family, housemates and friends for all their support. My parents, for always staying positive and helping me put things into perspective. My older brother and twin brother Steffen and Evert, for always being there for me and providing the distraction, both desired and undesired. All of my housemates, for the distraction but also for listen to whatever I had to say about the thesis and being my rubber duck. Bram, Sietse and Nina, working and finishing our theses together at the University has been so valuable for me, I am so grateful! Also a special thanks to Harold, for reading some of my work and of course for the many (online) breaks that we had! Also a big thank you to Maarten, Ruben, Siepel, Gerben and Fausto for your support.

# Nomenclature

## Abbreviations

BTE	Boltzmann Transport Equation
CFD	Computational Fluid Dynamics
CRC	Colorectal Cancer
CT	Computed Tomography
FEM	Finite Element Method
FVM	Finite Volume Method
GUI	Graphical User Interface
HCC	Hepatocellular Carcinoma
LBM	Lattice Boltzmann Method
MD	Molecular Dynamics
MRI	Magnetic Resonance Imaging
PDE	Partial Differential Equation
RHA	Right Hepatic Artery
SIRT	Selective Internal Radiation Therapy
SPECT	Single Particle Emission Computed Tomography

## Physical parameters

$\mu$	Dynamic viscosity	$[Pa \cdot s]$
$\nu$	Kinematic viscosity	$[m^2/s]$
$\nu_L$	Kinematic lattice viscosity	$[-]$
$\omega$	Collision frequency	$[-]$
$\omega_i$	Weight factor	$[-]$
$\rho$	Density	$[kg/m^3]$
$\tau$	Relaxation factor	$[-]$
$c$	Lattice velocity	$[-]$
$c/\mathbf{u}$	Velocity	$[m/s]$
$c_s^2$	Lattice speed of sound	$[-]$
$F$	Force	$[N]$
$f$	Distribution function	$[-]$

$f^{eq}$	Equilibrium distribution function	[-]
$k_B$	Boltzmann constant	[s]
$L$	Length of the model	[m]
$m$	Mass	[kg]
$N$	Number of elements	[-]
$N_A$	Avogadro's number	[1/mol]
$P$	Pressure	[Pa]
$R$	Gas constant	[J/(K · mol)]
$r$	Radial position	[m]
$R_{sp}$	Specific gas constant	[J/(kg · K)]
$Re$	Reynolds number	[-]
$T$	Temperature	[K]
$t$	Time	[s]
$u$	Macroscopic velocity	[m/s]
$u_L$	Lattice velocity	[-]

# Contents

Nomenclature	4
<b>1 Introduction</b>	<b>8</b>
1.1 Research question	9
1.2 Scope	9
1.3 Approach	9
1.4 Outline	10
<b>2 Lattice Boltzmann Method</b>	<b>11</b>
2.1 Kinetic theory of gases	12
2.2 Boltzmann Transport Equation	13
2.3 The BGK approximation and Maxwell-Boltzmann distribution function	15
2.4 Discretization: lattice elements	17
2.5 Boundary condition	22
2.6 Chapman-Enskog expansion	24
<b>3 Biomedical background of the liver and radioembolization</b>	<b>28</b>
3.1 Human liver anatomy and physiology	28
3.2 Liver cancer: statistics, types and treatment	32
<b>4 The APES Simulation Framework</b>	<b>34</b>
4.1 Mesh generation: Seeder	35
4.2 Musubi: the Lattice Boltzmann solver	36
4.3 Code execution: High Performance Computing	38
<b>5 Preliminary pipe flow studies</b>	<b>39</b>
5.1 Pipe flow with a circular cross section	39
5.2 Pipe flow with a rectangular cross section: steady flow	43
<b>6 Right Hepatic Artery: models, results and analysis</b>	<b>51</b>
6.1 Experimental setup	51
6.2 Wide angle liver vasculature model	53
6.3 Wide angle liver vasculature model, corrected geometry	59
6.4 Small angle liver vasculature model	65
6.5 Small angle liver vasculature model, boundary correction	71
<b>7 Catheter injection: a qualitative study</b>	<b>83</b>
7.1 Catheter specifications and modelling	83
7.2 Catheter injection simulation results	85
<b>8 Discussion, conclusions and recommendations</b>	<b>95</b>
8.1 Discussion	95
8.2 Conclusions	97
8.3 Recommendations	98
<b>A Right Hepatic Artery: initial wrong results</b>	<b>105</b>
<b>B Right Hepatic Artery: more scalar and vector field results</b>	<b>107</b>

**C Comparison to Ansys Fluent simulation results 111**  
**D Catheter study: more results 112**

# Chapter 1

## Introduction

Primary liver cancer is the fifth most common cancer worldwide and the second leading cause of cancer mortality [1]. Surgical resection of the liver tumour is preferable and shows an increase in survival rate and life expectancy, however this is not always possible. Only 30% of patients with this diagnosis is eligible for surgery, so a large group still relies on alternatives [2]. Next to the primary form of liver cancer, a large group of cancer patients is diagnosed with secondary liver cancer, or liver metastases, with a median survival rate of less than 8 months [3] [4]. Due to its location, size and amount of metastases, only 15% of patients with this prognosis is eligible for surgical resection. The group of patients diagnosed with non-resectable primary and secondary type liver cancer is increasingly treated with the loco-regional therapy called radioembolization [5]. Radioembolization is a non-ablative selective procedure in which radioactive microspheres are administered to blood flow in the liver arteries by catheter injection, which embolise in narrower vessels near the malignant tissue. Radioembolization is minimally invasive and most of the healthy tissue is spared, which makes this the preferred treatment type if the outcomes are favourable with respect to other treatments.

A better understanding of the flow behaviour and the flow distribution could form the basis for improving microsphere distribution in radioembolization. This improved distribution knowledge can contribute to enhance anti-tumour efficacy and could reduce nontarget embolization, which is defined as the unintentional delivery of microspheres, mostly to extrahepatic regions [6]. For the prediction of microsphere distributions, a pre-treatment in-vivo simulation is currently applied with surrogate particles. The comparison of pre-treatment predictive and post-treatment measured dosimetry shows some good results [7]. However, changes in hemodynamics and catheter setup still result in a difference between the two procedures. Patient specific in-silica simulations are non-invasive and allow more freedom in optimising the distribution, which might improve or even replace the pre-treatment procedure in the future.

In most radioembolization procedures yttrium-90 microspheres are used, which have proved to extend the life expectancy of patients where surgery is not an option [8]. From a medical imaging perspective, microspheres of a new type have been developed at the University Medical Center Utrecht (Utrecht, Netherlands) that are visible by other imaging techniques. These particles consist of Holmium-166 which are highly paramagnetic, a property that makes the particles visible by MRI [9]. While yttrium-90 particles only emit beta radiation, holmium-166 microspheres also emit gamma radiation which allows for gamma scintigraphy imaging. The particle behaviour for both particles is still unknown and should be studied to improve radioembolization outcomes. In practice, many other uncertainties in the procedure still exist regarding the catheter type, configuration and method of injection with respect to timing and applied pressure.

In this thesis work, flow in a representation of the Right Hepatic Artery will be analysed using the Lattice Boltzmann Method. The Lattice-Boltzmann method is method for CFD that originates from statistical mechanics, in which a version of the Boltzmann transport equation is solved. Compared to other more conventional CFD methods that solve the Navier-Stokes equations like the Finite Element Method or Finite Volume Method, the Lattice Boltzmann Method offers great capabilities for the simulation of flow in complex geometries. The method makes use of a structured grid and allows for fast simulations on fine grids using High Performance Computing, which makes flow simulations in accurate representations of vasculature networks possible. With the ongoing improvements in High Performance Computing, the relatively simple algorithm used in the Lattice Boltzmann Method gives a high degree of parallelisation, an important aspect in the possibility of using multiple cores for simulations. Due to its origin from statistical mechanics, the Lattice Boltzmann Method also offers relatively easy ways to implement particle coupling which will be interesting

for future research in this project and also substantiates the choice of the Lattice Boltzmann Method for this preliminary numerical work.

## 1.1 Research question

The central research question in this report states: *To what extent can we predict and identify the clinical aspects that influence the microsphere distribution in the liver vasculature using computational modelling?* Several sub questions are stated below to help answer the main research question:

1. How does the Lattice Boltzmann Method compare to in-vitro experiments conducted on the same model?
2. Can computational modelling be used to identify aspects that influence microsphere distribution?
3. Can the microsphere distribution be predicted by using pure flow streamlines?
4. What is the influence of the position of the catheter on the deviations in flow streamlines?

## 1.2 Scope

In this thesis, the microsphere distributions are predicted by studying the flow in a simplified Right Hepatic Artery model. The simplified model could serve as a foundation for studies on other vascular networks near the liver or near other surrounding organs, as long as the dimensions of the vessels are roughly the same. Results in this thesis could aid in the improvement of both holmium-166 radioembolization as well as yttrium-90 radioembolization. Also, research on similar loco-regional therapies with intra-arterial drug administration, like intra-arterial chemotherapy might benefit from the results in this report.

This thesis is conducted in the context of the ULTIMO project. In-vitro experiments are conducted on the same models at the University of Twente, which are used for comparison. At Ghent University, in-silica simulations are performed using Ansys Fluent on the same models, which are also used for comparison.

## 1.3 Approach

The approach consists of various steps that are required to answer the research questions. First, the Lattice Boltzmann Method is studied to develop the required knowledge to run the simulations with the software package Musubi. The literature study in the thesis consists of the Lattice Boltzmann Method analysis and the radioembolization treatment analysis. The latter also includes a study on the liver anatomy and physiology, which is required to understand radioembolization treatment of liver tumours. Next to the literature study, a couple of benchmark cases are studied for which the analytical solutions are known. By practising with the software and analysing the results, characteristics in simulations and results can be identified and the simulation software is tested. Also, some initial findings might already give a part of the answer on research question 2. The main part of this thesis consists of the flow simulations and analysis of the simplified liver vasculature model. With these results, questions 1, 2 and 3 can be answered. Lastly, a qualitative catheter study will be conducted to answer question 4.

## 1.4 Outline

The outline roughly follows the steps mentioned in the approach, with each step as a separate chapter. The literature study consists of two chapters, the theory of the Lattice Boltzmann Method in chapter 2 and the theory of the anatomy and physiology of the liver together with radioembolization statistics and characteristics in chapter 3. In chapter 4, the used software in this thesis and some important aspects of the implementation of the simulation theory are discussed. To develop more insight into these simulations, a preliminary study on pipe flow is conducted, which can be found in chapter 5. Chapter 6 contains most of the results that can answer the research questions and it can be seen as the main work in this thesis. The model is expanded in chapter 7, where a catheter is added to the model and the impact is examined. In the closing part of this thesis, chapter 8, the discussion, conclusions and recommendations can be found.

## Chapter 2

# Lattice Boltzmann Method

The Lattice Boltzmann Method (LBM) is a relatively new Computational Fluid Dynamics (CFD) method. Most of its development only started about 20 years ago, but its use has rapidly increased due to some of the advantages it has over conventional CFD methods like Finite Element Methods (FEM) and Finite Volume Methods (FVM). One of the biggest advantages of the method is that it allows for a high level of parallelization, which means that the problem can be split into multiple domains which can be solved separately. While the amount of computations can be much higher than for another method, the algorithm that is used in LB methods is a bit simpler than in other methods and thus computations are faster. The method also has a high potential for parallelization due to the nature of the algorithm, which can give relatively fast LB simulations by using multiple CPU cores.

The derivation of the LBM comes from a different approach of solving the transport equations of mass, momentum and heat. A blob of fluid can be considered to be a continuum, where the individual particles are not considered. By applying the conservation laws on an infinitesimal control volume, sets of Ordinary Differential Equations (ODE) or Partial Differential Equations (PDE) are obtained, a famous example being the Navier-Stokes equations [10]. This continuous approach results in a problem on macroscopic scale. One can imagine that this works for many problems, however problems do exist where the assumption of a continuum could form a problem, for example when inter molecular interactions play a more dominant role.

A discrete approach considers the separate particles, resulting in a complete change of physics. For each particle, the location and velocity are considered and the system is solved by applying momentum conservation for the collisions between molecules and the boundaries. On this microscopic scale, macroscopic properties like pressure and temperature do not exist explicitly, but are derived from the kinetic energy of the particles. Simulation methods that use these principles are called Molecular Dynamics (MD) methods. Inter molecular interactions are now taken into account, which should mean that an even broader range of problems could be solved with such methods compared to the conventional CFD methods. One of the largest disadvantages of these methods is however the scale. For macroscopic problems, these methods are computationally-wise too demanding, since computations for all the individual particles are required. Here, a typical time step is of the order femto seconds ( $10^{-15}$  s) and the total simulation time is of the order pico seconds ( $10^{-12}$  s) [11].

Now, what if we would like to solve a problem at macroscopic scale, but still desire the advantages that a particle interaction approach gives us? One of the possible solutions is applying statistical mechanics to the transport equations, which was done by Ludwig Boltzmann. He derived the Boltzmann transport equation, which forms the basis of Lattice Boltzmann Methods. In this chapter, the derivations and assumptions are given which eventually give us the framework for the Lattice Boltzmann Method. A single particle will be analysed in section 2.1, which forms the basis of most molecular dynamics methods. Then in section 2.2, it will be shown that using statistical mechanics, an equation for the whole system can be obtained called the Boltzmann Transport Equation (BTE). While this equation can be used for some applications, its discrete variant is better applicable. The derivation of this discrete equation is given in section 2.3. This discretization only works for a special type of elements called lattice elements. The basic principles of these elements and the resulting equations are given in section 2.4. The last part in this chapter will give the relation between the discrete BTE and the Navier-Stokes equations by using the Chapman-Enskog expansion, which shows that the obtained equation is indeed capable of producing similar results to conventional CFD methods regarding incompressible flow problems.

## 2.1 Kinetic theory of gases

In the introduction of this chapter, it was already stated that the Lattice Boltzmann Method uses statistical mechanics to describe fluid behaviour. Before statistical mechanics are applied, a system is considered from a particle or molecular perspective. We consider a particle that is moving in free space, that obeys the conservation laws. One of the conservation laws is conservation of momentum, also known as Newton's second law:

$$\mathbf{F} = m \frac{d\mathbf{c}}{dt} = m \frac{d^2\mathbf{r}}{dt^2} \quad (2.1)$$

In the equation,  $F$  is the applied force,  $m$  is the mass of the particle,  $c$  is the velocity vector and  $r$  is the position vector. Now, we consider a particle at a position  $r$  with a velocity  $c$  at a time instant  $t$  that is subjected to a force  $F$  at that time instant. In figure 2.1 the result for the position and velocity vectors can be seen.

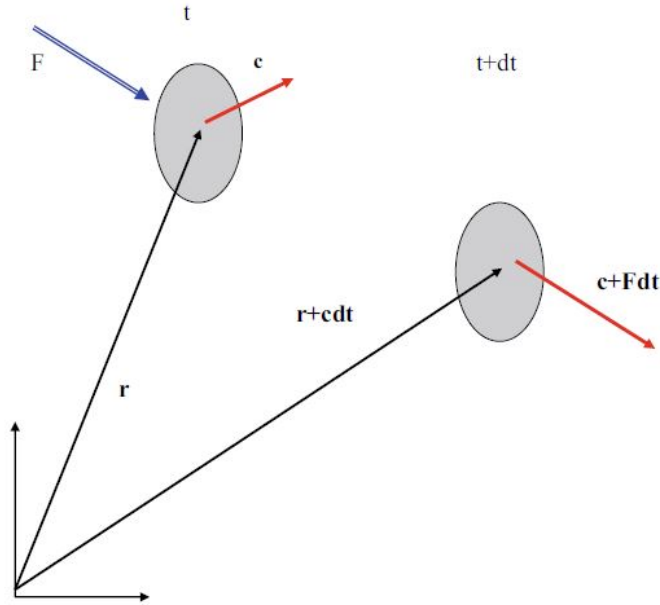


Figure 2.1: Position and velocity vector of a particle subjected to a force [12]

This is already the basis for MD methods. For each particle in the system, only the position and velocity vectors have to be saved. This representation is called phase space. Together with the information of the particles, like molecular structure, size and mass, we have sufficient information to macroscopic values like the temperature and pressure. It can be shown that the pressure  $P$  is linked to the kinetic energy of the particles, see equation 2.2.

$$P = \frac{2}{3} \tilde{n} E_{kin} \quad (2.2)$$

In the equation,  $\tilde{n}$  is the number of particles per unit volume and  $E_{kin}$  is the kinetic energy given by equation 2.3. In the equation,  $c$  is the total velocity, which is the sum of the squared velocities in all three spatial directions.

$$E_{kin} = \frac{1}{2}mc^2 \quad (2.3)$$

The kinetic energy on the microscopic level can also be used to obtain the temperature. For example for a gas, the assumption of an ideal gas relates the kinetic energy to the temperature, as can be seen in equation 2.4. If the amount of interactions between particles is too high, a result at high pressure, then the ideal gas law does not hold [13]. Also, the type of interactions is important for the validity of the law: only particle collisions are taken into account. If other interactions become more dominant, the law does not hold, which happens at low temperatures. This is however only a problem in extreme cases, for normal room temperature conditions the equation results in the following relation:

$$T = \frac{2E_{kin}}{3k_B} = \frac{mc^2}{3k_B} \quad (2.4)$$

Where  $k_B$  is the Boltzmann constant, which is related to the gas constant  $R = 8.314 \text{ J} \cdot \text{K}^{-1}\text{mol}^{-1}$  and Avogadro's number  $N_A = 6.02214 \cdot 10^{23}\text{mol}^{-1}$ .

$$k_B = R/N_A = 1.38 \times 10^{-23} \text{ J/K} \quad (2.5)$$

The full derivations are left out here, the equations are given to show that it is possible to link the particles with only momentum conservation to macroscopic quantities. However, this is an impossible task for many types of problems if the information of all particles is required to obtain a solution. Now, it turns out that in many cases the information from the individual particles is not required to acquire accurate macroscopic quantities. By introducing statistical mechanics, the number of computations can be reduced drastically, which results in a more feasible method that still has some of the advantages of this particle perspective approach. This approach forms the basis of the Boltzmann transport equation, which will be derived in the next section.

## 2.2 Boltzmann Transport Equation

Like the Navier-Stokes equations in CFD, the discrete version of the Boltzmann Transport Equation (BTE) is the workhorse in LBM simulations. The continuous variant of this equation can be derived by taking a statistical approach for describing a system. In the equation, a distribution function is solved that describes the state of the particles in the system. This distribution function is a type of Probability Density Function (PDF), which is a function of the six variables that are saved in the phase state (three position components and three velocity components), and the time.

We again consider the two states of a particle that were discussed in the particle kinetics theory (section 2.1), that is before and after being subjected to a force. These two states are given by figure 2.1. From this figure, we will now take a look at a group of particles, which can be represented by the distribution function. The distribution of molecules before and after applying the force is the same, but only if no collisions take place. This gives the following conservation equation, where a distribution function  $f$  is introduced to include all the particles in the system:

$$f(\mathbf{r} + \mathbf{c}dt, \mathbf{c} + \mathbf{F}dt, t + dt) d\mathbf{r}d\mathbf{c} - f(\mathbf{r}, \mathbf{c}, t) d\mathbf{r}d\mathbf{c} = 0 \quad (2.6)$$

In the equation, the function  $f$  is a function of the position  $r$ , the velocity  $c$  and the time  $t$ . If collisions do take place, we do not have an equilibrium. Instead, the right hand side becomes equal to the collision operator, denoted by  $\Omega$ , which also depends on the chosen distribution function.

$$f(\mathbf{r} + \mathbf{c}dt, \mathbf{c} + \mathbf{F}dt, t + dt)d\mathbf{r}d\mathbf{c} - f(\mathbf{r}, \mathbf{c}, t)d\mathbf{r}d\mathbf{c} = \Omega(f)d\mathbf{r}d\mathbf{c}dt \quad (2.7)$$

Dividing this equation by  $d\mathbf{r}d\mathbf{c}dt$  and taking the limit  $dt \rightarrow 0$  yields the total rate of change for the distribution function:

$$\frac{df}{dt} = \Omega(f) \quad (2.8)$$

Since the distribution function is a function of variables in the phase state, which means we can expand the rate of change and express it in multiple components:

$$\frac{df}{dt} = \frac{\partial f}{\partial \mathbf{r}} \frac{d\mathbf{r}}{dt} + \frac{\partial f}{\partial \mathbf{c}} \frac{d\mathbf{c}}{dt} + \frac{\partial f}{\partial t} = \Omega(f) \quad (2.9)$$

In this equation, the derivative of the position  $r$  with respect to time is the velocity  $c$  and the derivative of the velocity with respect to time is the acceleration, which is rewritten by using Newton's second law. This yields the Boltzmann Transport Equation:

$$\frac{\partial f}{\partial t} + \mathbf{c} \cdot \frac{\partial f}{\partial \mathbf{r}} + \frac{\mathbf{F}}{m} \cdot \frac{\partial f}{\partial \mathbf{c}} = \Omega(f) \quad (2.10)$$

The above equation is the general form of the BTE, with external forces. For the remaining derivations in this chapter, we will use a form of the BTE without external forces. In the discretized version of the equation, most cells are in general not subjected to external forces, which substantiates this choice of representing the general equation. The equation without external forces is given by equation 2.11, where the  $\frac{\partial f}{\partial \mathbf{r}}$  term is rewritten by using the  $\nabla$  (nabla) operator:

$$\frac{\partial f}{\partial t} + \mathbf{c} \cdot \nabla f = \Omega(f) \quad (2.11)$$

In this equation, the collision function  $\Omega$  should be known if the equation is to be solved. If this function is known, the equation can be solved for the distribution function  $f$ . Then, macroscopic quantities can be obtained from this equation, like the density and velocity of the fluid:

$$\rho(\mathbf{r}, t) = \int m f(\mathbf{r}, \mathbf{c}, t) d\mathbf{c} \quad (2.12)$$

$$u(\mathbf{r}, t) = \frac{1}{\rho(\mathbf{r}, t)} \int m \mathbf{c} f(\mathbf{r}, \mathbf{c}, t) d\mathbf{c} \quad (2.13)$$

However, these macroscopic quantities can only be obtained in this way if equation 2.11 can be solved analytically. This mainly depends on the analytical solution possibilities for the collision function, which is an integro-differential function. For some very specific cases it is possible to do this and comprehensive and complex papers have been written on these subjects [14][15][16]. This is interesting mainly from a mathematical perspective and not useful for most engineering applications.

From a practical and engineering perspective, the discrete version of this equation is much more interesting. The discrete version of the equation can be derived by approximating the collision function  $\Omega$ . In the next section, the collision function will be addressed by introducing the Bhatnagar, Gross and Krook (BGK) approximation. The approximation makes use of a known distribution function for particles in equilibrium,

which can be chosen depending on the problem that has to be solved. In this thesis, incompressible fluid flows are solved, which make use of a specific equilibrium distribution function called the Maxwell-Boltzmann distribution function, which will also be discussed in the next section.

## 2.3 The BGK approximation and Maxwell-Boltzmann distribution function

In the transport equation, the collision function  $\Omega$  is a very complicated function, which makes it difficult to solve the equation. A simple approximation was made by Bhatnagar, Gross and Krook (BGK), which replaces the collision function with a term that suffices for single phase flows. The approximation eventually makes the BTE solvable, while the simplicity of the approximation results in a discretized version of the equation that is able to give accurate results.

$$\Omega = \frac{1}{\tau} (f^{eq} - f) = \omega (f^{eq} - f) \quad (2.14)$$

In the equation,  $\tau$  is the relaxation factor and  $\omega$  is the collision frequency. For the collisions, the difference between the local equilibrium distribution function  $f^{eq}$  and the actual distribution function  $f$  is taken for the collisions. If the difference between the two distributions is large, the term has a larger value, which means that more collisions take place in order to reach the equilibrium faster. The difference is multiplied by the relaxation frequency  $\omega$  which dictates how fast equilibrium is reached. This relaxation frequency can be seen as a form of viscosity: for lower values of  $\omega$ , equilibrium is reached slower and the fluid is more viscous. Another way to look at it is by comparing it to a proportional action in a PID controller. For a larger P action, the the system moves faster to the equilibrium, however this can also result in a larger overshoot and more severe initial fluctuations.

The local equilibrium distribution function  $f^{eq}$  that is used in the majority of LB simulations is the Maxwell-Boltzmann distribution function. For the derivation of this function, four assumptions are made regarding the behaviour of the particles [17][18]:

- The diameters of the molecules are much smaller than the distance between them.
- The collisions between molecules conserve energy.
- The molecules move between collisions without interacting, with a constant speed in a straight line.
- The position and velocities of the molecules are initially random.

From a particle perspective and by using these assumptions, the Maxwell-Boltzmann distribution function in equation 2.15 can be obtained. The Maxwell-Boltzmann distribution in this form is obtained by considering the speed instead of the velocity, which is the resultant of the individual components, or  $c = \sqrt{c_x^2 + c_y^2 + c_z^2}$ . In phase space, this corresponds to the surface area of a sphere which is  $4\pi c^2$ . The surface area of this sphere accounts for all particles with exactly that speed. This means that the Maxwell-Boltzmann distribution function describes the possibility of a particle being in a certain velocity state.

$$f^{eq}(c) = 4\pi c^2 \left( \frac{m}{2\pi k_B T} \right)^{\frac{3}{2}} e^{-\frac{mc^2}{2k_B T}} \quad (2.15)$$

In the equation,  $m$  is the mass of the molecule in  $[kg]$ ,  $T$  is the temperature of the system in  $[K]$  and  $c$  is the velocity of the particle in  $[m/s]$ . The Maxwell-Boltzmann distribution function depends on the

temperature of the system and the mass of the molecules. In figure 2.2, the distribution functions of both helium ( $u = 4 \text{ g/mol}$ ) and oxygen ( $u = 16 \text{ g/mol}$ ) at room temperature ( $T = 293\text{K}$ ) and at elevated temperature ( $T = 393\text{K}$ ) can be found, which is computed by using equation 2.15. The molecular mass  $u$  can be converted to the mass of one molecule by multiplying the molecular mass with Avogadro's number.

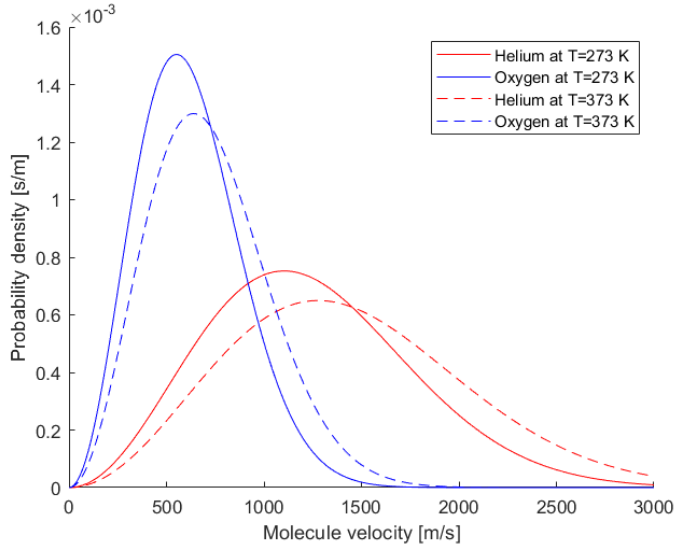


Figure 2.2: Distribution functions of Helium and Oxygen

In the figure, it can be seen that the mean velocity and the maximum velocity of helium are higher than those of oxygen. This is the expected result since generally lighter molecules move faster. The dimension of the probability density is in  $[s/m]$ , such that the area under any section of the curve is dimensionless [19].

The Maxwell-Boltzmann distribution function is the basis for the BGK approximation, which can replace the complex collision term in equation 2.11. With the BGK approximation, we get equation 2.16.

$$\frac{\partial f}{\partial t} + \mathbf{c} \cdot \nabla f = \omega (f^{eq} - f) \quad (2.16)$$

The left hand side of the equation represents the streaming process and the right hand side of the equation represents the collision process.

In the collision term,  $f^{eq}$  is a another form of the Maxwell-Boltzmann distribution function, where the individual components of the velocity are taken into account. To transform the equation, we consider the probability of finding a particle on a spherical shell with radius  $c$  and width  $dc$ . For the individual components, we then get the following transformation [20]:

$$f_{box}^{eq}(c_x, c_y, c_z) 4\pi c^2 dc = f_{sphere}^{eq}(c) dc \quad (2.17)$$

This transformation gives equation 2.18. Note that the velocity in the equation is now a vector.

$$f^{eq}(\mathbf{c}) = \left( \frac{m}{2\pi k_B T} \right)^{\frac{3}{2}} e^{-\frac{m\mathbf{c}^2}{2k_B T}} \quad (2.18)$$

Equation 2.18 is multiplied by the macroscopic density  $\rho$ , to scale the normalised distribution function and

make it specific for the system. When we consider a gas that has a non-zero macroscopic velocity, we obtain the equation below:

$$f^{eq} = \frac{\rho}{(2\pi R_{sp}T)^{3/2}} \exp\left(-\frac{(\mathbf{c} - \mathbf{u})^2}{2R_{sp}T}\right) \quad (2.19)$$

In the equation,  $R_{sp}$  is the specific gas constant in  $[\text{J kg}^{-1} \text{K}^{-1}]$ , given by the equation below:

$$R_{sp} = \frac{k_B}{m} \quad (2.20)$$

First, the exponential in equation is rewritten to allow for a Taylor expansion:

$$f^{eq} = \frac{\rho}{(2\pi R_{sp}T)^{3/2}} \exp\left(-\frac{\mathbf{c} \cdot \mathbf{c}}{2R_{sp}T}\right) \exp\left(\frac{2(\mathbf{c} \cdot \mathbf{u}) - \mathbf{u} \cdot \mathbf{u}}{2R_{sp}T}\right) \quad (2.21)$$

The second term in the equation is now approximated:

$$f^{eq} = \frac{\rho}{(2\pi R_{sp}T)^{3/2}} \exp\left(-\frac{\mathbf{c} \cdot \mathbf{c}}{2R_{sp}T}\right) \left[1 + \frac{2(\mathbf{c} \cdot \mathbf{u}) - \mathbf{u} \cdot \mathbf{u}}{2R_{sp}T} + \frac{(2(\mathbf{c} \cdot \mathbf{u}) - \mathbf{u} \cdot \mathbf{u})^2}{8(R_{sp}T)^2} + \dots\right] \quad (2.22)$$

Now, the substitution below is used to get rid of the exponential term:

$$W(\mathbf{c}) = \frac{1}{(2\pi R_{sp}T)^{3/2}} \exp\left(-\frac{\mathbf{c} \cdot \mathbf{c}}{2R_{sp}T}\right) \quad (2.23)$$

With some rewriting and ignoring all terms of order  $\mathcal{O}(u^3)$  in the approximation of the exponential, we get the second order accurate equilibrium distribution function that is most commonly used in the BGK approximation:

$$f^{eq} = \rho W(\mathbf{c}) \left[1 + \frac{2(\mathbf{c} \cdot \mathbf{u}) - \mathbf{u} \cdot \mathbf{u}}{2R_{sp}T} + \frac{(\mathbf{c} \cdot \mathbf{u})^2}{2(R_{sp}T)^2}\right] + \mathcal{O}(u^2) \quad (2.24)$$

With the equilibrium distribution function known, the collision term can now be discretized on its own, which allows for discretization of the full BTE. This discretization is done by using a special type of element, called a lattice element. In these elements, specific directions are defined for the flow directions. The discretization using these lattices and the results for a type of lattice will be explained and discussed in the next section.

## 2.4 Discretization: lattice elements

The BTE with the BGK approximation that is given by equation 2.16 can be discretized by introducing lattice elements. A lattice element is a unique kind of element that is used in LB methods, where possible directions of flow are determined by the type of lattice element. Lattice elements evolved from cellular automata, which offer some insights into the working of lattice elements. The working principles of cellular automata are well explained by Sukop et al., however they are however mainly interesting from a historical perspective and will not be discussed here. [21].

In a lattice element, discrete probability functions are used to indicate the probability of a particle moving in a certain direction with a microscopic velocity  $c$ . Lattice element type is denoted by  $DnQm$ , with  $n$  giving the dimension of the lattice and  $m$  giving the number of flow directions. The simulations that can be found in this report all use the same D3Q19 stencil. In this section, the 2 dimensional D2Q9 stencil given by figure 2.3 will be used as an example, which is better for visualisation purposes.

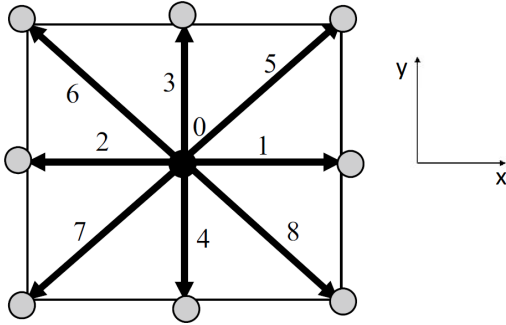


Figure 2.3: D2Q9 lattice arrangement [12]

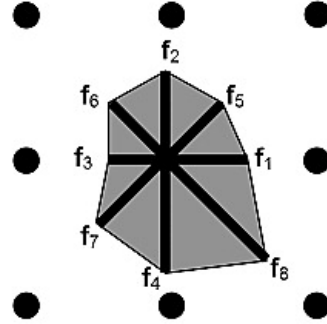


Figure 2.4: D2Q9 distribution function example [21]

In the figure, it can be seen that for this stencil 9 streaming directions are possible, where the streaming direction with index 0 indicates a particle at rest. The streaming directions are given by the discrete velocity vectors  $\mathbf{c}_i$ :

$$\mathbf{c}_i = \begin{cases} (0, 0) & i = 0 \\ (1, 0), (0, 1), (-1, 0), (0, -1) & i = 1, 2, 3, 4 \\ (1, 1), (-1, 1), (-1, -1), (1, -1) & i = 5, 6, 7, 8 \end{cases} \quad (2.25)$$

The discrete probability distribution function  $f_i$  can be seen as direction specific densities, or particle populations. An example of the distribution can be found in figure 2.4. Next to a discrete probability distribution function  $f_i$  for each streaming direction, a weight factor  $w_i$  is introduced. The weight factors for this stencil are given by equation 2.26.

$$w_i = \begin{cases} 4/9 & i = 0 \\ 1/9 & i = 1, 2, 3, 4 \\ 1/36 & i = 5, 6, 7, 8 \end{cases} \quad (2.26)$$

These weight factors are obtained from applying the rules that a lattice model has to obey. For this model, the equation is given by equation 2.27. The equation below has the same form as the equation for the moment of a probability distribution function, which will be used later in the Chapman-Enskog expansion in section 2.6. The moment is mentioned here to clarify that the equation below is not arbitrarily chosen and has a significance in statistical mechanics. For example, the zeroth and first order central moments of a PDF are equal to 1 and 0 respectively, by definition.

$$E^{(n)} = \sum_{i=0}^8 \omega_i c_{i,j_1} c_{i,j_2} \cdots c_{i,j_n} \quad (2.27)$$

This equation can be expanded for values of  $n$ , with the first 5 equations given below, where  $c_s$  is the lattice speed.

$$\begin{aligned}
E^{(0)} &= \sum_{i=0}^8 \omega_i = 1 \\
E^{(1)} &= \sum_{i=0}^8 \omega_i c_{i,j_1} = 0 \\
E^{(2)} &= \sum_{i=0}^8 \omega_i c_{i,j_1} c_{i,j_2} = c_s^2 \delta_{j_1 j_2} \\
E^{(3)} &= \sum_{i=0}^8 \omega_i c_{i,j_1} c_{i,j_2} c_{i,j_3} = 0 \\
E^{(4)} &= \sum_{i=0}^8 \omega_i c_{i,j_1} c_{i,j_2} c_{i,j_3} c_{i,j_4} = c_s^4 (\delta_{j_1 j_2} \delta_{j_3 j_4} + \delta_{j_1 j_3} \delta_{j_2 j_4} + \delta_{j_1 j_4} \delta_{j_2 j_3})
\end{aligned} \tag{2.28}$$

The first line in equation 2.28 gives the sum of the weight factors is equal to 1, which corresponds to both the definition of the zeroth order moment of a PDF and the definition of the sum of the weight factors. The second line can be seen as a symmetry condition, which is required for a balanced lattice element, where streaming directions do not have a preference. The second to fourth order moments are obtained by applying isotropy conditions to the lattice element. In the Navier-Stokes equations, isotropy of the environment is automatically conserved, as the physical properties that are independent of the orientation are also invariant by orthogonal changes in the spatial frame [22]. For a lattice element, this means that rotation of the lattice element by 90 degrees in an arbitrary direction around an axis should not change the result. It is known that the higher order isotropic tensor has the form of an 'isotropic delta function', which is the sum of Kronecker delta functions over all distinctive permutations of its sub-indices, by Chen [23]. In this paper, it is stated that full rotational symmetry is impossible for lattice element with a finite number of vectors. The choice of a lattice element is very important here, as it can guarantee isotropy up to a specific order. For the problems in the thesis, lattice elements that give up to fourth order isotropy suffice, which is the case for the used D3Q19 elements.

With the lattice elements, the discrete version of the BTE that is valid along these specific directions can be obtained, given by equation 2.29:

$$\frac{\partial f_i}{\partial t} + \mathbf{c}_i \cdot \nabla f_i = \omega (f_i^{eq} - f_i) \tag{2.29}$$

The equilibrium distribution function in the equation is now also discrete. The discrete distribution function can be derived from 2.24, which uses the substitution below:

$$c_s^2 = R_{sp} T \tag{2.30}$$

Here,  $c_s^2$  is the lattice speed of sound, which depends on the lattice element that is chosen and can be derived from equation 2.28. The general discrete equilibrium function is given by equation 2.31. In the equation, it is assumed that the basic speed on the lattice is  $1 \text{ lu ts}^{-1}$ .

$$f_i^{eq} = \rho w_i \left[ 1 + \frac{2(\mathbf{c}_i \cdot \mathbf{u}) - \mathbf{u} \cdot \mathbf{u}}{2c_s^2} + \frac{(\mathbf{c}_i \cdot \mathbf{u})^2}{2c_s^4} \right] + \mathcal{O}(u^2) \tag{2.31}$$

This approximation is again second order accurate. For both the D2Q9 and D3Q19 lattice elements, the lattice speed of sound is given by  $c_s^2 = 1/3$ . For these lattice elements, equation 2.32 is the equilibrium distribution function.

$$f_i^{eq} = \rho w_i \left[ 1 + 3(\mathbf{c}_i \cdot \mathbf{u}) - \frac{3}{2}(\mathbf{u} \cdot \mathbf{u}) + \frac{9}{2}(\mathbf{c}_i \cdot \mathbf{u})^2 \right] + \mathcal{O}(u^2) \quad (2.32)$$

For an incompressible fluid flow, the density is constant. It is however difficult to constrain the density in LB methods, which remains a topic of research [24]. One option is to replace the density by equation 2.33, proposed by He and Luo [25].

$$\rho = \rho_o + \delta\rho \quad (2.33)$$

In the equation, the average density of the fluid  $\rho_o$  is a constant, which is a fluid property. The  $\delta\rho$  term accounts for small density fluctuations. The incompressible equilibrium distribution function for the earlier mentioned two lattice types can now be written as equation 2.34.

$$f_i^{eq} = w_i \left[ \rho + \rho_o \left( 3(\mathbf{c}_i \cdot \mathbf{u}) - \frac{3}{2}(\mathbf{u} \cdot \mathbf{u}) + \frac{9}{2}(\mathbf{c}_i \cdot \mathbf{u})^2 \right) \right] + \mathcal{O}(u^2) \quad (2.34)$$

In most LB methods, the streaming step takes place first, followed by the collision step. This process is nicely visualized by Yuanxun Bill Bao & Justin Meskas [26]. The streaming step is given by the left hand side of equation 2.16, which can be found in figure 2.5.

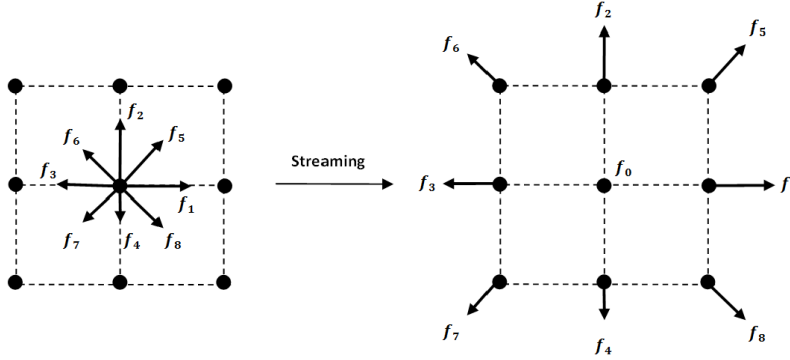


Figure 2.5: Streaming step for a D2Q9 lattice [26]

After the streaming step, the particles have moved in directions specified by the lattice, which is the new location if no collisions take place. Since the lattices are surrounded by other lattice elements and sometimes walls, collisions do take place. This means that the moving particles are initially in a sort of imaginary state, denoted by  $f_i^*$ . For the collision step, the information of the streaming step is used by calculating the macroscopic density and speed from this step. This can also be seen in equation 2.31, where the density  $\rho$  and the velocity  $u$  are the only unknowns in the equation. These macroscopic values can be calculated by using equations 2.37 and 2.38, which is a sum over all  $N$  streaming directions in the lattice. To derive these equations, we first take the mass and momentum conservation over the lattice for the discrete BTE [27]:

$$\sum_{i=0}^N f_i^{eq} = \sum_{i=0}^N f_i \quad (2.35)$$

$$\sum_{i=0}^N c_{i,j} f_i^{eq} = \sum_{i=0}^N c_{i,j} f_i \quad (2.36)$$

In equation 2.36, the vector  $\mathbf{c}_i$  is replaced by the vector components  $\mathbf{c}_{i,j}$ , since we have momentum conservation in all spatial dimensions. Now for the equilibrium distribution function, we can use equation 2.32 to obtain the equations for the density and velocity as a function of the calculated particle density functions. It is logical that the sum of the distribution functions is equal to the density, since the normalised Maxwell-Boltzmann distribution function was multiplied by the density in equation 2.19.

$$\rho = \sum_{i=0}^N f_i \quad (2.37)$$

$$\mathbf{u} = \frac{1}{\rho} \sum_{i=0}^N f_i \mathbf{c}_i \quad (2.38)$$

For the collision step, we have particle-particle collisions and particle-wall collisions. When looking at the streaming process, one could expect interactions between the distribution functions coming from neighbouring lattice elements. For example, we take the lattice element in figure 2.5 and imagine another lattice element on the right side of this element. If this lattice element has the same numbering convenience, a collision might be expected between distribution function  $f_1$  and  $f_3$ . The particle-particle collisions however take place inside the distribution function and the collisions can be seen as a purely local process. For a single-phase flow, the distribution functions are simply interchanged after the time step.

These local collisions are taken into account by the distributions moving to the local equilibrium. The new distribution functions are obtained by using the distribution function after the streaming step  $f_i^*$ .

$$f_i = f_i^* - \omega (f_i^* - f_i^{eq}) \quad (2.39)$$

For the particle-wall collisions, extra information is needed to calculate the updated distribution functions. These collisions are actually taken into account in the streaming step, which means that the collisions in the LB method are a bit different than for molecular dynamics models. At the walls, a boundary conditions is imposed that dictates how these collisions take place. These boundary conditions will be explained in the next section. In the BGK BTE version that is given in the report, the external force term is not included. The main reason for this is that in the problems in this report, external forces like the buoyancy, gravity or magnetic forces do not have to be applied to solve the problems. The impact on the derivations is often not treated in literature, however the complexity of the implementation of the external forces can become quite large depending on the problem [28].

One of the largest advantages of LB methods is the possibility for parallelization, which can be explained by the streaming and collision in each time step. The collisions take place locally, which means that interactions between the lattice cells only happen due to streaming. At the next time step, only the information from the direct neighbouring cells is required to update the distribution functions in the cell. The streaming and collision steps in the LB method can thus be solved separately for each element, before updating the cells based on the distributions coming from the neighbouring cells. This in turn allows for parallelization, since all elements can be computed separately, which is often done by dividing the tasks over multiple CPUs. Also, in Navier-Stokes based solvers like FEM and FVM, the pressure field has to be solved explicitly from a pressure Poisson equation. In equation 2.37 it can be seen that the density is derived locally. In LBM, the pressure and density are related by equation 2.40:

$$P = \rho c_s^2 \quad (2.40)$$

From this equation, it becomes clear that the pressure can be calculated from the density which means that the pressure Poisson equation does not have to be solved explicitly in LB methods.

## 2.5 Boundary condition

The equations that hold for the internal flows are explained. For the boundaries, various options exist that are able to fully describe the system that has to be solved. In this section, the bounce-back boundary condition and the Dirichlet boundary condition will be discussed. Other boundary conditions like the Neumann flux boundary condition can also be used to describe the behaviour at the walls and the inlets and outlets of a model. They are however used in specific cases and most basic simulations can be performed by using the two types of boundary conditions that are explained below.

### Bounce-back boundary condition

The simplest boundary condition that can be used in LB methods is the bounce-back condition. This condition is often used to describe the particle-wall collisions and while it is a simple condition, it is used very often in LB simulations. For this boundary condition, either the nodes on the boundary are used to describe the process, or additional nodes are generated behind the wall that act as storage nodes which gives a different bounce-back behaviour.

The process of bounce-back is quite straightforward, which can be seen in figure 2.6 for a southern solid boundary with a mid-plane bounce-back condition. In the first three images, one time step is shown near the boundary. The streaming process takes place from the first image to the second image and a sort of collision process takes place from the second image to the third image. The bounce-back condition can be seen as an alternative collision process where all the particle densities are reversed in direction by the wall. At the end of the time step, it can be seen in the figure that the particle densities are stored at the nodes in the wall. In the fourth image, the particle densities for the next time step after streaming are shown, which shows that the particles have been released from the wall and are now streaming in opposite direction.

The bounce-back condition that is described here is the mid-plane condition, where the solid boundary is exactly in between the node in the fluid node and the solid node. It is also possible to place the boundary at another location relative to the lattice, as shown in figure 2.7 [29].

The traditional bounce-back condition is obtained when the boundary plane coincides with A, however it has been shown that this gives first order behaviour for the error, or that the error reduces linearly with a decreasing mesh size [30]. The traditional bounce-back takes place after half the time step, which results in poorly described particle-wall collision for streaming directions  $c_4$ ,  $c_7$  and  $c_8$  in the figure. This can be fixed by changing the definition of the bounce-back, by for example changing the time instant at which the bounce-back takes place. Another option is to place the boundary plane

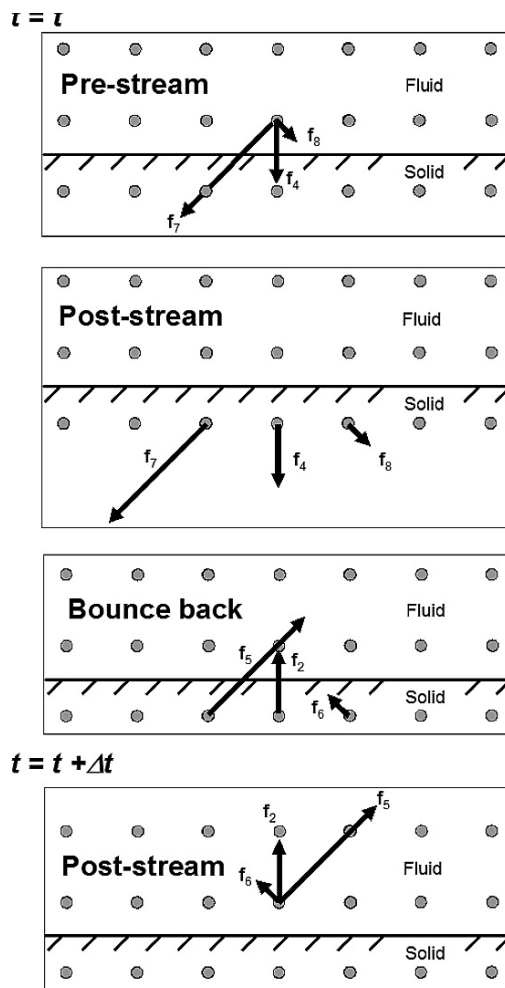


Figure 2.6: Collision process at the wall [21]

such that it coincides with B in the figure. It has been shown that placing the boundary condition at this location yields second order behaviour for the error. This bounce-back condition is referred to as the mid-plane bounce-back condition, or as the shifted bounce-back condition. This boundary condition can however not be implemented in all cases, but various other options exist that still ensure the global second order behaviour of the LB method if this is desired [30].

The bounce-back condition here is explained for the wall-particle collisions, however it is also possible to use this condition for some inlets and outlets. For example, the inlet velocity can be prescribed by using a bounce-back condition. Here the particle densities just before the bounce-back are prescribed in such a way, that with the bounce-back a prescribed velocity is achieved. The theory behind this condition is a bit more complex than the wall bounce-back condition. A simpler condition that can also be used for inlets and outlets is a Dirichlet boundary condition, which will be explained in the next paragraph.

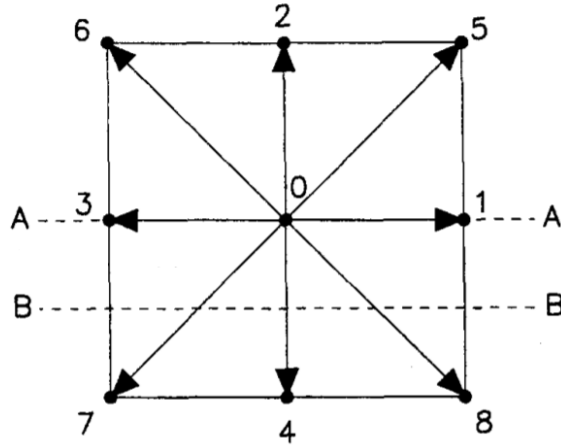


Figure 2.7: Options for the placement of the boundary for the bounce-back condition, adapted from Kim [29]

### Dirichlet boundary condition

The bounce-back condition is a very suitable boundary condition for the walls in a model and it can also be used for some types of inlets and outlets. An alternative that is also widely applied in LB methods is a Dirichlet boundary condition. Here, a value like the velocity, pressure or density is applied on a point, line or plane. For this, we consider a D2Q9 lattice element with a prescribed velocity at the southern boundary, which corresponds with the A plane in figure 2.7. The macroscopic density for this lattice element can be calculated by using equation 2.37:

$$\rho = f_0 + f_1 + f_2 + f_3 + f_4 + f_5 + f_6 + f_7 + f_8 \tag{2.41}$$

The momentum equations in  $x$  and  $y$  direction can be obtained from equation 2.38:

$$\rho u = f_1 + f_5 + f_8 - f_6 - f_3 - f_7 \tag{2.42}$$

$$\rho v = f_5 + f_2 + f_6 - f_7 - f_4 - f_8 \tag{2.43}$$

Also, we have an equilibrium over the boundary, which gives:

$$f_2 - f_2^{eq} = f_4 - f_4^{eq} \quad (2.44)$$

The fluid is considered incompressible, however the density  $\rho$  is still an unknown since incompressibility cannot be enforced. This means that there are four equations and four unknowns ( $f_2$ ,  $f_5$ ,  $f_6$  and  $\rho$ ). The other distribution functions are outward of the domain and are known and obtained from the streaming step. One could see this boundary condition as a response to the streaming step from the boundary. Using the equilibrium distribution function from equation 2.32, we obtain the following equations for the unknown variables:

$$\rho = \frac{1}{1-v} [f_0 + f_1 + f_3 + 2(f_4 + f_7 + f_8)] \quad (2.45)$$

$$f_2 = f_4 + \frac{2}{3}\rho v \quad (2.46)$$

$$f_5 = f_7 - \frac{1}{2}(f_1 - f_3) + \frac{1}{6}\rho v + \frac{1}{2}\rho u \quad (2.47)$$

$$f_6 = f_8 + \frac{1}{2}(f_1 - f_3) + \frac{1}{6}\rho v - \frac{1}{2}\rho u \quad (2.48)$$

Here, we can see that the unknowns at the boundary are fully defined by the given equations, so the Dirichlet boundary condition can be implemented in this way. For a given pressure at the boundary, which is often desired at outlets, the method is quite similar. For an incompressible flow, the change in pressure and density can be related by the lattice speed of sound, given by equation 2.40 [25].

This means that the velocity over the boundary is the only unknown in equations 2.41 to 2.44, which only requires a relation between the velocities  $u$  and  $v$  to solve, which is given by the geometry or angle of the boundary.

There are other options for boundary conditions, like the Neumann flux condition that is often used in diffusion problems. In this report, problems with incompressible fluid flows are solved, which means that the given boundary condition options will be used to fully define and solve the problems.

## 2.6 Chapman-Enskog expansion

Up to this point, many equations have already been derived or explained regarding the LB method. The purpose of these derivations is to show the assumptions and underlying theory on which the LB method is built. The topic of interest in this thesis is incompressible flow with a low Mach number. It seems that the derived equation should be able to produce results for such a flow problem, however proof of this is yet to be given. For other more conventional CFD methods, a certain set of PDEs is solved for such problems, which are called the Navier-Stokes equations. Now, it has been proven that the link between the BTE and the Navier-Stokes equations can be given by the Chapman-Enskog expansion [31] [27]. Next to the link between these two equations, it can also be shown that the parameters in the LB methods have to be chosen in a specific way to obtain physical results.

First, we will rewrite the discrete version of the BTE with the BGK approximation, given by equation 2.16. The particle density function  $f$  is a function of the time and the position vector  $\mathbf{r}$ .

$$f_i(\mathbf{r} + \mathbf{c}_i \Delta t, t + \Delta t) - f_i(\mathbf{r}, t) = \omega (f_i^{eq}(\mathbf{r}, t) - f_i(\mathbf{r}, t)) \quad (2.49)$$

First, the material derivative operator is introduced, given by equation 2.50. The material derivative operator is often used to track the change of a property in the field while moving with the flow.

$$\frac{D}{Dt} = \frac{\partial}{\partial t} + \mathbf{c}_i \cdot \nabla \quad (2.50)$$

Now equation 2.49 can be rewritten with a sum to infinity based on a Taylor expansion:

$$\sum_{n=1}^{\infty} \frac{\Delta t^n}{n!} \left( \frac{D}{Dt} \right)^n f_i(\mathbf{r}, t) = \omega (f_i^{eq}(\mathbf{r}, t) - f_i(\mathbf{r}, t)) \quad (2.51)$$

Before the Chapman-Enskog expansion can be introduced, the moments of the equilibrium distribution function  $f_i^{eq}$  are given. These equations can be derived from using the properties of the lattice model, given by equation 2.28. Here, we have  $j_1, j_2, j_3 \in [1, 2, 3]$  for a 3D model, accounting for the  $x$ ,  $y$  and  $z$  directions.

$$\begin{aligned} \sum_i f_i^{eq} &= \rho \\ \sum_i c_{i,j_1} f_i^{eq} &= \rho u_{j_1} \\ \sum_i c_{i,j_1} c_{i,j_2} f_i^{eq} &= c_s^2 \rho \delta_{j_1 j_2} + \rho u_{j_1} u_{j_2} \\ \sum_i c_{i,j_1} c_{i,j_2} c_{i,j_3} f_i^{eq} &= c_s^2 \rho (\delta_{j_1 j_2} u_{j_3} + \delta_{j_1 j_3} u_{j_2} + \delta_{j_2 j_3} u_{j_1}) \end{aligned} \quad (2.52)$$

Similar forms of the first two equations of these low-order moments were already given earlier for calculating the macroscopic values for the density and velocity (see equations 2.37 and 2.38). These equations for the equilibrium distribution function will be used later in the derivation of the incompressible Navier-Stokes equations. Now, the Chapman-Enskog expansion is introduced to allow expansion of the unknown particle distribution function and the time derivative:

$$f_i = \sum_{n=0}^{\infty} f_i^{(n)} \quad (2.53)$$

$$\frac{\partial}{\partial t} = \sum_{n=0}^{\infty} \frac{\partial}{\partial t_n} \quad (2.54)$$

In equation 2.51, each term is expanded separately and the terms are grouped based on the magnitude [32]. The magnitude in this sense is the order of the expansion. If one term is expanded once and another term is expanded once as well, the order of the expansion is 2. Expansion and ordering of the magnitudes gives the zeroth, first and second order magnitude equations below:

$$f_i^{(0)} = f_i^{eq} \quad (2.55)$$

$$\Delta t \left( \frac{D}{Dt} \right) f_i^{(0)} = -\omega f_i^{(1)} \quad (2.56)$$

$$\Delta t \left( \frac{D}{Dt} \right) f_i^{(1)} + \Delta t \frac{\partial}{\partial t_1} f_i^{(0)} + \frac{(\Delta t)^2}{2} \left( \frac{D}{Dt} \right)^2 f_i^{(0)} = -\omega f_i^{(2)} \quad (2.57)$$

In equation 2.57, the second term is the expanded material derivative. Now, the following assumption is made that still obeys the conservation laws of mass and momentum, or equations 2.37 and 2.38:

$$\sum_i f_i^{(n)} = 0, \forall n \neq 0 \quad (2.58)$$

$$\sum_i c_{i,j_1} f_i^{(n)} = 0, \forall n \neq 0 \quad (2.59)$$

Now, using the assumptions from equations 2.58 and 2.59 and the definition given by equation 2.55, equation 2.56 can be rewritten. Here the material derivative is written out for purpose of clarity.

$$\frac{\partial f_i^{eq}}{\partial t_0} + c_{i,j_1} \frac{\partial f_i^{eq}}{\partial r_{j_1}} = 0 \quad (2.60)$$

With this equation, equation 2.57 can also be rewritten using the assumptions again:

$$\frac{\partial f_i^{eq}}{\partial t_1} = 0 \quad (2.61)$$

The zeroth order moments of equations 2.60 and 2.61 can be obtained by taking the first equation in 2.52 as the basis, also using the other equations of the low order moments to rewrite the equilibrium distribution function:

$$\begin{aligned} \frac{\partial \rho}{\partial t_0} + \frac{\partial (\rho u_{j_1})}{\partial r_{j_1}} &= 0 \\ \frac{\partial \rho}{\partial t_1} &= 0 \end{aligned} \quad (2.62)$$

These two equations can be combined by using that  $\frac{\partial}{\partial t} = \sum_{n=0}^{\infty} \frac{\partial}{\partial t_n} \approx \frac{\partial}{\partial t_0} + \frac{\partial}{\partial t_1}$ , which gives the mass continuity equation of the incompressible Navier-Stokes equations:

$$\frac{\partial \rho}{\partial t} + \frac{\partial (\rho u_{j_2})}{\partial r_{j_2}} = 0 \quad (2.63)$$

The similar method can be used to obtain the first order moments of equations 2.60 and 2.61:

$$\begin{aligned} \frac{\partial (\rho u_{j_1})}{\partial t_0} + \frac{\partial}{\partial r_{j_2}} (c_s^2 \rho \delta_{j_1 j_2} + \rho u_{j_1} u_{j_2}) &= 0 \\ \frac{\partial (\rho u_{j_1})}{\partial t_1} + \left(1 - \frac{\omega}{2}\right) \frac{\partial}{\partial r_{j_2}} \sum_i c_{i,j_1} c_{i,j_2} f_i^{(1)} &= 0 \end{aligned} \quad (2.64)$$

The sum in the bottom equation can be rewritten by using some algebraic manipulations. The derivation is quite long, so only the result of the derivation is shown below:

$$\sum_i c_{i,j_1} c_{i,j_2} f_i^{(1)} = -\frac{\Delta t}{\omega} \left[ c_s^2 \rho \left( \frac{\partial u_{j_2}}{\partial r_{j_1}} + \frac{\partial u_{j_1}}{\partial r_{j_2}} \right) - \frac{\partial}{\partial r_{j_3}} (\rho u_{j_1} u_{j_2} u_{j_3}) \right] \quad (2.65)$$

Now, by combining 2.64 and 2.65, a form of the momentum equation of the incompressible Navier-Stokes equations is obtained. Again, the sum of the partial time derivatives is taken here:

$$\begin{aligned} \frac{\partial (\rho u_{j_1})}{\partial t} + \frac{\partial (\rho u_{j_1} u_{j_2})}{\partial x_{j_2}} = \\ -\frac{\partial}{\partial x_{j_1}} (c_s^2 \rho) + \frac{\partial}{\partial x_{j_2}} \left[ \left(1 - \frac{\omega}{2}\right) \frac{\Delta t}{\omega} \left( c_s^2 \rho \left( \frac{\partial u_{j_2}}{\partial x_{j_1}} + \frac{\partial u_{j_1}}{\partial x_{j_2}} \right) - \frac{\partial}{\partial x_{j_3}} (\rho u_{j_1} u_{j_2} u_{j_3}) \right) \right] \end{aligned} \quad (2.66)$$

The equation above only represents the incompressible Navier-Stokes equations if the parameters in the equation are chosen carefully. The restrictions to these parameters and relations between the parameters in LBM simulations will be discussed in section 4.2. If these parameters are chosen correctly, the derived discrete BTE can be used to simulate incompressible flows, like blood flows in the human body.

## Chapter 3

# Biomedical background of the liver and radioembolization

The liver is the largest internal organ in the human body, located in the abdomen. The liver weighs about 1500 grams and it is one of the most versatile organs, performing over 500 known functions [33] [34]. It is part of the gastrointestinal tract and it is vital to a working metabolism. Next to storing nutrients, it acts as a filter for blood and chemicals in food, medicine and alcohol. If the liver function becomes limited, a person often experiences problems with body homeostasis and the liver begins to decompensate [35]. One of the possible reasons for liver decompensation is liver cancer. In liver cancer, cells in the liver start to grow unbounded, spreading and invading other parts of the liver or the body [36]. There are many causes for liver cancer, which are often life style related, like excessive drinking, smoking or obesity. Other possibilities concern long term liver diseases, like liver cirrhosis or hepatitis B or C viruses. For advanced stage liver cancer, a non-ablative therapy called radioembolization can be used to treat the tumour and increase the life expectancy and quality of patients.

The goal of the research is to get a better understanding of radioembolization treatment, which could be improved with this information. For the modelling and interpretation of the results of the simulations in this thesis, a good understanding of the liver and radioembolization is required. In this chapter, the required information for a good understanding of the study will be given, which should provide more insights in the acquired results from the simulations.

### 3.1 Human liver anatomy and physiology

The liver plays a vital part in the metabolism of many vertebrates. In order for the liver to perform its functions, it has to work together with the surrounding organs in many and often complex ways. In this section, the anatomy and physiology of the human liver will be explained and discussed. The anatomy of the liver can become very complex and whole books are written on the anatomy and physiology of the liver. The focus here is on the macroscopic anatomy, as the microscopic anatomy is too small for the level of detail for the modelling, or the smallest scale is already represented by the macroscopic anatomy. Also, the blood supply is the most important aspect for a good understanding of the impact of the study, so the general focus in this chapter is on the macroscopic blood supply.

The liver is located in the upper right side of the abdominal cavity, with a large part of the liver being covered by the rib cage. A simplified anterior representation of the abdominal cavity is given by figure 3.1a. A part of the liver is connected to the thoracic diaphragm with areolar tissue, which is a type of connective tissue. The thoracic diaphragm, often referred to as just diaphragm, separates the thoracic cavity, which contains the heart and the lungs, and the abdominal cavity. Since the liver is connected to the diaphragm, it moves down in inspiration and up in expiration. The liver is closely related to the small intestine and other organs in the digestive tract, from which it receives nutrient-enriched venous blood. The liver also secretes bile, which is transported to the duodenum, which is the first part of the small intestine. The liver secretes bile continuously, however the usage of bile is not constant in the digestion. Any excess bile is stored in the gallbladder, which is located just below the liver.

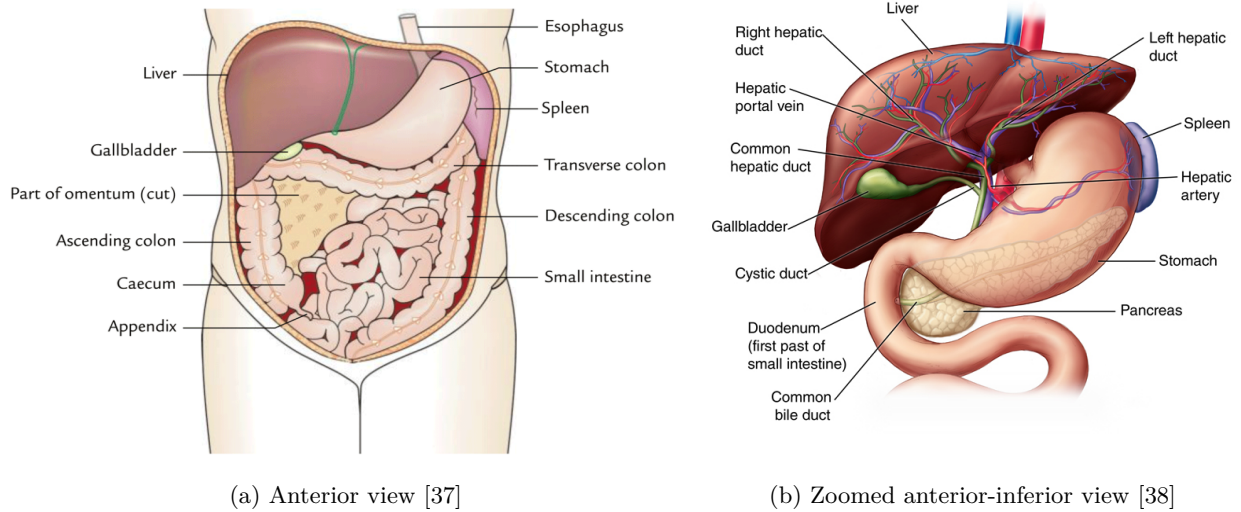


Figure 3.1: Anatomy of the abdominal cavity

Next to bile, the liver produces many more important substances, like cholesterol, glycogen and urea. Cholesterol is used to make hormones and other substances that help in the digestion of food. Glycogen is produced from glucose, which unlike glucose can be stored in the body. Glucose serves as a fuel for cells and a constant supply of glucose can be realised by the conversion of glycogen reserves to glucose. The urea is a product of the blood filtering in the liver, where any old and abnormal red blood cells are removed. Together with other harmful substances they are excreted in the bile and blood in the form of urea. The bile is further processed in the intestine and leaves the body as feces, while the blood is processed in the kidneys and leaves the body as urine.

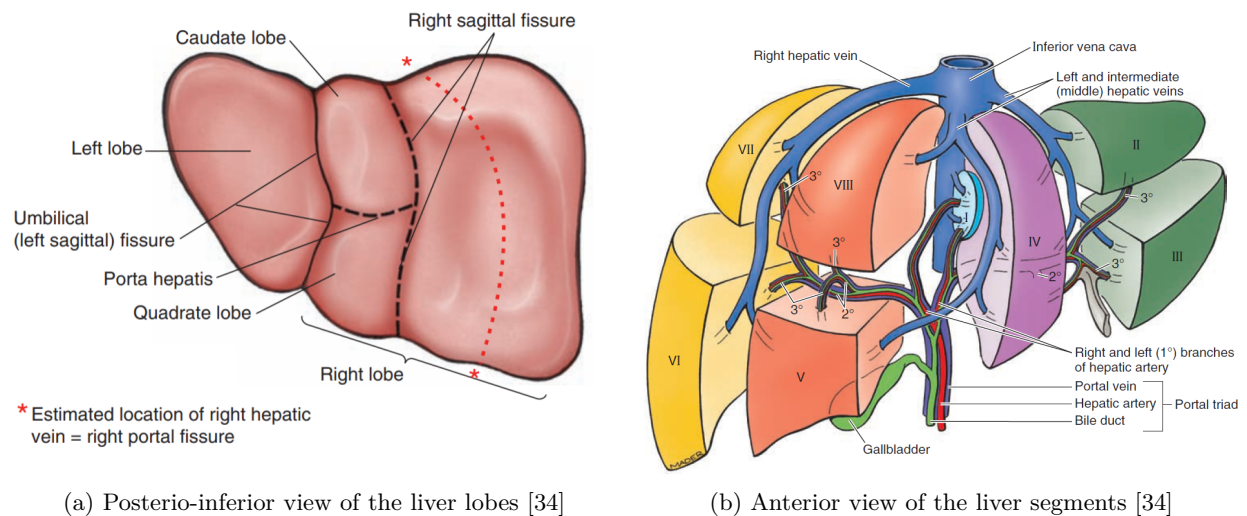


Figure 3.2: Liver anatomy based on division definition

The liver lobes consist mainly of functional tissue, or liver parenchyma. The liver parenchyma consists of about 80% hepatocytes, which can be considered to be the main and most important cells in the liver. The number of non-parenchymal cells, like connective tissue, is relatively large in the liver. However, their volume is small compared to the parenchymal cells.

In the liver, two lobes of unequal size, the left and right lobe, can be distinguished. In figure 3.2a a postero-

inferior view of the liver lobes is given, which means that the liver is observed from the back and below side. The left lobe is much smaller than the right lobe, as can be seen in the figure. When looking at the function of the liver, the two accessory lobes can also be distinguished which gives a liver division with four different lobes. The two accessory lobes are the caudate lobe and the quadrate lobe, which are also given in the figure. The gallbladder is located between the right lobe and the quadrate lobe.

The liver is also sometimes divided into two, four and eight segments based on the blood supply, which can be seen in figure 3.2b. Here an anterior or front view of the liver is given, where the right lobe of the liver is now located on the left side of the figure. The segments that are numbered in the figure can all work independently because they all have their own independent fluid vessels. This also means that all these segments are surgically resectable. The division here can be made by classifying the segments in the liver based on the splitting of the main portal triad branch. For example, the right and left lobe receive blood from the left and right branches of the portal triad, which gives a different definition of the left and right lobe than the anatomical definition.

In the human body, two types of blood circulation can be distinguished: systemic circulation and pulmonary circulation. The liver is part of the systemic circulation, like all other organs in the abdominal cavity. About a quarter of the total cardiac output goes to the liver to deliver oxygen and nutrients that are transported by the blood [33]. In most organs, an artery transports oxygen-rich blood to the organ, where capillaries take care of the distribution. Only one red blood cell can fit through a capillary, so this can be classified as microscopic anatomy. Due to the high pressure in the arteries and the permeable walls of the capillaries, a part of the oxygenated blood is pushed through the walls to the interstitium, where interstitial flow distributes nutrients and oxygen to nearby tissue. After the interaction with the tissue, the capillaries form multiple larger venules, which combine into veins and eventually in the vena cava which transports the deoxygenated blood to the heart.

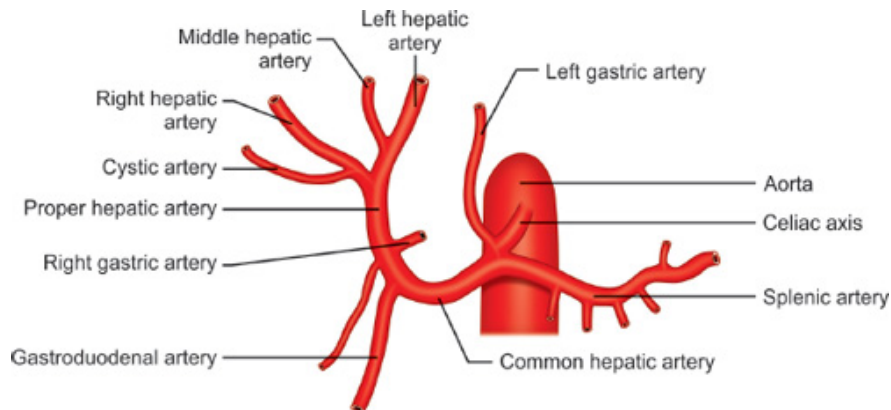


Figure 3.3: Typical pattern of branching of celiac axis and hepatic arteries [39]

The blood supply for the liver is a bit different compared to other organs, because it has a dual blood supply. The liver receives blood from the hepatic artery and also the hepatic portal vein, which contains blood that is already used in the digestive tract, which contains the spleen, stomach, pancreas, and intestines. The largest amount of blood is delivered by the hepatic portal vein. In general, the hepatic portal vein delivers oxygen and nutrients to the liver parenchyma, while the hepatic arteries deliver blood to the non-parenchymal cells in the liver. These two fluid vessels are combined with a third fluid vessel, the bile ducts, which form the portal triad. After they are combined, they branch off over the whole liver, as can be seen in figures 3.1b and 3.2b. The blood vessels transport blood to the liver, while the bile ducts transport bile from the liver. The produced bile in the liver is transported to the gallbladder and the duodenum, which is a part of the small intestine. The gallbladder is connected to the portal triad by the cystic duct.

While delivering a smaller part of the blood supply to the liver of about 25%, a relatively large part of the

required oxygen is delivered by the hepatic arteries. The main artery that eventually branches off into the hepatic artery is called the celiac axis, or celiac trunk. The celiac trunk is a primary branch of the aorta, from which several arteries branch off that go to other organs in the abdominal cavity. In figure 3.3, it can be seen that the name of the artery that goes to the liver is called the common or proper hepatic artery, depending on which and how many arteries have split off from the main artery. From the proper hepatic artery, the left, middle and right hepatic artery deliver the oxygenated blood to the liver. The cystic artery delivers blood to the cystic duct, which is part of the bile ducts that originate from the liver.

In general, the right hepatic artery delivers blood to the right part of the liver, and the left hepatic artery delivers blood to the left part of the liver. In figure 3.2b, this means that the right hepatic artery delivers blood to segments V to VIII. In most cases, it also delivers blood to segment I which is part of the caudate lobe, however this segment also receives blood from the middle hepatic artery. Some of the blood is used by the tissue in the liver and the remaining part is collected by the left, middle and right hepatic vein, which is connected to the inferior vena cava that transports the deoxygenated blood back to the heart.

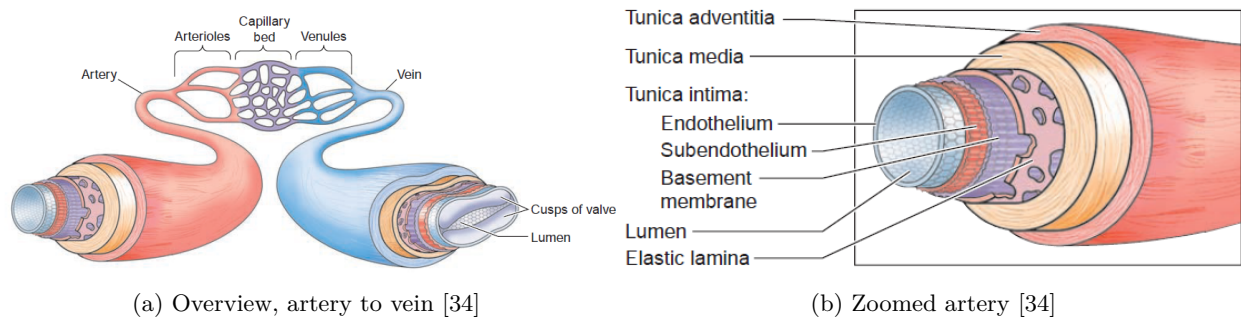


Figure 3.4: Schematic of the blood vessel structure

A schematic of the structure of a blood vessel is given by figures 3.4a and 3.4b. The hollow space in the arteries and veins through which the blood flows is called the lumen. As can be seen in figure 3.4a, the diameter of the lumen is much smaller for the arteries compared to the veins, which helps maintain the blood pressure [40]. Also, the arteries have a thicker wall, which gives them a more rounded appearance than veins. As the blood moves through the arteries to the capillaries, the vessel becomes narrower to maintain sufficient pressure. After the capillaries, the blood flows from the venules to the veins, which eventually enter the vena cava. For the liver, the veins all enter the inferior vena cava, which transports the blood up, back to the heart. For the veins, the diameter of the lumen increases to maintain the pressure and flow in the vessels.

Through the lumen the blood flows, which is composed of plasma, red blood cells, white blood cells, and platelets [41]. About 55% of the whole blood consists of plasma, with the whole blood defined as the blood that runs through the arteries, veins and capillaries. The plasma can be seen as a transport fluid, which transport the blood cells, nutrients and other bodily product in the entire vasculature network. The blood cells consist largely of red blood cells, which contain hemoglobin, a protein that can transport oxygen from the lungs to the organs and carbon dioxide back to the lungs. The white blood cells account for about 1% of the blood and are essential to the immune system. The platelets are small fragments of cells which help in the blood clotting process that closes wounds.

Blood is a non-Newtonian fluid, which has a shear thinning behaviour due to the shape of the red blood cells. At low velocity, the molecular interactions are increased which causes red blood cells to stick together, which is called a Rouleaux formation [42]. As the velocity increases, the shear stress increases which causes a decrease in the blood viscosity. This property of blood is essential to an efficient perfusion of the vascular tree [43].

## 3.2 Liver cancer: statistics, types and treatment

Liver cancer is the fifth most common type of cancer and it is the second leading cause of cancer due to its high mortality rate. If cells start to grow uncontrolled, a tumour is formed which can be either benign (non-cancerous) or malignant (cancerous). A benign tumour does not spread into tissue and it is not able to metastasise, which means that it will not spread throughout the body. In most cases this tumour type is not too harmful and surgery often provides a solution, if required at all. A malignant tumour on the other hand can spread through other tissue and metastasise, which in most cases requires treatment.

The amount of liver cancer diagnoses has more than tripled since the 1980s [44]. In 2020, about 1500 people were diagnosed with liver cancer in the Netherlands [45]. In the same year, about 905.000 cases of liver cancer were reported globally [46]. The mortality of liver cancer in the same year was about 830.000, which gives a global mortality rate of around 92%. A higher mortality rate can be expected in non-western countries, since the possibility of treatment is often more limited here. The amount of new cases in males was about 630.000, which is about 70% of the total amount of cases. The mortality rates for both sexes are about equal. The incidence of liver cancer has remained quite constant over the last few years, so the calculated mortality rate should be accurate and not be affected by yearly fluctuations [44].

The 5 year survival rate for a certain type of cancer gives the percentage of patients who are alive 5 years after their diagnosis. The 5 year survival rate of liver cancer for all ages is about 20% in western countries, compared to 3% four decades ago. The survival rate largely depends on the stage of the cancer when it is discovered, with lower survival rates for metastasised cancer. One of the factors that plays a role in the survival rate is the available treatment at a stage. In general, surgery gives a better survival rate than other therapies like radiation- and chemotherapy, however surgical resection is often not possible for advanced stages of liver cancer.

A distinction is made between two types of cancer: primary and secondary cancer. For a primary type cancer, the cells form at the location itself, while for a secondary type cancer or metastatic cancer, the cancerous cells have formed at another location in the body and have metastasised to the location that is observed. In this case, it concerns malignancies that originate from an extrahepatic site and metastasise to the liver [6]. These tumours are also called metastases. Second type liver cancer is much more common than first type liver cancer in Europe and the US [44].

In the human liver, several types of cancer have been observed and classified based on how and where they form and grow. The most common form of primary liver cancer is Hepatocellular Carcinoma (HCC). HCC is a primary type cancer which has two distinguished growth patterns. The first type of HCC starts to grow in the liver, only spreading to other parts in the liver and the rest of the body at a late stage. The second type of HCC grows as small cancerous nodules (small tumours) on multiple locations in the liver. This type of HCC is often found in patients who also suffer from cirrhosis or scarring of the liver tissue. Another primary type cancer in the liver is called Intrahepatic Cholangiocarcinoma, which is a type of bile duct cancer. The bile ducts are connected to the liver and a part of the bile ducts is located in the liver, so tumours that form in these parts of the bile ducts are classified as liver cancer. However, the largest part of bile duct cancer cases are not classified as primary liver cancer since they form outside of the liver. Next to these two most common types of liver cancer, other types of liver cancer like hepatoblastoma, angiosarcoma and hemangiosarcoma also exist, but they are considered relatively rare.

The liver is especially susceptible to the spread of cancer cells because of its blood filtering function. For this reason, a relatively large part of the liver cancer diagnoses is second type cancer. Second type cancer metastasises from another location in the body and is considered advanced stage cancer if detected in the liver. About 50% of all secondary type liver cancers originate from the colon and rectum, which is a part of the large intestines [47]. This type of liver cancer is called colorectal liver metastases. Up to 70% of people with Colorectal Cancer (CRC) eventually develop liver metastases [48]. The reason for this is partly because of the direct connection between the intestines and the liver through the portal vein. Due to the advanced stage of the secondary type liver cancer, surgery is often not a solution anymore. Other techniques like

chemotherapy, immunotherapy and radiotherapy are often used to extend the lives of patients and enhance the quality of life, however a full recovery is uncommon in advanced stage liver cancer.

Terminal or advanced stage HCC and colorectal liver metastases are often chemorefractory, or not responsive to chemotherapy. Then, a form of radiotherapy called Selective Internal Radiation Therapy (SIRT), or transarterial radioembolization is applied to enhance the survival of patients [49]. In this loco-regional treatment, a radiation source is administered to the blood stream close to the tumour. The radioactive particles are glass or resin microspheres containing either  $^{90}\text{Y}$  (Yttrium-90) or  $^{166}\text{Ho}$  (Holmium-166), which are injected through a catheter [50]. The treatment relies on the principle that hepatic tumours are predominantly supplied by the hepatic arteries, while the healthy liver tissue blood supply is mostly provided by the portal vein. The particles move through the hepatic arteries to the hepatic arterioles, where they cluster and accumulate. The goal is to direct the microspheres to an arteriole near the cancerous tissue, where they lodge and emit beta radiation over time.

The treatment is performed after the angiographic workup, or the mapping of the vasculature. First, an in-vivo simulation procedure is started, where surrogate particles are injected into the bloodstream to predict the microsphere distribution. The results are also used for the assessment of the suitability of the treatment. For example, if microsphere deposition in other vessels than the desired ones is observed, the treatment should be adjusted or maybe even another treatment should be investigated. Based on the in vivo simulation results, a dosis is prescribed and the microspheres are injected into the blood stream. After the procedure, imaging can show the the microsphere distribution, which can validate the earlier performed in vivo simulation and improve the distribution for follow-up treatment.

$^{90}\text{Y}$  microsphere studies in human bodies were already performed in the late 1970s, however it has only proved to be clinically interesting and viable over the last two decades [51]. Around the year 2000, treatment with two types of  $^{90}\text{Y}$  microspheres was approved for unresectable HCC and colorectal metastases. An increasing amount of evidence is emerging that radioembolization is an effective treatment for these two types of diseases [52].

For advanced stage HCC, a median survival of 10 months was the result of a large study with a total of about 700 patients [53]. It is shown that this median survival largely depends on the stage of HCC, however radioembolization data is lacking for earlier stages as it is currently not used as a first-line or primary therapy. For untreated advanced stage HCC, the median survival rate is 6 months, which shows that radioembolization is effective [54]. For colorectal liver metastases, a median survival of 4 to 5 months was reported without radioembolization [55]. A study with 71 patients showed an estimated survival rate of 65% after 6 months and 30% after 12 months, with a median survival of 8 months using radioembolization [56]. In a larger and more recent study with 531 patients, the median survival was even higher at 10.6 months [55]. The treatment shows good results with low toxicity and minor side effects, with the most common side effects being fatigue, abdominal pain and sometimes nausea. These side effects are often caused by extrahepatic deposition of microspheres, where radiation is unintentionally released near healthy tissue outside of the liver.

The study in this thesis focuses on radioembolization using  $^{166}\text{Ho}$  particles. Next to the shorter half-life value of 26.8 hours for  $^{166}\text{Ho}$  compared to 64.1 hours for  $^{90}\text{Y}$ , the paramagnetic properties and gamma radiation of the particles enable imaging with MRI and better imaging with SPECT/CT respectively [57]. The number of studies on  $^{166}\text{Ho}$  radioembolization is relatively small, however a recent study on a small group of 40 patients with colorectal liver metastases shows some promising results with a median survival of 10.7 months [58].

While the treatment is not considered curative by itself, it can offer the possibility of an organ transplant and further surgical resection. Also, it can be applied with other treatments like chemotherapy, which increases the overall effectiveness. With more research on radioembolization, the median survival using this treatment will increase and maybe in the future, radioembolization might be applied in many more cases and be considered a first-line therapy for even early stages of liver cancer.

## Chapter 4

# The APES Simulation Framework

The Lattice Boltzmann Method simulation results that are given in this thesis report are obtained using software from APES. APES is a suite of simulation tools built around an octree mesh infrastructure [59]. APES provides the tools that are required for simulations on large parallel computing facilities, or supercomputers. In figure 4.1 all components that APES provides are given. It is available as an open-source download at <https://apes.osdn.io>.

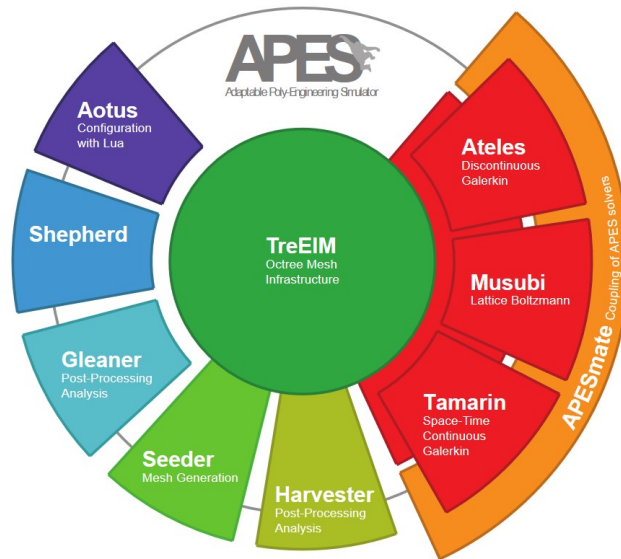


Figure 4.1: APES structure and components

For the LBM simulations, a structured mesh is generated by the mesh generator called Seeder. On this mesh, the LBM simulation software package Musubi is used. For the visualization of the mesh the package Harvester is used. The combination of Seeder and Musubi gives very large simulations that require many computations compared to other conventional CFD software that is based on FEM or FVM. One of the advantages of using the mentioned software is the possibility for parallelization, which allows for solving large scale problems relatively fast by using parallel computers. The computer power comes from the usage of many cores that are provided by the Dutch national supercomputer Cartesius. For the post-processing, the software Matlab and Paraview are used, which will not be discussed as they are quite commonly used packages. In this chapter, the packages and facilities that are used for producing the results are discussed.

## 4.1 Mesh generation: Seeder

The mesh that is used with the Musubi simulations is generated by Seeder, which is a component of APES. Generally, unstructured meshes contain elements of different sizes, which requires that all geometries and relations to neighbouring elements should be described explicitly [60]. For larger systems where parallelization is required, this is not the preferred option. With Seeder, a structured mesh is generated by using the principle of an octree, which does allow for the required level of parallelization [61]. Here, an element is split into eight octants, which results in a mesh refinement in all three spatial dimensions. Translating this process to the entire space, every element in the mesh is split into eight octants, such that with each refinement level, the number of elements is given by  $n_{elements} = 2^{(3 \cdot level)}$ . In this method, a recursive bisection method is used to achieve the desired number of elements in a level, which continually applies bisectioning until the desired element size or number of elements is obtained.

The recursive bisection algorithm is applied to generate the mesh by using the information provided by the bounding cube and the desired element size, thus the level. The bounding cube is a cube that is put around the geometry, which should at least contain the whole geometry. First, elements are put inside the total bounding cube. The recursive bisection algorithm splits the elements based on the geometry, however elements are also put outside of the geometry. Next, the elements that coincide with the geometry are flooded, which means that those elements are saved in the final mesh. This coincidence is determined by placing a seed in the geometry. Everything that is between the walls around this seed is then considered to be the geometry. Elements that coincide with the boundaries of the geometry of the mesh are not flooded. For curved boundaries, this is one of the reasons why a very fine mesh is required to accurately represent the actual model. The level is calculated by using the length  $L$  of the model and the desired element length  $dx$ . The length of the model here is the largest length in one of the spatial dimensions.

$$level = \frac{\log(L/dx)}{\log(2)} \quad (4.1)$$

In the equation, the level is rounded up since it should be an integer. This also means that the desired length  $dx$  will be slightly smaller in most cases. The desired length can still be obtained by changing the size of the bounding cube. The number of elements in the bounding cube is set for a certain level. By increasing the size of the bounding cube, the number of elements and the size of the elements can be changed to better approximate the desired element length  $dx$ . This is done by using the ratio of the desired element length  $dx$  and the 'real' element length  $dx_{real}$  resulting from the rounding of the refinement level. The origin of the bounding cube is placed in such a way that the middle of the geometry is also in the middle of the bounding cube. The origin of the bounding cube is given by equation 4.2.

$$x_{i,new} = x_i - \frac{L}{2} \cdot \left( \frac{dx}{dx_{real}} - 1 \right) \quad (4.2)$$

In the equation,  $L$  is the length of the model and  $x_i$  is the original location of the origin of the bounding cube, with  $i = 1, 2, 3$ , representing the spatial dimensions  $x$ ,  $y$  and  $z$  respectively. The length of the bounding cube is given by equation 4.3, which is the same in each direction.

$$L_{new} = L + L \cdot \left( \frac{dx}{dx_{real}} - 1 \right) \quad (4.3)$$

From the equation, it can be seen that the bounding cube is not expanded if the value of  $dx$  is not changed, meaning that the level is not rounded up. From equation 4.1, it can be concluded that halving the value of  $dx$  results in an increase of the level by exactly 1. The length of the bounding cube is increased more if the rounding of the level is more extreme.

The Seeder program uses an input file where the dimensions are given. In this file, the boundaries of the model, the bounding cube and the refinement level can be defined. The boundaries can be defined by inserting a basic geometry like a plane based on coordinates. For more complex boundaries like the walls of the model that is used for the simulation, a geometry file can be used, like an STL file. These basic inputs for Seeder are sufficient to define the system boundaries for the simulations. In this thesis, other options that are included in the mesh generator are not used.

## 4.2 Musubi: the Lattice Boltzmann solver

The software package Musubi is used for the LBM simulations in this thesis. The software package roughly follows the LB theory given in chapter 2. For the simulations, a Solver Input File (SIF) is used in which the simulation parameters are defined, as well as the tracking of variables used for post-processing. Some of the relevant options will be discussed here to show some of the parameters that can be adjusted for the simulation. The impact of these choices will also be discussed.

In Lattice Boltzmann simulations, the macroscopic physical variables and the microscopic lattice variables are concurrently used in many different contexts. A clear distinction should be made between these two sets of variables, as they can become confusing. In the general sense, the physical variables are defined in such a way that they represent the real physical system, while the lattice variables can often be tuned to ensure a certain accuracy or stability of the simulation [62] [63]. While the lattice variables can be tuned to increase the efficiency or the performance of the simulations, the variables are still bounded by the physical system. Derivations of the lattice variables are usually done by first converting the system to a non-dimensional system and from this system a mesoscopic LB system can be obtained. For all these systems, the dominant non-dimensional numbers in the problem should be equal if a similar problem and solution are desired. In this case, the derivations for the similar Reynolds numbers will be discussed, because this is the only important non-dimensional number for the type of problems in this research. In this section, the definitions of the lattice variables will be given, together with their limitations.

In the previous section, it was already mentioned that the relaxation frequency  $\omega$  is coupled to the viscosity of the system. For a given system, the density and viscosity of the system are known. The density, the kinematic viscosity and the dynamic viscosity are linked by equation 4.4, which means that only two of these parameters should be given to define the system.

$$\nu = \frac{\mu}{\rho} \tag{4.4}$$

The relation between the kinematic viscosity and the relaxation frequency is given by equation 4.5 [26]. This expression is a result of the Chapman-Enskog expansion, which links the Lattice Boltzmann Method to the incompressible Navier-Stokes equations [27]. If the parameters are chosen in this way, then a LB model is obtained that follows the physics that are described by the incompressible NS equations.

$$\nu = \frac{2\tau - 1}{6} \frac{(\Delta x)^2}{\Delta t} = \frac{\frac{1}{\omega} - \frac{1}{2}}{3} \frac{(\Delta x)^2}{\Delta t} \tag{4.5}$$

In the equation, the kinematic viscosity is known from the fluid and the element size  $dx$  depends on the mesh that is used. The parameter  $\omega$  can be tuned, which means that the time step of the simulation is chosen implicitly. If a larger value of  $\omega$  is chosen, then the time step becomes smaller and thus the simulation time is increased. From this equation, we can also see that for a mesh refinement where the element size is halved, the time step is divided by 4, which means that the amount of iterations is multiplied by 4. This is a choice that can be made for the simulations, which is called diffusive scaling. Another option that is sometimes used in LBM simulations is acoustic scaling, which gives a constant ratio of the spatial step over the time

step, instead of the spatial step squared over the time step. In this thesis, diffusive scaling will be used for all simulations. For a 3D model with diffusive scaling, the number of elements is increased by a factor 8 for such a mesh refinement, which means that the total amount of computations is increased by a factor 32. The lattice viscosity is the apparent viscosity in the system on a microscopic level, which is given by equation 4.6.

$$\nu_L = \nu \frac{\Delta t}{(\Delta x)^2} = \frac{1}{\omega} - \frac{1}{2} \quad (4.6)$$

From equation 4.6, we can see that  $\omega$  should be greater than 0, but smaller than 2.0. The lattice viscosity as a function of the relaxation frequency is given by figure 4.2a. In most simulations the value of  $\omega$  is higher than 1.5, which is shown in figure 4.2b. Here, it can be seen that the function is quasi-linear in this region.

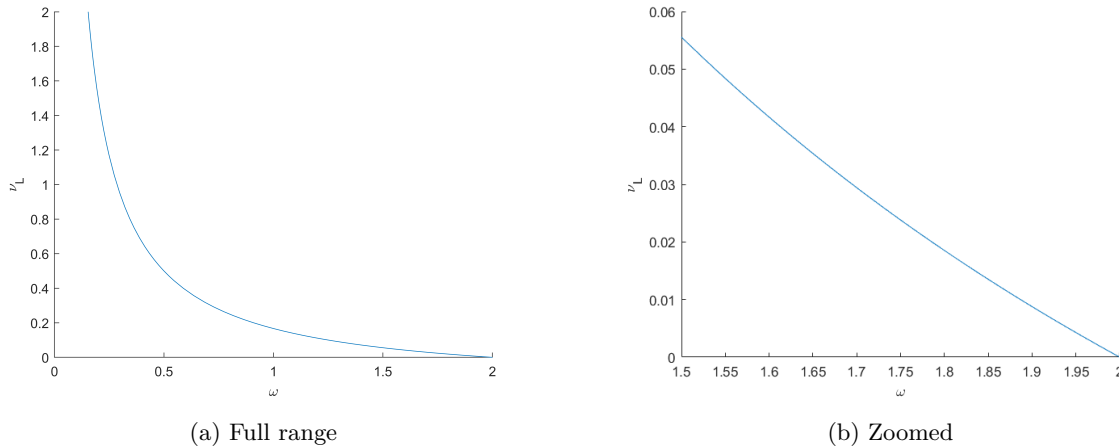


Figure 4.2: Lattice viscosity for different values of  $\omega$ , from equation 4.6

In the figure, it can be seen that lower values of  $\omega$  introduce more viscosity in the system. The viscosity can be seen as damping of the solution: for a higher viscosity, the initial fluctuations in the system are lower, however convergence to a steady solution takes longer. These initial fluctuations can cause some trouble due to limitations to the lattice velocity, however it is often desired to have a low apparent viscosity in the system due to faster convergence. This is one of the reasons why a larger value of  $\omega$  is chosen.

Next to the viscosity, the lattice velocity is an important parameter in LB simulations. The lattice velocity is given by equation 4.7.

$$u_L = u \frac{dt}{dx} \quad (4.7)$$

The lattice velocity now depends on the grid and the time step, while the macroscopic velocity is often determined by the problem. A mesh refinement can solve the problem, since a decrease in  $dx$  gives an even larger decrease in  $dt$  due to the definition of the viscosity given by equation 4.5. From this same equation, it can also be seen that an increase in the relaxation frequency leads to a smaller time step. While the relaxation frequency leads to a smaller time step, it also leads to larger initial fluctuations, which could mean that the lattice velocity is actually larger at the start for a larger value of  $\omega$ .

At the start of this section, it was mentioned that only the Reynolds numbers of the systems should be matched to ensure a physical solution. This is partly true, as the Mach numbers of the systems should also be below the threshold for the assumption of incompressible flow, but they do not have to be matched exactly. The Mach numbers for the types of problems in this research are well below the compressibility

threshold on the macroscopic scale. On the mesoscopic scale this is often not the case, but also not desirable since this requires very fine meshes and many iterations because of the low time step. The threshold is set at  $u_L = 0.15$  and the simulation stops if the lattice velocity in the model is higher than this velocity at any point. Officially, an incompressible flow can be assumed if the fluid speed is lower than 0.3 times the speed of sound. The lattice elements that are used in this research have  $c_s^2 = 1/3$ , which means that the lattice speed should be lower than  $u_L = 0.10$  for the official definition of incompressible flow.

In Musubi, a choice should be made for the physical model, which can be either a compressible or incompressible fluid, where the choice mainly depends on the value of the Mach number in the problem. The model of the simulations in this thesis is set to an incompressible fluid, since the Mach number is below the compressibility limit. It is expected that this choice will not have a large influence on the simulation, since the choice for a compressible model would only result in small density fluctuations due to the definition of incompressible flow. With the incompressible model, a standard value is chosen for the bulk viscosity and only the kinematic viscosity and the density of the fluid should be given. The bulk viscosity is a hydrodynamic parameter that is important in compressible flows, which captures more movement of molecules like vibrations and rotations, instead of only the translations that are described by the dynamic viscosity [64].

For the relaxation frequency in LBM, either BGK or MRT relaxation is used. BGK relaxation is named after the BGK approximation, which gives a single relaxation frequency that is used in the entire simulation. It has an easy implementation, however it can give some numerical instabilities and unphysical numerical artifacts in complex geometries [65]. The other relaxation option is MRT, which uses multiple relaxation times that are tuned by Musubi to ensure numerical stability. In general, MRT relaxation will give a more stable simulation, however some varying values of the relaxation frequency will be used. In most cases this is fine, however using multiple relaxation frequencies might influence a grid refinement study, as the value of  $\omega$  should be kept constant to get the expected convergence slope.

In the simulations, the standard condition that is used at the walls is a bounce-back condition. This condition is first order accurate, which offers advantages for computation time. In the chapter on the LBM theory, higher order bounce-back boundary conditions were discussed briefly, which are also available in Musubi, with the implementation method explained by Bouzidi et al. [66]. In this thesis, only the first order bounce-back condition will be used in the simulations. This means that the results become first order accurate due to the boundary condition. The derived equations for the bulk flow are second order accurate, which means that second order behaviour can be obtained in Musubi by changing the wall boundary condition. The most important options in the SIF have been discussed that are relevant for this thesis. Information about the other options should not be required to understand the simulation results and the impact of the choices made in the simulations thereon.

### 4.3 Code execution: High Performance Computing

The Musubi code was executed on two clusters. The first cluster is a local cluster from the Thermal and Fluid Engineering department of the University of Twente. This cluster can be used for some small LBM simulations, however it is not always reliable due to variations in users of the cluster. Also, for larger LBM simulation the cluster does not provide enough cores to ensure fast simulations. The total amount of cores on the TFE cluster is 480, which are divided over 15 nodes with 32 cores each. The other core cluster that is used is provided by the Dutch national super computer Cartesius, which is a part of the cooperation association of educational and research institutions called SURF [67]. Cartesius uses a Slurm Workload Manager, which is a job scheduler for Linux kernels that increases the reliability of running simulations consistently. The maximum number of cores that a user can use at once on Cartesius depends on the type of node. The maximum number of nodes for the standard node type is 17,280, which is a maximum of 720 nodes with 24 cores each. While many cores can be used, the clock speed of these cores is relatively low. The clock speed gives information about how fast arithmetic operations are done by a CPU. The potential of a supercomputer relies mostly on the number of cores and the individual performance of each core is less important.

# Chapter 5

## Preliminary pipe flow studies

To get familiar with the software and to see the effects of different parameters, two test cases were used to get a better understanding of the possibilities for Lattice Boltzmann simulations. For this purpose, the steady behaviour of two types of channel flow with a different uniform cross-sectional geometry are analysed. For the second test case with a square cross-section, the transient behaviour is also analysed.

### 5.1 Pipe flow with a circular cross section

The first case that is analysed is a pipe flow test case. This is also one of the benchmark cases from Musubi, to check if the implementation of the code is done correctly. The flow characteristics of pipe flow have been studied many times and the type of flow for the test case has a specific name: Poiseuille flow [68]. Poiseuille flow is an axisymmetrical pressure induced laminar flow in a long horizontal tube, meaning  $R \ll L$ , with  $R$  the radius and  $L$  the length of the pipe.

The flow becomes fully developed after a certain length, called the inlet length. The equations below are derived from the assumption of fully developed flow. This means that the pressure drop is only caused by friction and not by acceleration to fully developed flow [69]. Poiseuille flow can be assumed if equation 5.1 is valid.

$$\frac{\Delta L}{2R} > \frac{Re}{48} \quad (5.1)$$

The definition of the Reynolds number is given by equation 5.2.

$$Re = \frac{\rho u L}{\mu} = \frac{u L}{\nu} \quad (5.2)$$

Poiseuille flow is only valid for laminar flow, restricting the possible values for the Reynolds number. The maximum Reynolds number in equation 5.1 cannot be higher than 2300, which is the critical Reynolds number for pipe flow. Substitution of the values of the geometry for this test case in equation 5.1 gives a maximum Reynolds number of  $Re = 363$ , which means that similar results should be obtained based on the type of flow.

The mass and momentum conservation equations of the Navier-Stokes equations are solved to obtain an analytical expression for the axial velocity. Here, a no-slip boundary condition is used at the edge and a symmetry condition is used at the centre of the pipe. The derivation of this equation can be found in many textbooks and the results have already been used in many benchmark test cases, so the details of this derivation will not be discussed here. The equation for the velocity is given by equation 5.3 in cylindrical coordinates  $x$ ,  $r$  and  $\theta$ .

$$u_x = \frac{\Delta p (R^2 - r^2)}{4\mu L} \quad (5.3)$$

In the equation,  $\Delta p$  is the pressure difference over the pipe,  $R$  is the radius,  $\mu$  is the dynamic viscosity and  $L$  is the total length of the pipe. From this equation it can be seen that the velocity profile is parabolic. The expression for the pressure drop is obtained by using that the velocity is highest at the centre of the pipe.

$$\Delta p = \frac{4\nu\rho L u_{max}}{R^2} \quad (5.4)$$

Here, the dynamic viscosity is written as the product of the density and the kinematic viscosity, because these two variables are used to define the flow properties for the simulation. The velocity profile is parabolic, which means that the velocity is highest at the centre of the pipe. Also, the maximum velocity for Poiseuille flow through a circular pipe is exactly twice the mean velocity:

$$u_{max} = 2 \cdot u_{mean} \quad (5.5)$$

The analytical solution is now fully described. Now, the first test case can be described. The parameters for the simulation can be found in table 5.1.

Parameter	Value	Parameter	Value
R	0.205 [m]	$\rho$	1.0 [kg/m <sup>3</sup> ]
L	2.05 [m]	$u_{max}$	0.244 [m/s]
$p_{amb}$	1.0 [Pa]	$\nu$	$1.0 \cdot 10^{-3}$ [m <sup>2</sup> /s]
$\Delta p$	$4.76 \cdot 10^{-2}$ [m <sup>2</sup> /s]	Re	100

Table 5.1: Parameters for Lattice Boltzmann pipe flow simulations

For this case the fluid properties are not linked to a specific fluid. The parameters are chosen such that the resulting velocities and pressures are not too small or too large and such that the specific effects can be observed clearly. The ambient pressure  $P_{amb}$  is chosen to be equal to 1, which is defined in such a way that the pressure at the end of the channel is equal to the ambient pressure. Also, this case is a benchmark case from Musubi and the parameters were not changed.

Poiseuille flow is a pressure driven flow, so the boundary conditions for both the inlet and the outlet are pressure related. The pressure here is defined by using the pressure drop from equation 5.4. The pressure of the outlet is set to the ambient pressure  $P_{amb}$  and the pressure of the inlet is set to the sum of the ambient pressure and the pressure drop, where the pressure drop is positive. For the inlet and outlet, pressure extrapolation boundary conditions are used with different values. This also means that after convergence, the inlet flow is already parabolic and no acceleration to Poiseuille flow takes place. A constant pressure does not limit the velocity in the radial direction, so here the velocity will directly assume the parabolic velocity profile. For the walls, a standard bounce-back condition is used.

For this simulation, the relaxation frequency is implicitly defined by defining the lattice Mach number. As will be shown later in this section, this results in a slightly changing value of  $\omega$ . For the relaxation method, the standard BGK relaxation is used.

The results for the velocity and the pressure at the centre of the pipe in the middle can be seen in figures 5.1a and 5.1b. Here, the analytical solution is the fully developed solution at the centre of the pipe, which is the expected result from the simulations at every  $x$  location in the pipe, with  $x$  in lengthwise direction.

For these results, a probe was placed at the centre of the middle of the pipe, however the same results are expected at another location with  $r = 0$ .

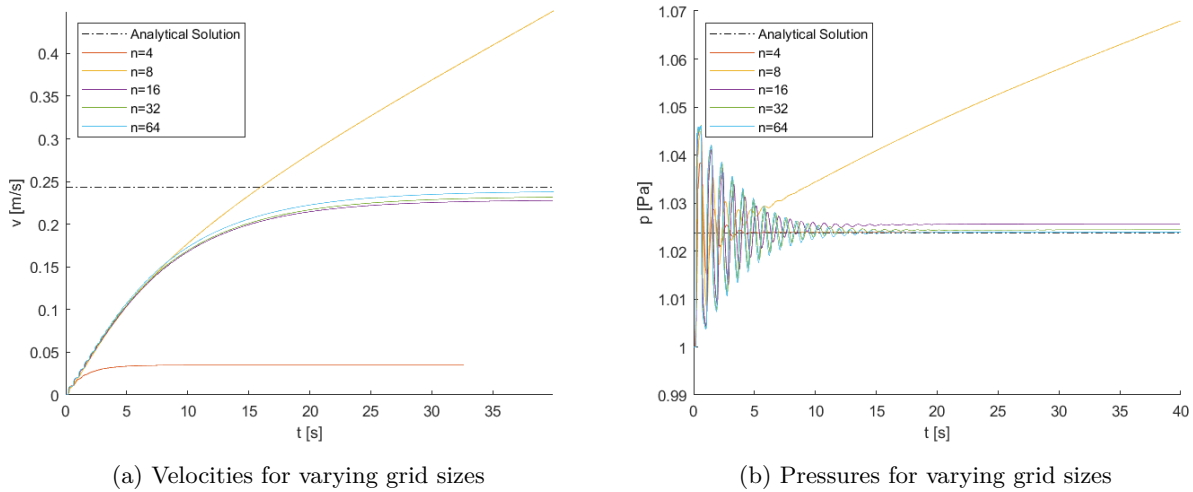


Figure 5.1: Velocity and pressure at the centre of the middle of the pipe

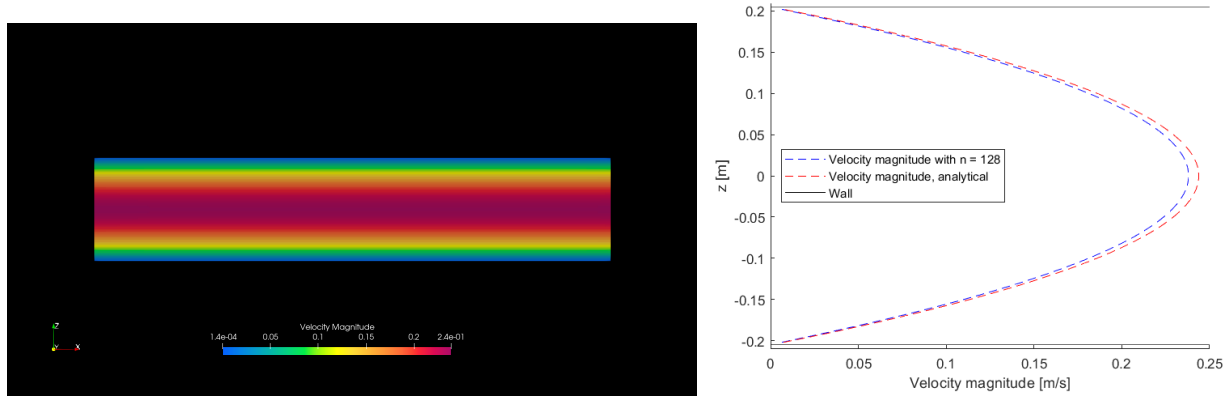
In figure 5.1a, the reference analytical solution line is given by  $u_{max}$ , since the centre of the pipe is observed. In the figures,  $n$  is the number of elements in radial direction. In table 5.2, the different parameters for different grid sizes can be found.

n	N	dt	iterations	$\omega$
4	252	1.213e-2 s	2691	1.986
8	2132	6.066e-3 s	6595	1.973
16	16848	3.033e-3 s	13189	1.946
32	130732	1.516e-3 s	26378	1.895
64	1025916	7.582e-4 s	52755	1.800
128	8197108	3.791e-4 s	131892	1.637

Table 5.2: Pipe case simulation parameters

For  $n = 4$ , a converged solution is obtained, which is truncated because of an implemented abort criterion in the benchmark case, which states that the simulation is aborted if the velocity and pressure fluctuations are both smaller than  $1 \cdot 10^{-8}$ . In figure 5.1b, the reference line is exactly half the pressure drop. The coarsest grid simulation does give a very good result for the pressure, however for the velocity plot shows that the result is bad. For  $n = 8$  an unstable solution is obtained which can be seen in both the pressure and velocity graphs. For the three finer grids, steady and converging solutions are obtained, which approach the reference lines better for the finer grids.

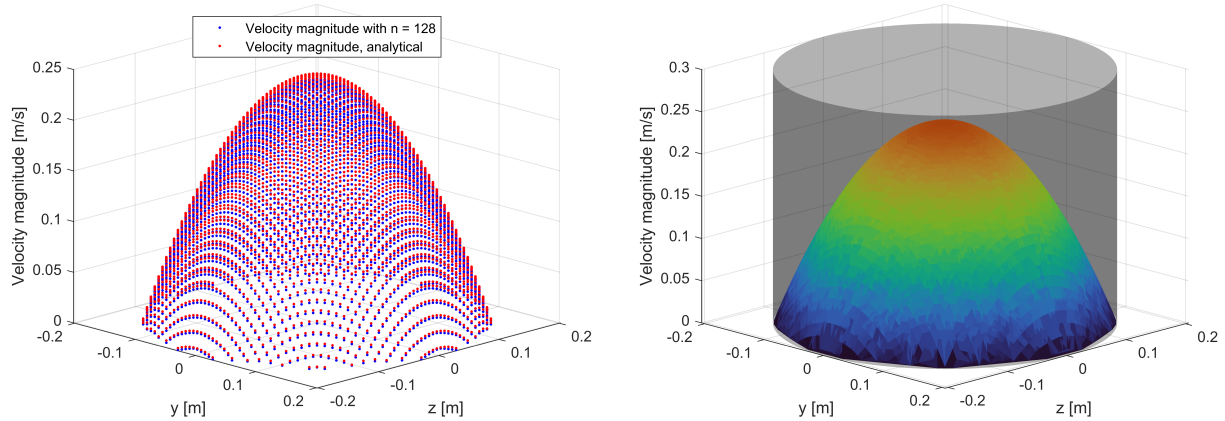
For one finer grid than is displayed in figures 5.1a and 5.1b with  $n = 128$ , the velocity field of a cross-section in length-wise direction is visualised in figure 5.2a. Also, the results for the velocity along the height of the pipe for the same grid is given by figure 5.2b.



(a) Velocity field in the cross-section, using Paraview (b) Velocity along the height at the centre of the pipe

Figure 5.2: Velocity fields in two cross-sections, with  $n = 128$

In figure 5.2a it can be seen that the flow does not accelerate to Poiseuille flow and that the velocity profile is independent of  $x$ . From figure 5.2b it can also be seen that the analytical solution is quite well approached if we look at the centre line in the pipe. The line velocity is expanded to a 3D planar velocity plot in figures 5.3a and 5.3b.



(a) Numerical and analytical solution

(b) Numerical solution with the pipe geometry as reference

Figure 5.3: Fully developed planar velocity plots of the pipe

The convergence for the different grid sizes can be analysed by using the Euclidean norm, or  $L_2$  norm, for difference between the analytical solution  $X$  and the numerical solution  $x_h$  over the whole grid. This norm is given by equation 5.6, which gives the mean error per element:

$$L_2(x) = \frac{1}{N} \sqrt{\sum (x_h - X)^2} \quad (5.6)$$

In the equation,  $N$  is the total amount of elements in the model. The convergence results for the different grid refinements in table 5.2 can be seen in figure 5.4.

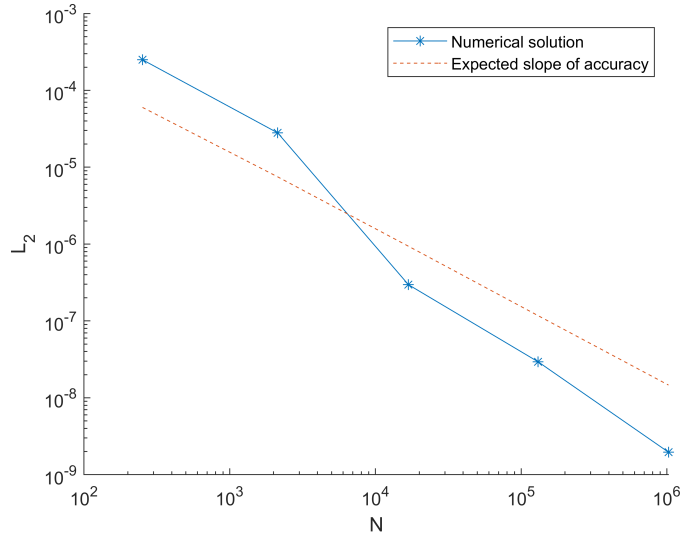


Figure 5.4:  $L_2$  norm for different grid refinements

From the characteristics of the Lattice Boltzmann method, we know that the method is first order accurate if the collision frequency  $\omega$  is kept constant. The definition of the variables for this test case is a bit different from the usual method, where the lattice Mach number is kept constant instead of the relaxation frequency. This results in a value for the collision frequency that is slightly changing per grid refinement, as can be seen in the last column of table 5.2. For this reason, the slopes in figure 5.4 do not match entirely and the error reduction is not exactly first order.

## 5.2 Pipe flow with a rectangular cross section: steady flow

For further analysis, a pipe with a rectangular cross section will be used, which will be referred to as channel. The geometry of this channel can be found in table 5.3, along with the properties of the fluid that flows through the channel. The fluid properties of Blood Mimicking Fluid (BMF) are used for these simulations. BMF is a mixture of water, glycerol and urea, which is the working fluid that is used in the experimental setup that is used for comparison with the main research in this thesis. This fluid is also used here to investigate its behaviour in a steady-state case with a simple geometry concerning. The geometry is given in  $mm$  and all units that contain a unit of length have been converted accordingly.

Parameter	Value
L	150 [mm]
B	20 [mm]
H	20 [mm]
$U$	$1.0 \cdot 10^{-6}$ [mm/s]
$\rho$	$1.1474 \cdot 10^{-6}$ [kg/mm <sup>3</sup> ]
$\mu$	$4.3100 \cdot 10^{-6}$ [kg/(mm · s)]
$\omega$	1.9 [-]

Table 5.3: Parameters for Lattice Boltzmann mini channel flow simulations

The boundary conditions for this test case are a little bit different compared to the pipe flow test case: the

left boundary has a prescribed velocity, which is imposed as a block velocity. This means that the fluid first has to develop to the parabolic Poiseuille flow velocity profile.

First, the steady state simulation will be tested using different refinement levels. For these different refinement levels, the relaxation frequency remains constant, while the lattice size  $dx$  and resulting time step  $dt$  decrease per level. For these simulations, an incompressible fluid model and the standard BGK relaxation method are used.

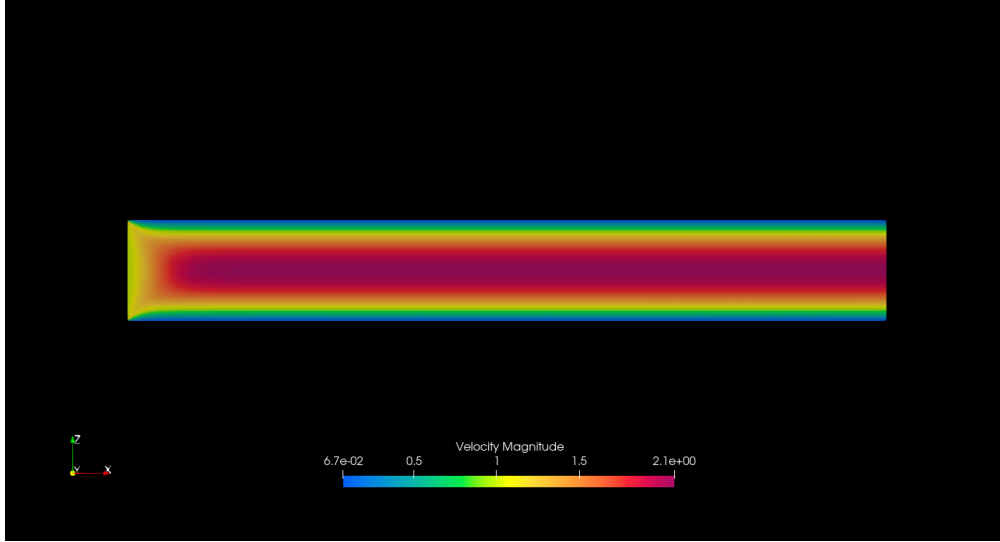


Figure 5.5: 2D view of the converged solution for the velocity in the channel

In the generation of the different meshes, a refinement level was prescribed and the bounding box remained constant. The result is that the element size on the new level is exactly half of the old element size. This also means that the difference between the new time step and the old time step is a factor 4 because of the constant  $\omega$ , which is explained in section 4.2. For Poiseuille flow in a channel with a rectangular cross-section, the velocity in the stream-wise direction is given by equation 5.7 [70]:

$$u = U \frac{48 \sum_{i=1,3,5,\dots}^{\infty} (-1)^{(i-1)/2} \left[ 1 - \frac{\cosh(i\pi y/2a)}{\cosh(i\pi b/2a)} \right] \frac{\cos(i\pi z/2a)}{i^3}}{\pi^3 \left( 1 - \frac{192a}{\pi^5 b} \sum_{i=1,3,5,\dots}^{\infty} \frac{\tanh(i\pi b/2a)}{i^5} \right)} \quad (5.7)$$

In the equation,  $U$  is the bulk or mean velocity,  $a$  is half of the width of the channel and  $b$  is half of the height of the channel. Since the cross section of the channel is square, we have  $a = b = 10mm$ . While equation 5.7 is an analytical expression, the equation is solved numerically to solve the sum in the equation. For this, we will first look at the convergence of the numerical solution to the analytical expression by using the following  $L_2$  norm:

$$L_2 = \frac{1}{N} \sum_{i=1}^{i=N} \sqrt{(u_{i,j} - u_{i,j-1})^2} \quad (5.8)$$

In the equation,  $N$  is the number of grid points and the index  $j$  represents the number of summation components. The  $L_2$  norm here calculated the convergence, where the result for the new sum is compared to the result of the old sum with one less component. For  $j = 1$ , the sum is solved for  $i = 1$  in equation 5.7, which can not be compared to the previous solution and it is thus not calculated. The result can be seen

in figure 5.6. Note that the  $x$ -axis represents the number of sum components and since the sum interval in equation 5.7, the sum index is about twice this value.

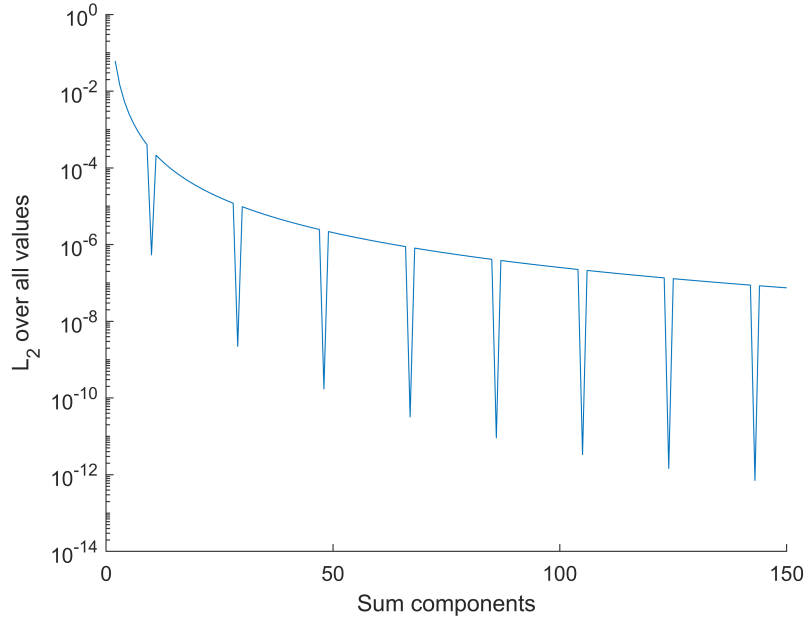


Figure 5.6:  $L_2$  norm of the convergence of the analytical solution, solved numerically

In the figure, a relatively smooth convergence can be seen. The spikes in the figure are a result of the hyperbolic trigonometric functions. For some sum components, these functions result in a very low value that is added in the sum, which means that the difference between the updated value and the old value in the sum is very small, hence a spike in the convergence plot. For the 150th sum component, the difference is of the order  $10^{-7}$  and we assume that the error in the approximation is of the same order. The velocity differences between the approximated analytical expression and the simulation on the finest grid is in this case of the order  $10^{-4}$ , so we can assume that the analytical expression is approximated well enough to capture the convergence of the simulations. So, we will consider the analytical expression with the sum to 299 for the comparison to the simulation results. The result of the approximation analytical solution can be seen in figure 5.7.

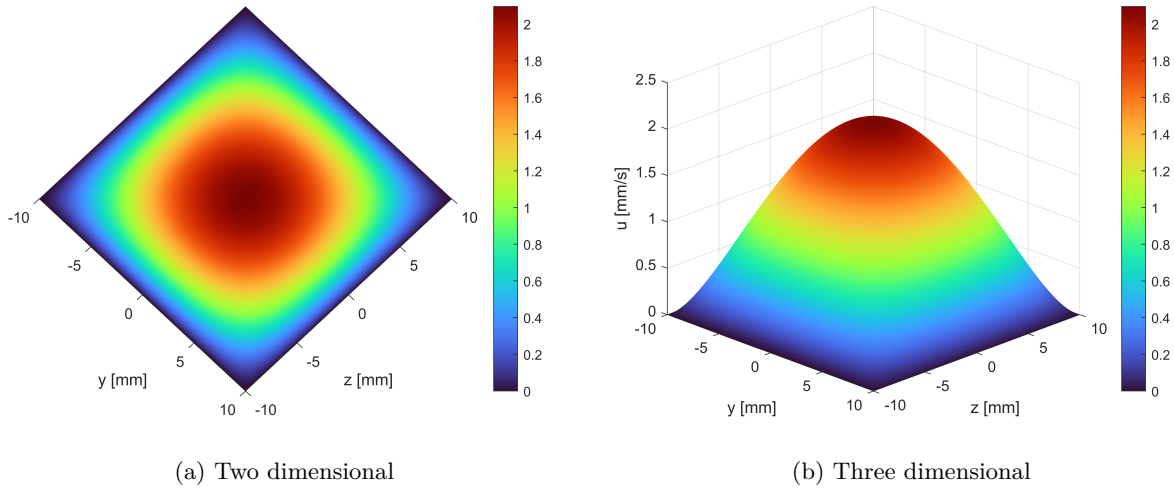


Figure 5.7: Velocity solution of the approximated analytical expression

To compare the simulation results to the analytical results, we take the velocities at a cross section near the end of the channel. As mentioned before, the boundary condition imposes a block velocity at the start, which means that the flow should first accelerate to Poiseuille flow. In figure 5.5 it can be seen that this happens quite early in the channel, however for the best result we will still take a plane near the end. The simulations were performed on 4 different grids, which can be found in table 5.4.

Level	N	$dx$ [mm]	$dt$ [s]	iterations
5	480	4.69	$5.13 \cdot 10^{-2}$	974
6	3968	2.34	$1.28 \cdot 10^{-2}$	3897
7	32256	1.17	$3.20 \cdot 10^{-3}$	15591
8	293624	$5.86 \cdot 10^{-1}$	$8.02 \cdot 10^{-4}$	62364
9	2358240	$2.93 \cdot 10^{-1}$	$2.00 \cdot 10^{-4}$	249456

Table 5.4: Simulation parameters with grid refinements

Now a mesh convergence study can be done by using the Euclidean norm given by equation 5.6. The results can be found in figure 5.8, along with the expected first order slope. Here, the level 5 grid is not included in the figure because of the relatively bad solution.

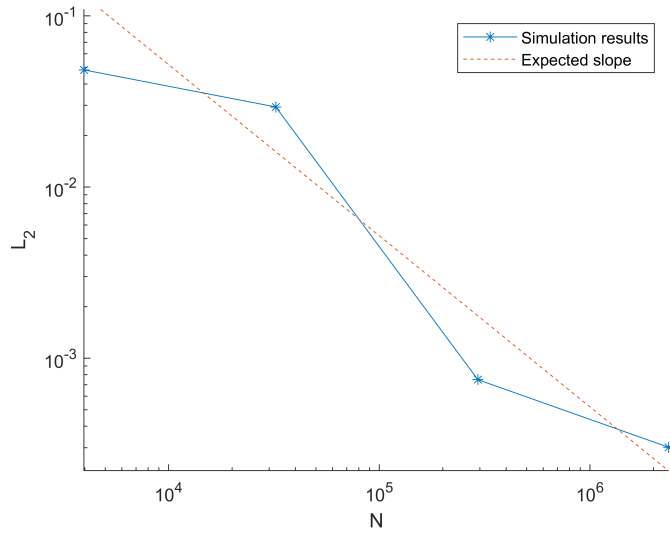


Figure 5.8: Mesh convergence of the channel, using the Euclidean norm

The same value  $\omega = 1.9$  is now used for all simulations, first order behaviour should now be obtained for the error norm. In the figure it can be seen that, although the result is not a straight line, this behaviour is approximately obtained. In the ideal case the result is a straight line, similar to what was observed in the previous test case in figure 5.4, however for this case with flow development and a square cross section that is relatively more complex, this result can be considered quite acceptable.

Next to the convergence study, we will look at some other parameters and their influence on the simulations. For the results below, the average over the cross section was taken near the inlet and the outlet. Note that the time interval is changed from  $t = 50s$  to  $t = 30s$  for visualization purposes.

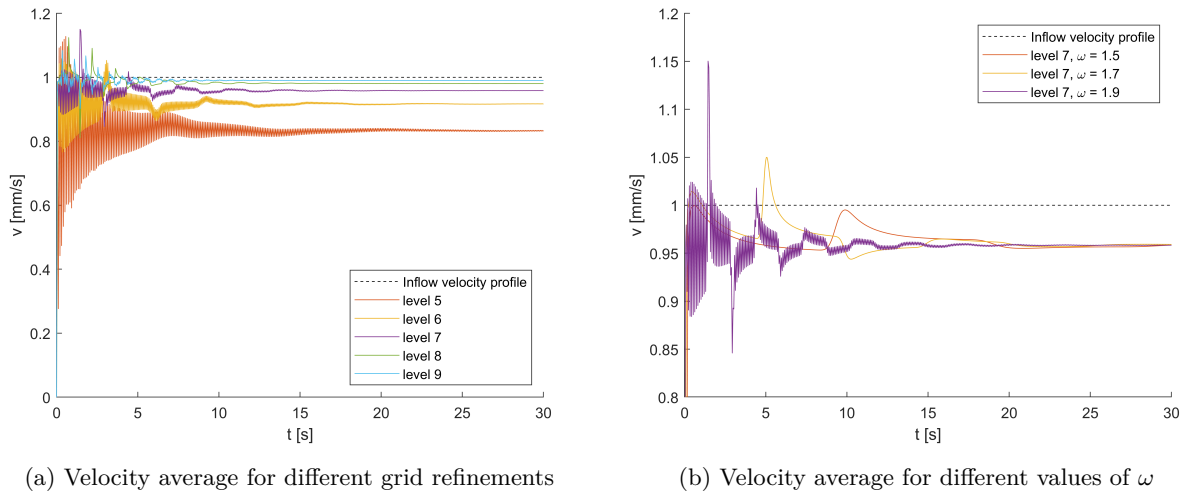


Figure 5.9: Channel velocity average over the cross section near the inlet

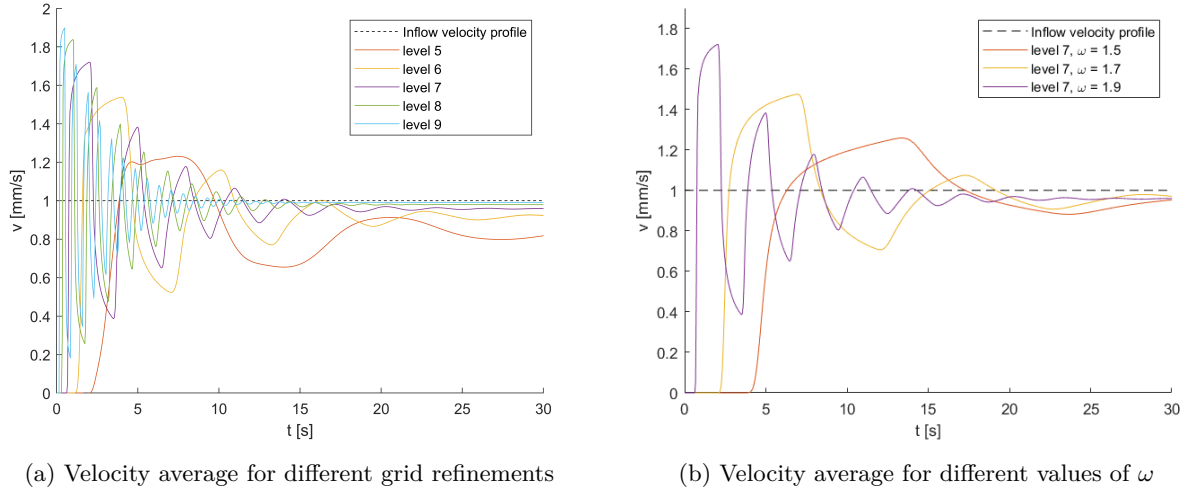


Figure 5.10: Channel velocity average over the cross section near the outlet

In the figures above, we can see the convergence for different grid sizes and values of  $\omega$ . For the different grid sizes, the same value of  $\omega = 1.9$  is used, while for the different values of  $\omega$  the same grid level is used: level 7. Also, the expected velocity is plotted. For the steady-state simulation using the incompressible fluid model, the average velocity should be the same everywhere in the channel, independent of the location and flow development stage. Thus, if the inlet velocity value is better approximated, we have a better solution. For the grid refinements, we can see that the solution converges faster and to a better value for a finer grid. The faster convergence is most likely due to the increased amount of iterations on a finer grid, while the better approximation is also expected based on the convergence study.

The density plot for different grids also gives interesting information about the results. For the simulations, an incompressible model is used, however the density cannot be constrained in LB methods. The density at the centre of the middle of the channel is given by figure 5.11.

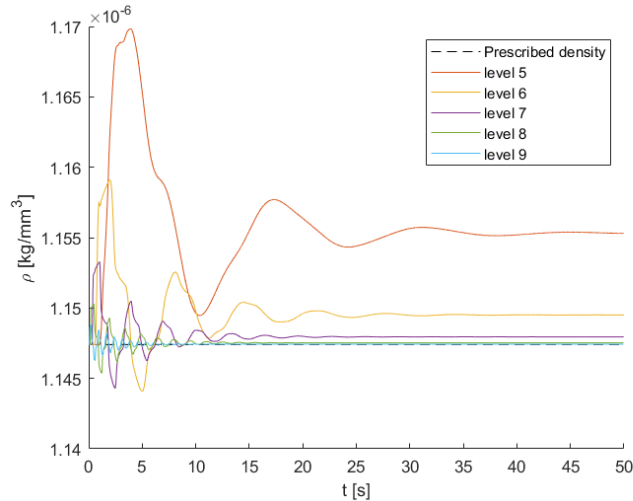


Figure 5.11: Channel density at centre for different grid refinements

In the figure, it is clear that the fluid is not entirely incompressible. However, a finer grid does give a better approximation of the density that is prescribed for the simulation. The steady state simulation in the channel

gives the expected results, so now the simulation can be expanded to a transient simulation by varying the input signal in time. The transient behaviour will be analysed by using a simple sine wave input. From the results in figures 5.9a and 5.10a, it is assumed that the simulations are converged well enough after 20 seconds, especially on the finer grids. This will be the starting point of the sine wave, with the proposed input signal given by figure 5.12.

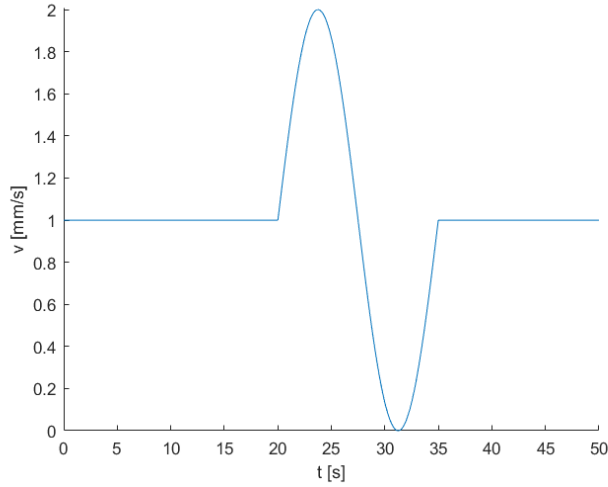


Figure 5.12: Transient inlet velocity profile

The sine wave is smooth, however the start of the wave is quite abrupt and the input signal has a discontinuous acceleration. By this, the response of a change in the system for a grid can also be analysed. The results for the velocities at the inlet and the outlet can be found in figures 5.13a and 5.13b.

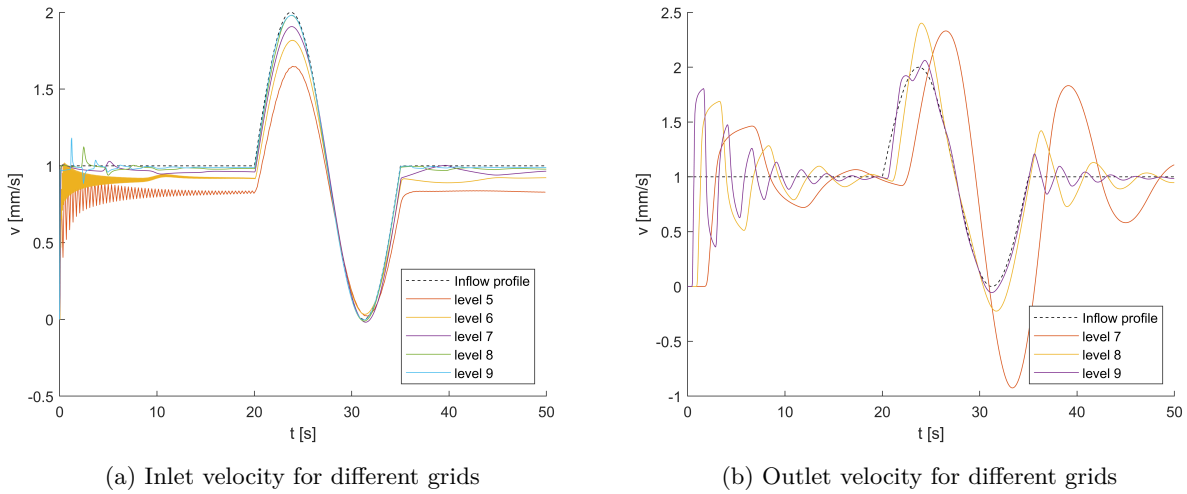


Figure 5.13: Channel velocity average over the cross section

The fluid model that is used for the simulations is an incompressible model, which means that density fluctuations are only minor. Also, the response to the sine wave should be directly noticeable near the inlet and outlet. In figure 5.13b it can be seen that the finer grids converge faster and approximate the inflow profile better. At the start of the wave, it seems that all grids have reached a steady velocity. During the

wave, better results are obtained for the finer grids, however the profile is followed quite well in all simulations. After the sine wave, only the simulations with grid levels 6 and 7 require some convergence again.

A better review of the performance of the simulations on the different grids can be given by looking at the velocity near the outlet in figure 5.13b. The results for grid levels 5 and 6 are dismissed here, because they do not follow the sine wave and make the figure unclear, which could be expected based on the results from figures 5.9a and 5.10a. For grid level 7, it can be seen that there is a delay in the reaction to the sine wave, together with an overshoot. At the start of the wave, the solution is not converged and after the wave a relatively large overshoot can be seen. Grid level 8 follows the sine wave much better, however a higher response to the sine wave than expected can also be seen here. The finest grid performs best, which does have some fluctuations around the inflow sine wave. At the start of the simulation, the initial overshoot is highest for the finest grid. This can give problems for the lattice velocity, however this is not a problem in this test case.

For any deviations from the sine wave in the channel, density fluctuations are also expected. In figures 5.14a and 5.14b the middle of the channel is observed. Here, an average of the velocity is taken and a probe is placed in the middle for the density. A better comparison could be made if the averages of both are taken or if the values at the probe are taken, however the plots still show the expected density fluctuations. Especially for the coarsest grid simulations in the figures, the fluctuations in the velocity are clearly visible in the density plot. From this, it can be seen that a finer grid obeys the incompressibility condition much better compared to a coarser grid.

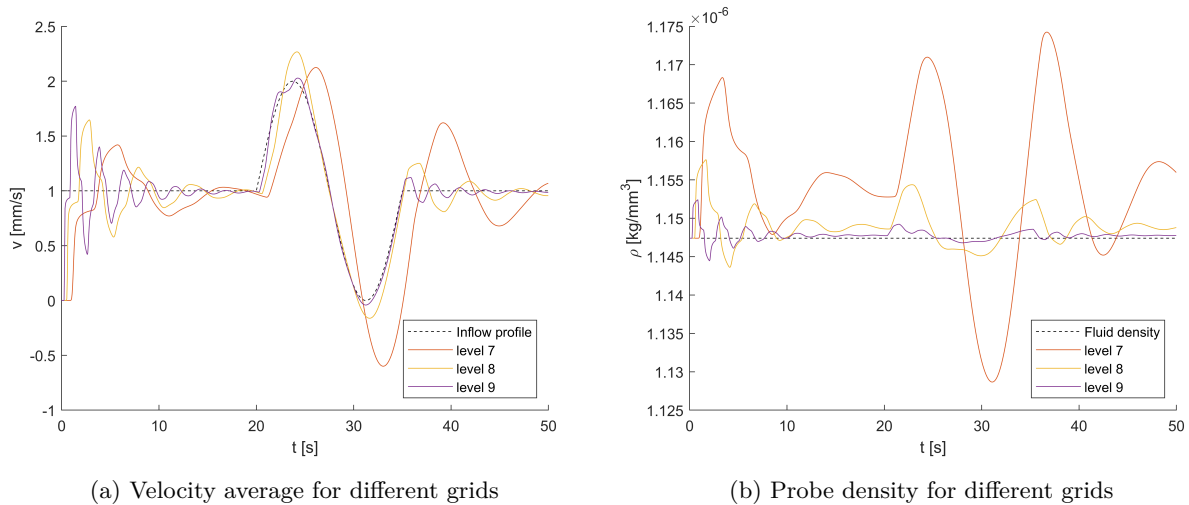


Figure 5.14: Channel values in the middle

## Chapter 6

# Right Hepatic Artery: models, results and analysis

The flow in the liver vasculature can become quite complex due to the transient flow and its behaviour in a complex geometry. Next to the yet unknown behaviour of injected radioactive particles in the blood, the liver vasculature is also highly patient specific. In this chapter, the flow in a simplified model of the Right Hepatic Artery (RHA) will be analysed. With the analysis of the flow, more insight in the flow is obtained and from these insights, the model can hopefully be expanded to a patient specific model in later research. The simplified model can also serve as a form of validation of future models, so an in-depth analysis of the flow can largely benefit future research.

The results in this chapter are valid for a simplified RHA with a Newtonian fluid called Blood Mimicking Fluid (BMF). In the work by Gijsen et al., flow differences between a Newtonian and non-Newtonian fluid in a carotid bifurcation model have been studied [71]. In this study, it was shown that the shear-thinning behaviour of blood has an impact on the velocity gradients in a cross section of the vessel. The dimensions are similar for the models in this chapter, so it can be expected that this assumption will have an impact on the velocity field. However, to study the flow field and resulting distributions of flow and eventually particles, in-vitro experiments are also performed with the fluid BMF. This substantiates the choice for this fluid for the simulations, since comparison is now possible.

In the simulations, the walls are assumed to be completely rigid. The used simplification is expected to have some impact on the flow behaviour, as vessel elasticity will make the pressure-drop non-linear. Including the elasticity of the walls will also make the simulations incredibly more complex regarding boundary conditions. Lastly, gravity is neglected in the model, which has an impact on the flow in the human body. The model is compared to experimental work which was placed horizontally and due to the placement, gravity is expected to have a small effect. Also, the RHA of a patient is oriented differently for each patient. For the simplified model, the gravity also makes the simulations complex and since the orientation is unknown, gravity can be neglected.

In this chapter, the details and results of the liver vasculature LBM simulations will be discussed. For validation of these results, in-vitro experimental work is performed at the University of Twente, of which the procedures will be discussed briefly.

### 6.1 Experimental setup

In this chapter, experimental results will be used for the validation of the simulations. The experimental setup will first be discussed shortly. The experimental work is conducted at the University of Twente by H. Mirgolbabaee, R. Kunst and E. Groot Jebbink, which is explained in detail in the MSc thesis by H. Mirgolbabaee [72].

Two pictures of the experimental setup are given by figure 6.1. In the simulations, two distinct models have been used that have different angles and outlets lengths. The given setup is similar for both models.

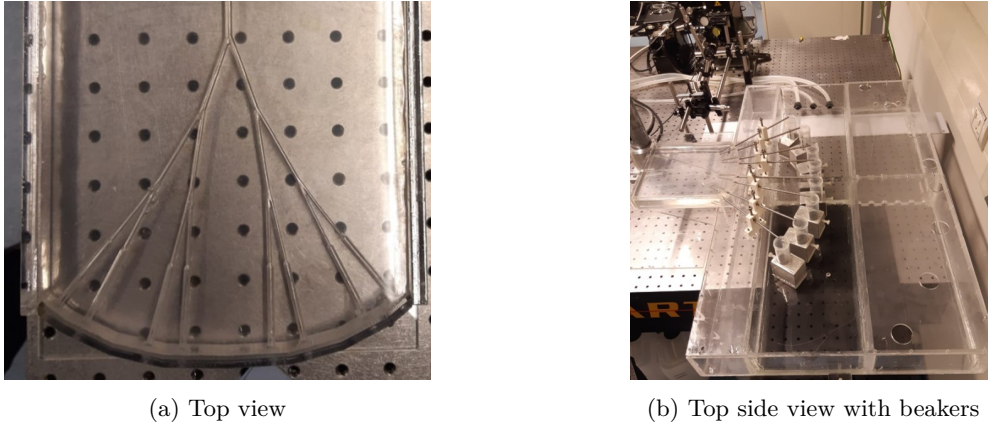


Figure 6.1: Experimental setup for the second model

The flow is pumped into the vasculature and measured at the inlet and outlets. A flow profile in the RHA is proposed by Aramburu et al [73], which is replicated by using two pumps. A hydraulic piston pump (SuperPump, ViVitro labs, Victoria, Canada) was used to generate the pulsatile flow and a gear pump (12V, Kavan, type 0190.121; Kavan GmbH, Nürnberg, Germany) was used to generate the steady flow. The cardiac cycle was measured in the liver phantom using a Coriolis MX55 flow sensor (Bronkhorst High-Tech B.V., The Netherlands), using an average over 30 cycles. The cycle that is generated in the liver phantom deviates a bit from the proposed profile due to the limitations of both pumps. Since the simulation is compared to the experimental data, the measured flow profile is used as the input for the simulation. The proposed flow and the measured flow can be found in figures 6.2a and 6.2b.

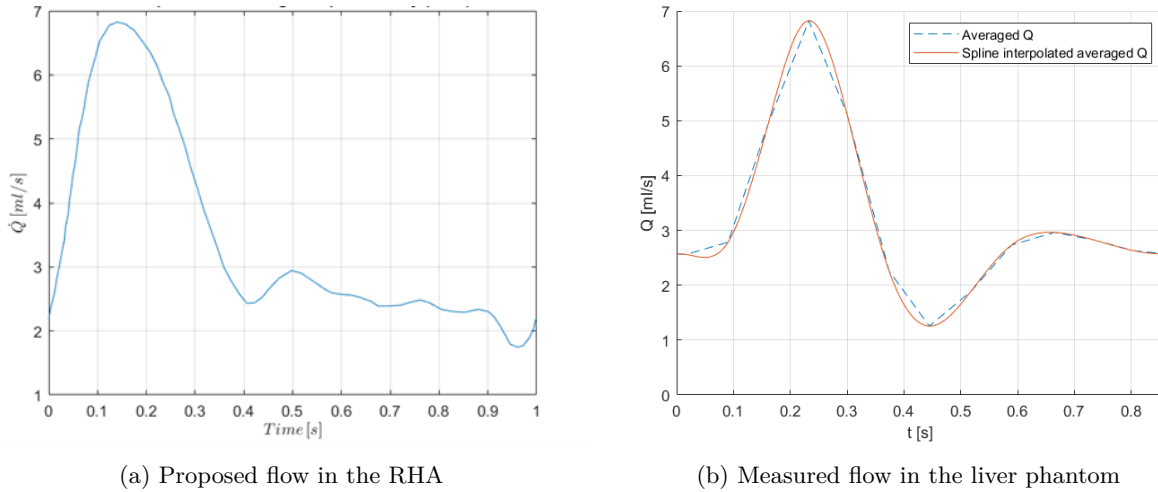


Figure 6.2: Proposed and measured flow in the RHA phantom

It can be seen that the measured flow is much smoother than the proposed flow, since abrupt changes in the flow rate likely require a more powerful pump. In the human body, the cardiac wave form is smoothed by the elasticity of the blood vessels [74]. The smoothing of the wave form due to the pump limitations could compensate a bit for the rigidity of the walls. Another difference between the proposed flow and the measured flow is the cycle rate of the flows, which are 60 BPM and 70 BPM respectively. The flow rate results of the experiments for both models will be given later in this chapter for validation of the numerical results.

## 6.2 Wide angle liver vasculature model

The first vasculature model that was used for the simulations is a plane symmetric model with three bifurcations. This model has bigger angles than the second model in this chapter, hence the name wide angle model. In figures 6.3a and 6.3b, a cross section of the model and the schematic of the model can be seen respectively. The  $x$ - $y$  plane is given here, with the horizontal  $x$ -axis and the vertical  $y$ -axis. A communication mistake resulted in the usage of this model, which is the mould of the model that is used in the first set of experiments, meaning they do not correspond. Still, the results of this model are shown here which will show that results can be obtained with a model with multiple outlets and thus it can be seen as a specific test case. It also shows that flow in an even smaller model is possible with Musubi, which means that the model could be extended to an even smaller scale. It should be noted that a Newtonian fluid is used that mimics blood and that at a very small scale this mimicking is not realistic anymore.

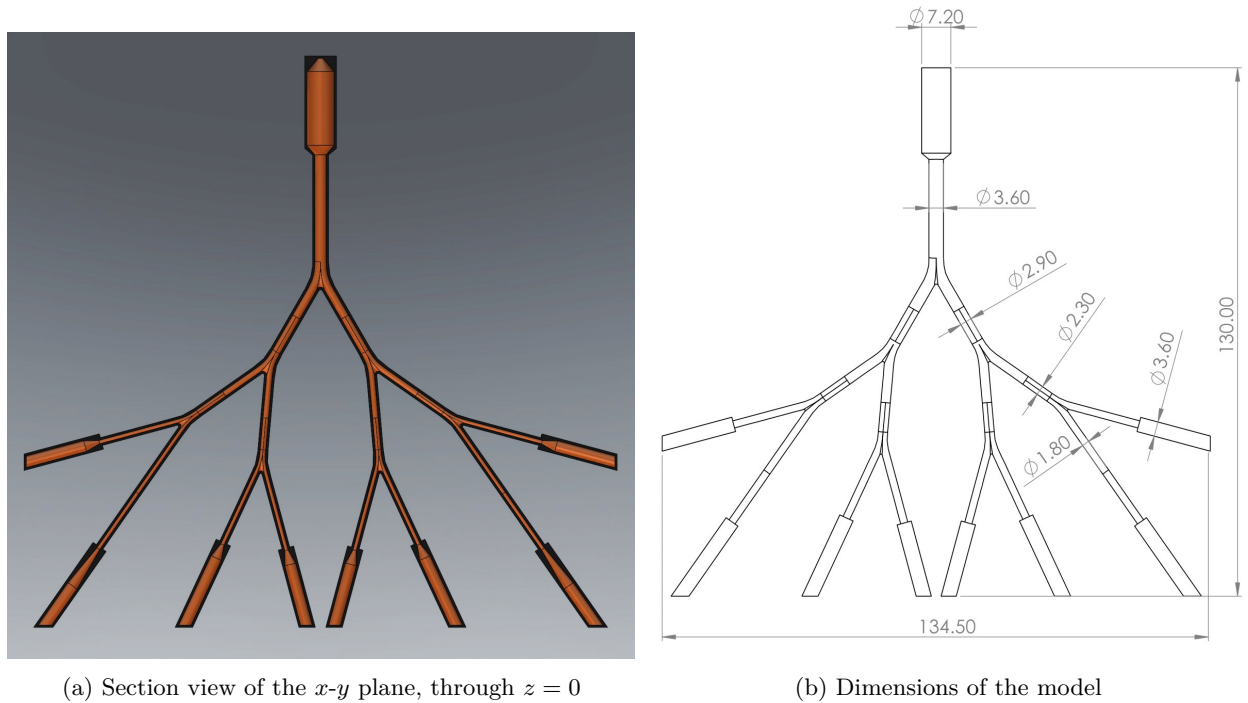


Figure 6.3: Liver vasculature model 1

In figure 6.3a, it can be seen that the inlet and outlets of the model are closed off. For the simulations, boundary conditions were placed on the inside of the model, effectively cutting off some parts of the model and transforming the model to an open model. For the inlet, a larger part of the top of the model was cut off to remove the loft.

The dimensions can be found in figure 6.3b, which are the outer dimensions. The inner dimensions can be found in table 6.1, together with the angles of bifurcation. The angle here is defined by comparing the main vessel to either one of the smaller vessels in which the main vessel branches off. The model is symmetric in the vertical axis through the middle, but also locally in each bifurcation, since the angle of bifurcation is equal on both sides. This also means that the angle between the two smaller resulting vessels is exactly twice the bifurcation angle.

Parameter	Value	Parameter	Value
$D_{in}$	6.2 mm	L	134.5 mm
$D_{out}$	2.6 mm	H	130.0 mm
$D_1$	2.6 mm	$t_{wall}$	0.5 mm
$D_2$	1.9 mm	$\alpha_1$	30°
$D_3$	1.3 mm	$\alpha_2$	25°
$D_4$	0.8 mm	$\alpha_3$	20°

Table 6.1: Dimensions of the vasculature model

Parameter	Value
$\rho$	$1.1474 \cdot 10^{-6} [kg/mm^3]$
$\mu$	$4.3100 \cdot 10^{-6} [kg/(mm \cdot s)]$
$\omega$	1.9 [-]

Table 6.2: Parameters for the LBM simulations

At the outlets, a zero pressure boundary condition is imposed. Here, an extrapolation method is used to obtain the prescribed pressure value, where the distribution function at the boundary is obtained by extrapolation by using the known distribution functions at two neighbouring points according to Junk et al. [75]. The parameters and fluid properties that are used in the simulations are given by table 6.2. The fluid properties were already tested in the channel test case and thus the geometry and the velocity value and profile are the only changes relative to that model. The properties in the table will be used in all the simulations in this chapter.

At the inlet, the velocity is prescribed by using a velocity bounce-back condition. The flow profile from figure 6.2b is used together with the area of the inlet to obtain the velocity profile that is prescribed at the boundary, given by figure 6.4. The first 2 seconds of the profile are steady, which is used for the convergence of the simulation. After one cardiac cycle is completed, a steady flow is introduced again to see if fluctuations after the cycle occur. If the flow is largely laminar, then it is unlikely that these fluctuations will occur. If they do occur, this means that it does not suffice to only simulate one cycle and extrapolate these results, which makes the simulations computationally much more expensive.

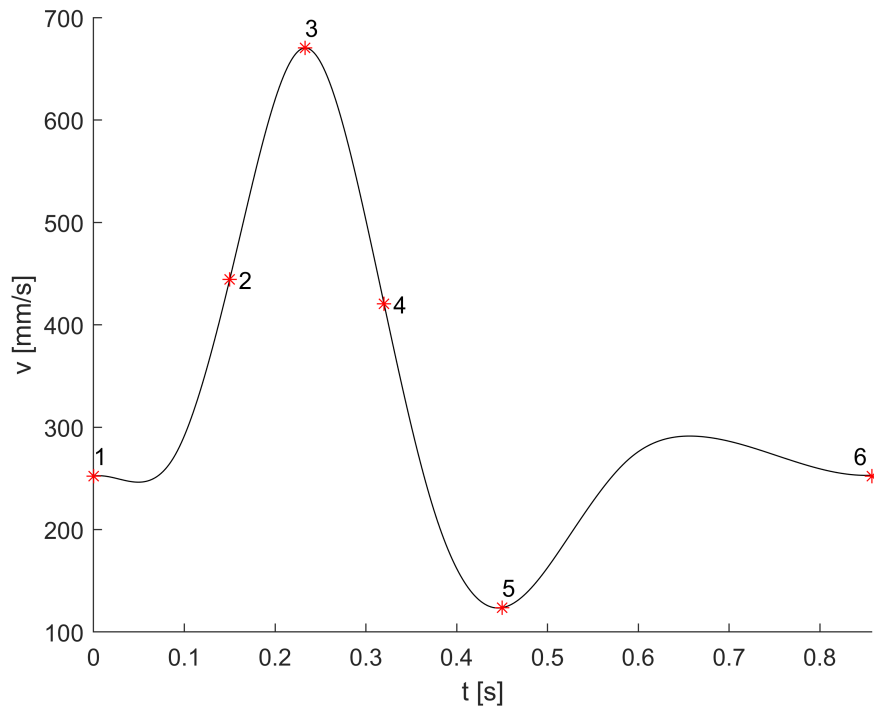


Figure 6.4: Velocity profile at the inlet

In the velocity profile figure, the flow analysis will be conducted at a few different time instances, which are given in the plot, with the exact values and names given by table 6.3. The choice of these locations is not arbitrary: points 3 and 5 are the minimum and maximum values of the velocity and points 2 and 4 are the maximum values of the acceleration of the flow, which should be sufficient to show all the characteristics of the cardiac cycle and resulting flow in the vasculature. During deceleration of the flow, the most drastic changes to the flow field are expected. Once the flow is decelerated, the pressure increases with the flow, which is called an adverse pressure gradient. With an adverse pressure gradient present, instabilities like flow reversal and flow separation occur, which have the biggest influence on the shape of the flow field.

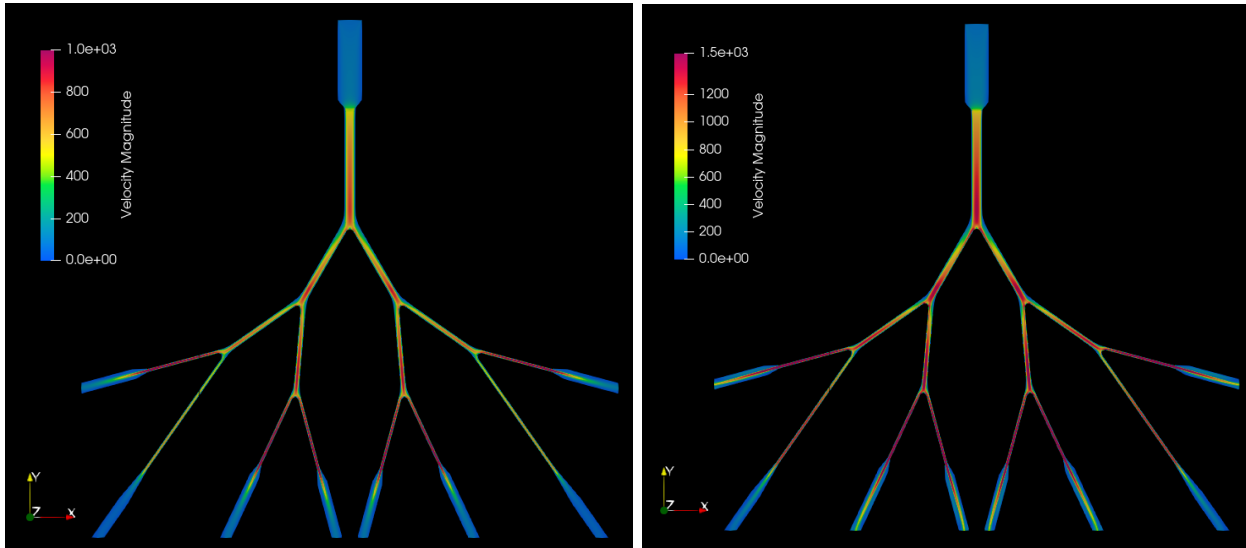
Index	Name	$t$ [s]
1	start	0.0
2	acceleration	0.15
3	peak systole	0.23
4	deceleration	0.32
5	peak diastole	0.45
6	end	0.86

case	$dx$ [mm]	$dt$ [s]	N
1	0.0055	$1.38 \cdot 10^{-6}$	$23.1 \cdot 10^6$
2	0.005	$1.13 \cdot 10^{-6}$	$35.5 \cdot 10^6$
3	0.004	$7.29 \cdot 10^{-7}$	$58.4 \cdot 10^6$

Table 6.4: Simulation details

Table 6.3: Important time instances in the cardiac cycle

Now, the model is fully defined and the mesh can be generated, which defines the element size  $dx$  and the time step  $dt$ . In chapter 4.2 it was already discussed how to calculate the minimum required element size. Also, decreasing the element size will in general reduce the numerical error made in the simulation, but it will increase the simulation time. For the results in figures 6.5 to 6.8, the case 2 in table 6.4 is used.



(a) 2D velocity field at the start of the cardiac cycle (b) 2D velocity field during deceleration in the cardiac cycle

Figure 6.5: Planar velocity field at two time instances, in  $mm/s$

In figures 6.5a and 6.5b, the velocity field of the model is given for two time instances. This velocity field is obtained by considering the  $x-y$  plane, through  $z = 0$ . Looking at figure 6.4, it can be seen that the inlet velocities for these two time instances are about  $60 \text{ mm/s}$  and  $100 \text{ mm/s}$  respectively. Because of the narrowing just after the inlet, the velocity is generally much higher in the rest of the model. As the fluid approaches the bifurcation, the velocity decreases due to the wall and the resulting rise in pressure. After the bifurcation, the flow tends to Poiseuille flow if the length of the vessel is long enough. In this model, the flow

velocity increases relatively quite a lot in the later branches because of the relatively small diameter. The diameters in this model are not realistic according to Murray’s law, which states that in an optimal vascular system the cube of the radius of the parent vessel is equal to the sum of the radii of the daughter vessels, such that flow is obtained with the least biological work [76]. A generalisation of Murray’s law is given by the equation below:

$$r_p^\gamma = r_1^\gamma + r_2^\gamma \quad (6.1)$$

The amount of biological work is a trade-off between energy dissipation for the blood transport due to the viscosity and metabolic costs for maintaining the vascular walls [77]. Here, the assumption of laminar Poiseuille flow results in Murray’s law, where  $\gamma = 3$ . Depending on the blood flow and the desired vasculature form, other values have also been reported in the human body, with for example  $\gamma = 2.7$  at locations with a very small vascular wall thickness. An ideal model for the right hepatic artery is assumed to have Murray’s law properties. Conclusions based on this model are therefore less representative of flows in an actual vasculature. The vessels in the later models in this chapter are designed in such a way that they approximately obey Murray’s law, which means that they represent a more realistic vasculature, albeit simplified.

To review the numerical results, the inflow and outflows will be analysed first. Any inequality in inflow and outflows either means an error in the model, or numerical inaccuracies. In figure 6.6, the tracked velocities at the start of the simulation and during the cardiac cycle are given.

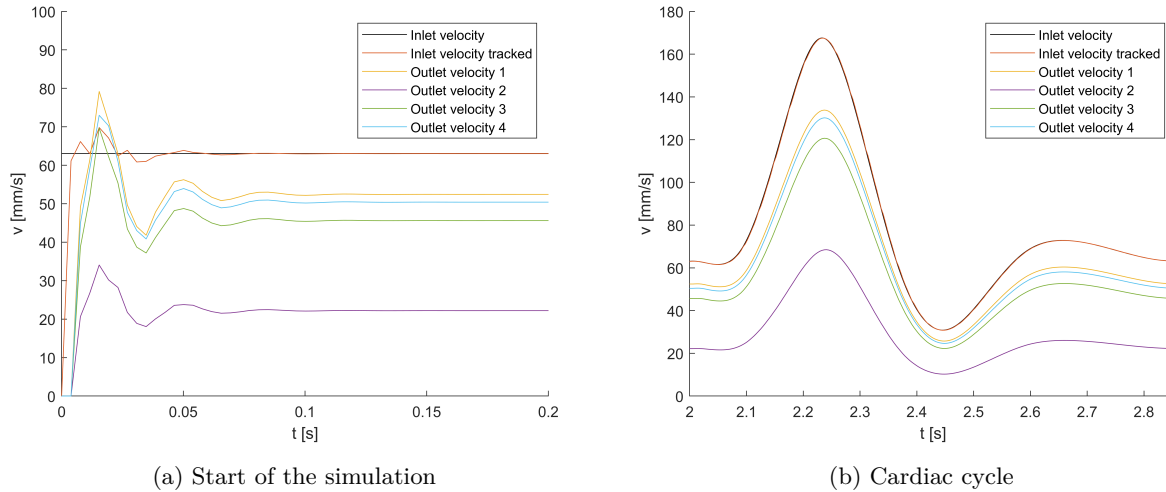


Figure 6.6: Tracked velocities near the inlet and outlets during startup and the cardiac cycle

The velocity at the start of the simulation gives information about the convergence to a steady solution of the simulation. The initial response in LBM simulations was already investigated in the test cases in the previous chapter and a similar response is observed here. After 0.2 seconds, it can be seen that the solution has already converged quite well. A choice was made to start the cardiac cycle after 2.0 seconds for convergence purposes, however while it is a safe choice, some computation time could have been saved by starting the cycle earlier.

In both figure 6.6a and 6.6b, the inlet velocity is given as an input and it is also tracked some distance away from the inlet to check if the velocity boundary condition works as expected. Initially some fluctuations are visible, but after convergence the tracked inlet velocity follows the imposed inlet velocity perfectly. Also, only four of the eight outlets are given in both figures, since the model is symmetric and the same values are expected for the other corresponding outlets, which is shown in figure 6.7.

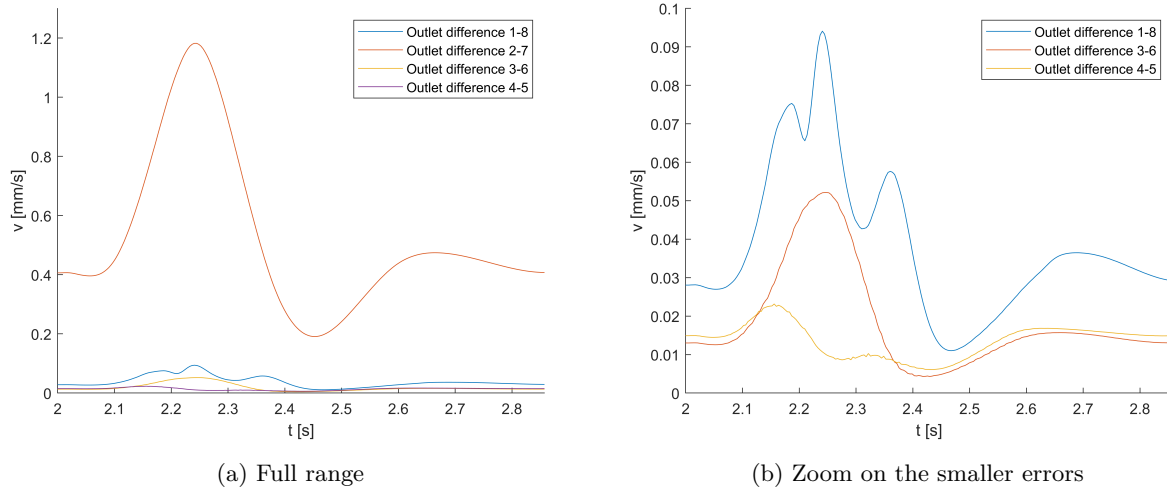


Figure 6.7: Difference between the symmetric outlet velocities during the cardiac cycle

From figure 6.7, it can be seen that the difference between the symmetric outlet velocities is very small. For outlets 2 and 7, this difference is significantly larger compared to the other outlets. There are various possibilities which could cause this difference, like the placement and the type of boundary conditions, the tracking of the velocity or the mesh generation, which could not be entirely symmetric. A symmetry check of the model in SolidWorks also shows a slight asymmetry in the smaller vessels towards outlets 2 and 7, however it has not been verified if this asymmetry causes this velocity deviation. The difference is about 2% of the total velocity and it does not result in a visible difference in the outflow plot over the whole cardiac cycle, given by figure 6.8.

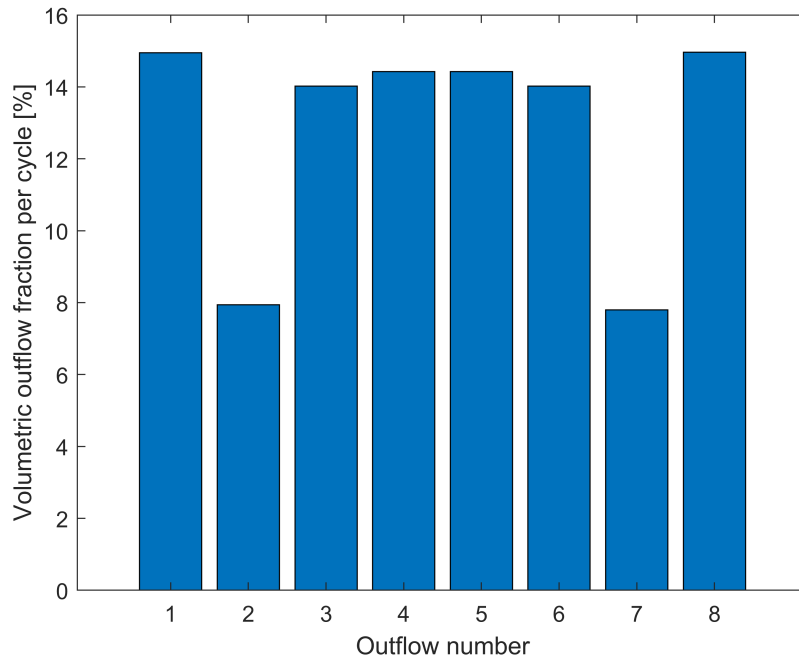


Figure 6.8: Outlet outflow fractions, calculated over the entire cardiac cycle

In this figure, it can be seen that the outflows from outlets 2 and 7 are much lower compared to the other outflows. This difference can be explained by the longer path to these outlets and the same zero pressure boundary condition. For this model, a grid refinement study was carried out to show the numerical convergence. The results of this can be found in figure 6.9.

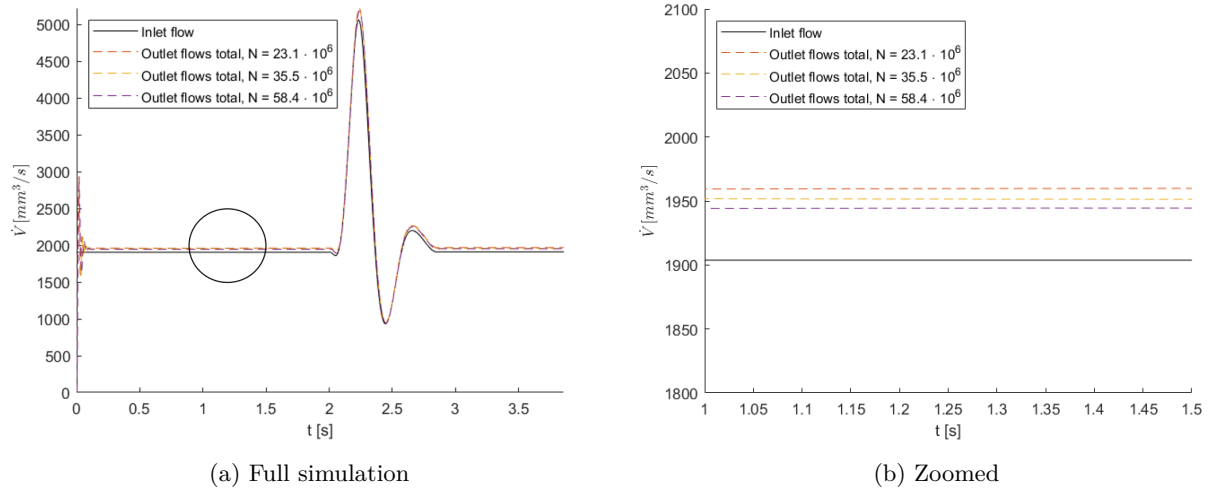


Figure 6.9: Tracked outflows for different grids for the whole simulation

In figure 6.9, the outflow results over the entire simulation range can be found. The initial phase is the startup phase, to ensure a converged solution before the cardiac cycle starts. After the cardiac cycle, the simulation returns to the steady velocity from the start-up, which is used to check if there are any visible effects of the cardiac cycle after the cycle has ended. If multiple cardiac cycles are simulated, this last region is replaced by another cardiac cycle, which is at  $t = 2.86s$ .

From these figures, it looks like the solution is converging and this plot was initially used to determine if the earlier discussed results were accurate enough. However, this plot alone does not suffice to check convergence. The outflow is calculated by taking all the values of the velocity on a plane, summing these values and taking the average. By multiplying this result with the area of an outlet and summing the results of all outlets, the total outflow is calculated. By adding more elements to a simulation, in general a solution with a smaller numerical error is obtained. What also happens here is that more elements are added to this plane, which makes the approximation of the outflow better, since more elements are used to calculate the average velocity. For future simulations, the convergence will also be tested by using pressure or velocity point data and comparing the results at the same point for multiple grid sizes.

### 6.3 Wide angle liver vasculature model, corrected geometry

As mentioned in the previous section, the model used for the first vasculature simulations was the mould model of the actual model. This means that the outer diameters in figure 6.3b are the inner dimensions of the new model. The new model can be seen in figure 6.10.

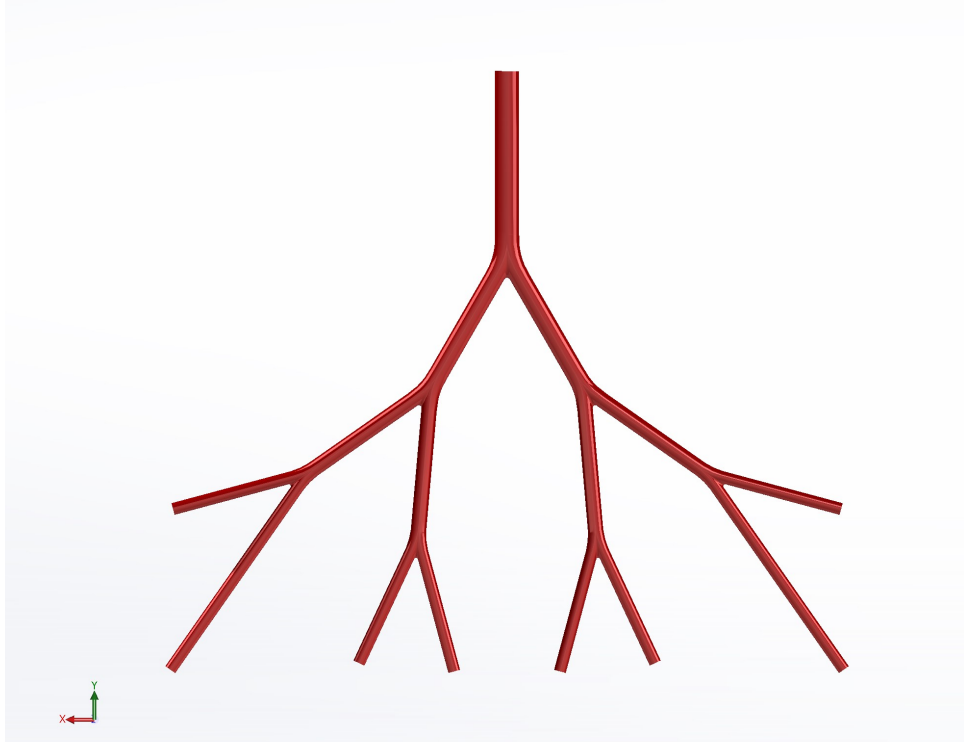


Figure 6.10: Front view of the vasculature model with the updated geometry

The dimensions of the new model can be found in table 6.5. Comparing this table to table 6.1, it can be seen that the corresponding diameters are exactly 1 mm larger than in the previous model. The length and height of the model are a bit shorter since the outer parts of the previous model are cut off. The updated model has no thickness, which is not realistic for a real model, however in these simulations this is not a problem. The thickness only becomes important if there is flow around the geometry and if the wall is not rigid. The radii that are used in this model approximately follow Murray's law, which also makes it more realistic compared to the previous model. Next to approximately following Murray's law, the model is designed in such a way that the inlet area is exactly half of the sum of the outlet areas. For incompressible flow this means that the mean velocity at the outlet is approximately half the mean inlet velocity with an approximately equal flow distribution over all the outlets. Compared to the previous model, it is expected that the velocity will decrease after each bifurcation, as the area before the bifurcation is always larger than the total area after the bifurcation.

Parameter	Value	Parameter	Value
$D_1$	3.6 mm	L	102.5 mm
$D_2$	2.9 mm	H	90.0 mm
$D_3$	2.3 mm	$\alpha_1$	30°
$D_4$	1.8 mm	$\alpha_2$	25°
$t_{wall}$	[-]	$\alpha_3$	20°

Table 6.5: Dimensions of the corrected vasculature model

case	dx [mm]	dt [s]	N
1	0.024	$1.38 \cdot 10^{-6}$	$102 \cdot 10^6$
2	0.022	$1.16 \cdot 10^{-6}$	$132 \cdot 10^6$
3	0.020	$9.59 \cdot 10^{-7}$	$176 \cdot 10^6$

Table 6.6: Simulation details

Although the model is quite similar to the previous model, the dimensions have changed quite a bit and a grid refinement study is again required to investigate the numerical convergence of the solution. In table 6.6 the simulation details can be found regarding element size, time step and the number of elements. A relatively large amount of elements is used for these simulations compared to the previous model, which was initially expected to be required because of the increased diameters in the model. Because of the increase in diameters, the velocity in the vessels also decreases and this means that a larger element size can be used for keeping the lattice velocity below the limit. The flow results of these simulations can be found in figure 6.11. Note that  $1000 \text{ mm}^3/\text{s}$  is 1 mL.

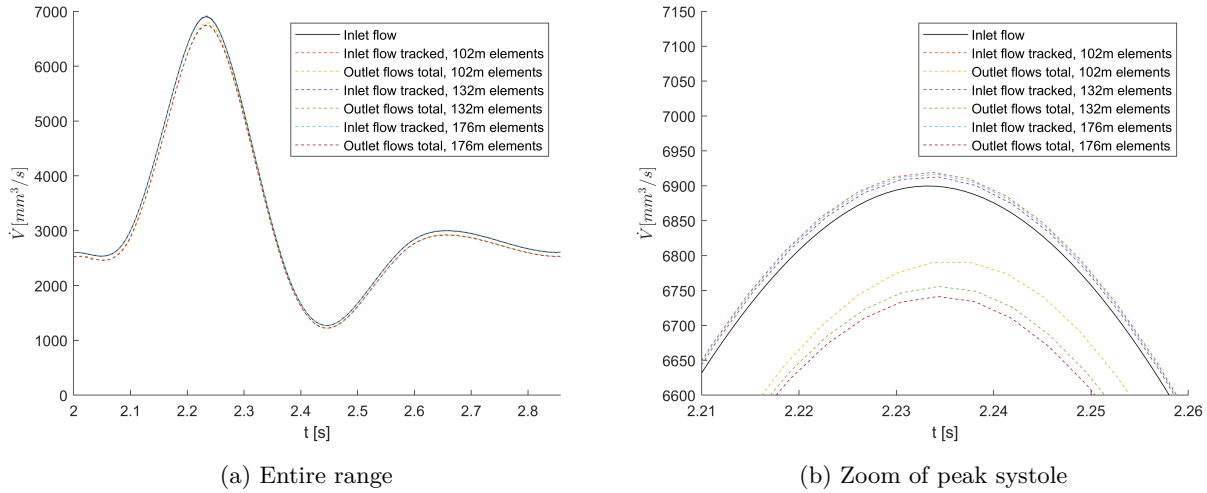


Figure 6.11: Cardiac wave, input and tracked flows

Again, it seems like a better solution is observed by using a finer grid. The approximation of the outflows here are not entirely precise however. In this model, the outlets are not horizontal or vertical. To track the velocities here, a skewed plane was used and the average velocity was taken. In a structured grid, a plane can be used for tracking if it is horizontal or vertical, however at an angle a sort of staircasing effect is observed, which can be seen in figure 6.12.

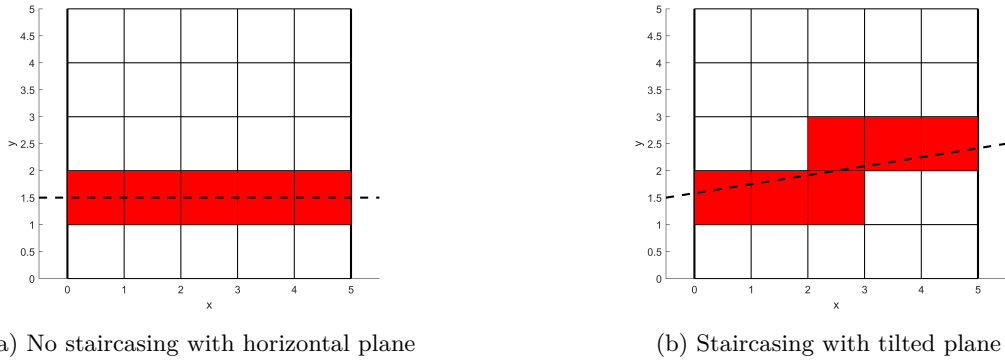


Figure 6.12: Example of the staircasing effect in tracking

The average is taken over all the elements that intersect with the plane, which is different for the two cases in figure 6.12. In the example, the difference in average velocity for both cases is very large because of the large contribution of each element to the average. In practice, this difference will be smaller but most likely still noticeable. A better approximation of the outflows can be realised by adding more points to calculate the average velocity. Increasing the number of points on a plane is only possible by decreasing the element size, so an alternative can be used by calculating the average velocity in a volume instead of a plane. By using this method for tracking, the staircasing effect is also decreased.

Another method to check the convergence is by placing probes at some locations, as was discussed in the previous section. For this model, three probes were placed near the first bifurcation, as can be seen in figure 6.13. The numbering of the probes increases for larger distance from the outlet. For example, probe 1 is located in the middle of the model, just before the first bifurcation.

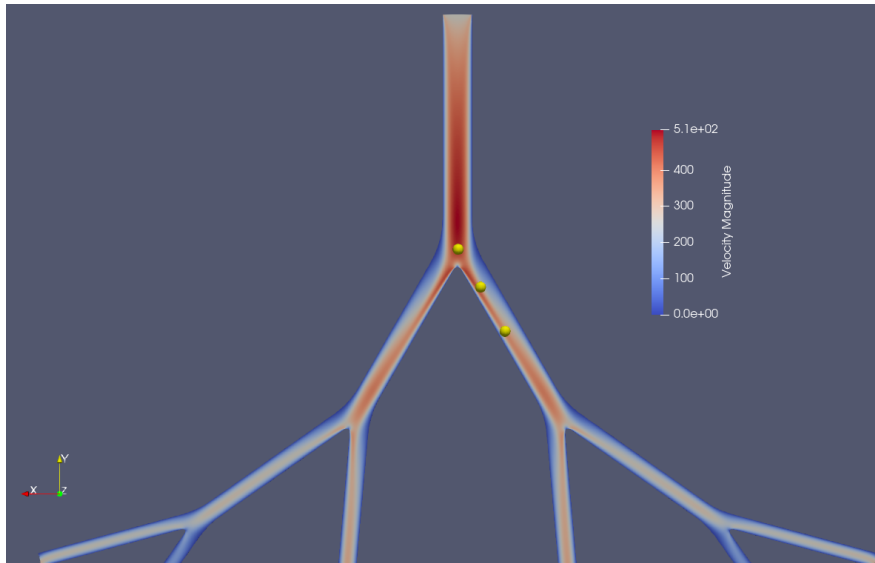


Figure 6.13: Velocity and pressure probe locations in the vasculature model, with the velocity field in  $mm/s$

The results for both the pressure and the velocity at these probes for the different grid sizes in table 6.6 can be found in figures 6.14a and 6.15a.

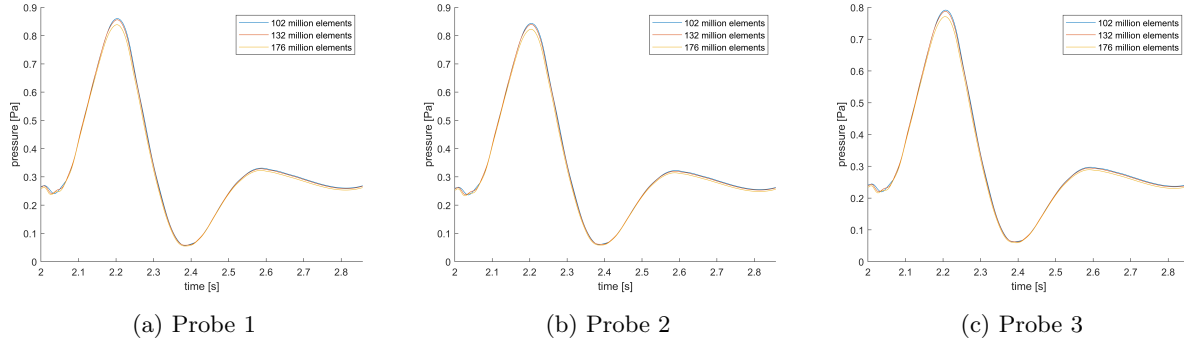


Figure 6.14: Pressure at probes over one cardiac cycle for different grids

In the pressure plots in figure 6.14, the two coarsest grids give a similar probe pressure for all three probes over the whole cardiac cycle. The finest grid deviates a bit from this pressure, which gives a slightly lower pressure at all three probes during the cardiac cycle. A possible explanation could be given by the boundary conditions, which causes a different pressure propagation through the vasculature for a different grid. Here the placement has a large influence, which will be shown in more detail for the next model. Also, the outlets do not have the same length, which could also cause this boundary condition problem and the resulting pressure difference. It is possible that the observed effect is a difference caused by the convergence, however based on the small difference between the first and the second grid relative to the third grid, this is unlikely.

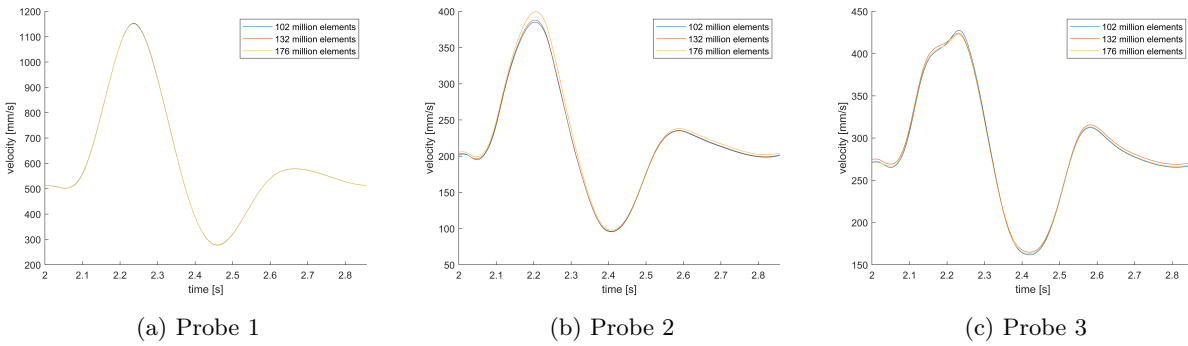


Figure 6.15: Velocity at probes over one cardiac cycle for different grids

The velocity plots in 6.15 show that the difference in pressure values does not always result in a difference in velocity. For example, the pressure difference for the finest grid at the first probe is not observed in the velocity at this probe. For flow in the vasculature, a pressure difference is required, which means that a single pressure value cannot be linked to a velocity difference. For the second probe, a velocity difference is visible for the entire cardiac cycle, which could be explained by the boundary condition. While there is a velocity difference for the finest grid at the second probe, this difference is not observed at the other two probes and it can be assumed that the results of the second grid are accurate enough to represent the flow. The resulting outflow deviations from the average outflow of this simulation can be found in figure 6.16a. Next to this figure, the experimental results are given for comparison.

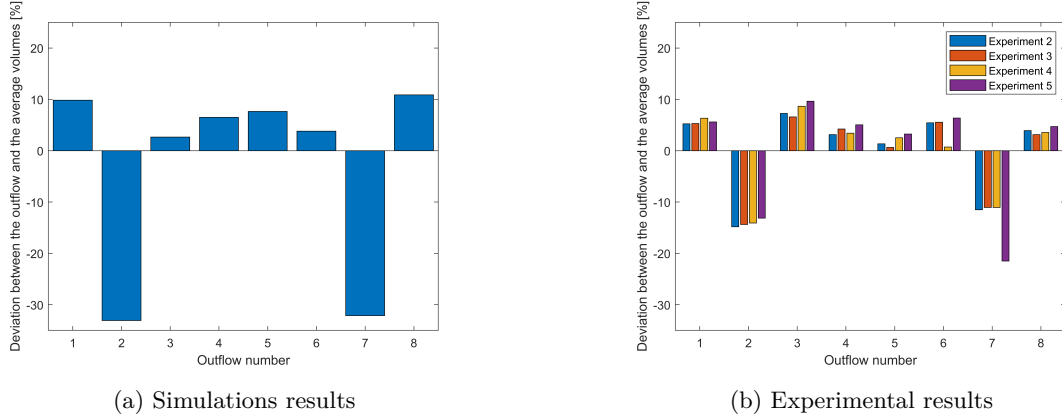


Figure 6.16: Outflow deviations from the average outflow given by equation 6.2

The outflow deviation from the average outflow  $\delta$  is calculated by using equation 6.2.

$$\delta = \frac{V_{out} - V_{avg}}{V_{avg}} \cdot 100\% \quad (6.2)$$

In the equation,  $V_{out}$  is the tracked outflow and  $V_{avg}$  is the total inflow or outflow divided by the number of outlets, which is 8 in this model. In both the experimental results and simulation results, a smaller outflow in outlets 2 and 7 is observed. However, the simulations show a much larger deviation from the average than the experiments. In figure 6.17 the velocity field of the vasculature at the start of the cardiac cycle is given.

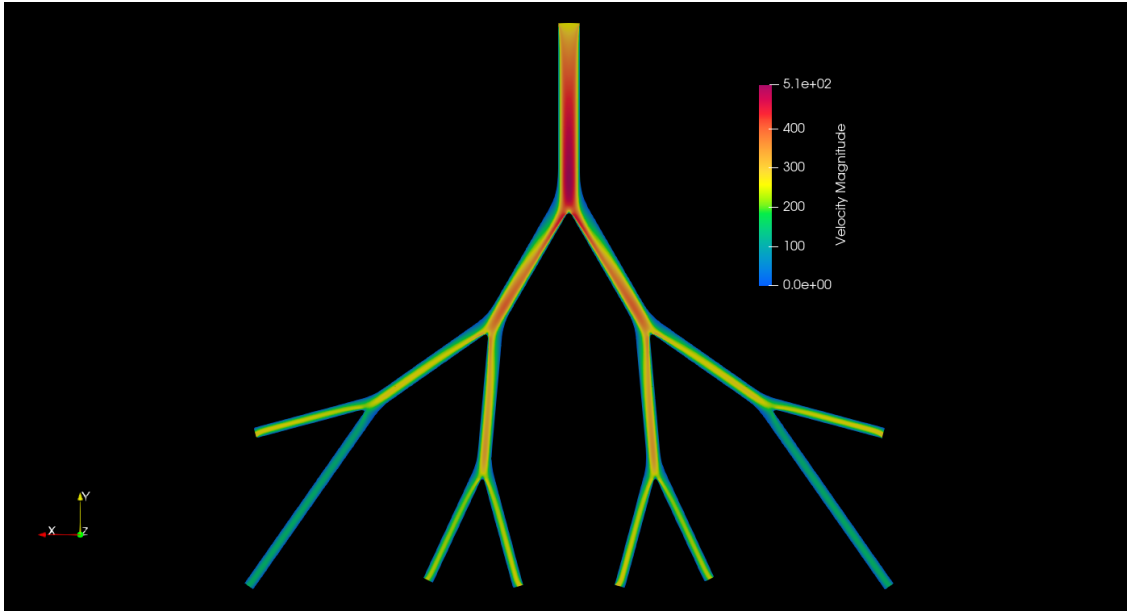
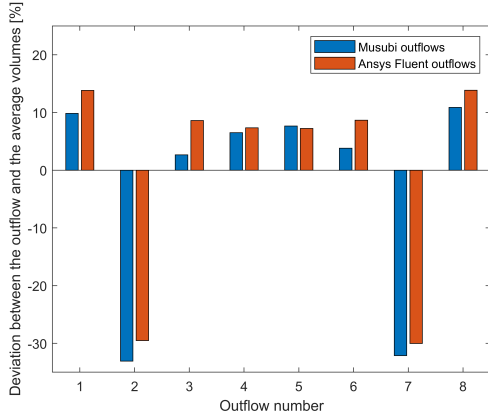
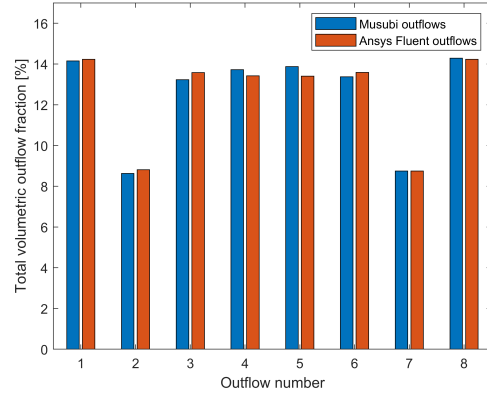


Figure 6.17: Velocity magnitude at the start of the cardiac cycle for case 1, in  $mm/s$

The velocity in the vasculature decreases after each bifurcation, which was expected from the increase in area after each bifurcation. However, the velocity in outlets 2 and 7 is relatively low, which is expected from the given outflow plots. In figure 6.18 the outflow deviation and outflow fractions of the Musubi simulation are compared to the Ansys Fluent simulations that are performed by Ghent University.



(a) Outflow deviations from average outflow



(b) Total outflow fractions

Figure 6.18: Musubi and Ansys Fluent simulation comparison on outflow deviation and total volumetric outflow fraction

The trend in the Musubi and Ansys simulations is much more similar than what is observed in the comparison with the experimental outflows. In the Ansys simulations, a similar zero pressure boundary condition is used. From this, it can be assumed that the simulations perform as well as could be expected with this type of boundary condition. One of the options to solve this problem is to impose a pressure boundary condition is a specific non-zero value, however for this the pressure from the experiments should be known. Here, an analytical derivation of the pressure could be a possibility, however this can become quite complex [78]. Instead, experiments were conducted with a new vasculature model with outlets that all have the same length. In the next section, the simulation results with this new model will be discussed.

## 6.4 Small angle liver vasculature model

With the updated model, the outlets all have the same length and problems with the pressure boundary condition should be solved. Also, the bifurcation angles of the new model are smaller for all three bifurcations. A front view of the updated model can be found in figure 6.19, with the new dimensions listed in table 6.7.



Parameter	Value
$D_1$	3.6 mm
$D_2$	2.9 mm
$D_3$	2.3 mm
$D_4$	1.8 mm
$t_{wall}$	0.1 mm
L	150.0 mm
H	120.5 mm
$\alpha_1$	20°
$\alpha_2$	12°
$\alpha_3$	6°

Figure 6.19: Front view of the new vasculature model Table 6.7: Dimensions of the new vasculature model

The model in figure 6.19 was created in SolidWorks and it is the second version of this model. Initially a similar model was used, however due to some modelling issues in SolidWorks it took a lot of time and computation power to get a working simulation. The results can be found in Appendix A, in which it is apparent that there is a mistake in the simulation. To get a working model, a very fine mesh was used and the relaxation frequency value was adjusted such that the simulation worked. From the results, it seems like the model is leaking at some location, since there is a large difference between the inflow and outflow. After remodelling, the simulation required less elements and the relaxation frequency could be changed back to the original value of  $\omega = 1.9$  that is used in all simulations. Tuning the relaxation frequency could in some cases result in a working simulation, however this is a circumvention of the problem without solving the problem.

With the updated model, the results improved a bit, however still some strange results were observed initially. In the previous model but also from the vasculature with the old angles in the previous section, some very fine were used and initially, convergence seemed to be the problem. Some very fine grids were used and the outflow fractions changed for each simulation. For a very fine grid with about 389 million elements, the result of the fractional outflow in one cardiac cycle can be found in figure 6.20. The tracked inflow and outflows can be found in figure 6.21 for the same grid over the cardiac cycle.

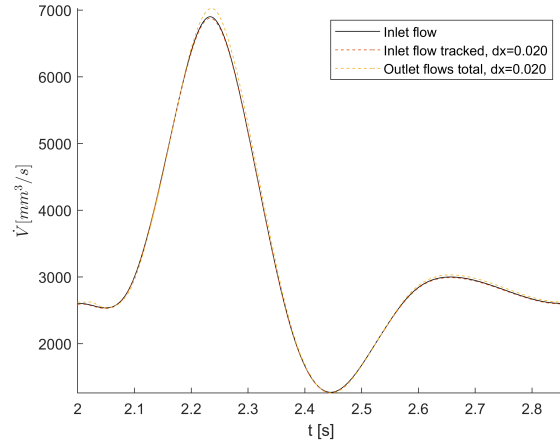
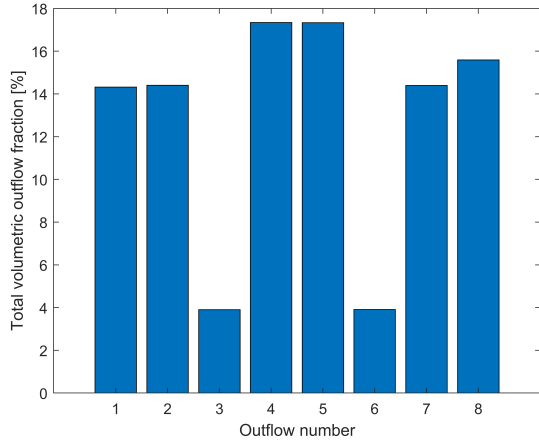


Figure 6.20: Fractional outflows with  $dx = 0.018$

Figure 6.21: Tracked inlet and outlet flows over the cardiac cycle

From figure 6.20, it can be seen that outflows 3 and 6 are very low for this very fine grid, which is not expected when analysing the model. Also, there is a difference between the outflows at outlets 1 and 8, which should not be observed in a symmetric model. In figure 6.21 the tracked inflow and outflows are given and while there is a difference between the inflow and outflow, this difference is much smaller compared to the outflows that the simulations with the wrong model produced. Still, there is an error in the model that should be resolved. Previous results were largely influenced by the wrong model, so first the model was analysed in attempt to resolve the error.

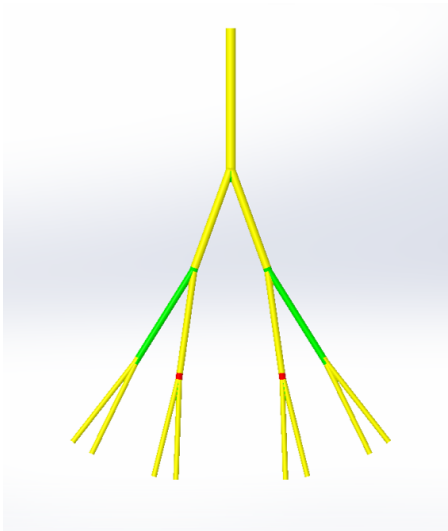


Figure 6.22: Symmetry check in the vertical axis of the model

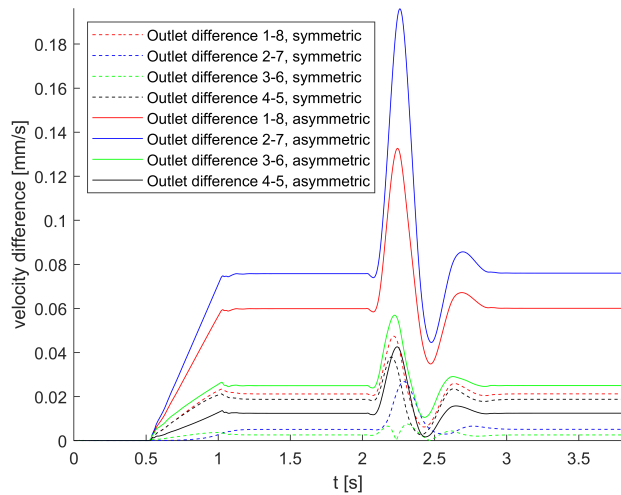


Figure 6.23: Velocity differences between the outlets for the symmetric and asymmetric model

In figure 6.22 a symmetry check of the model can be seen. The symmetry check is a tool in SolidWorks which identifies similar surfaces based on a symmetry plane. In the figure, the yellow surfaces are symmetric, which means that the surfaces are identified to be similar on the left and right side of the plane and they also have the same dimensions. The green surfaces in the figure are not symmetric, which means that SolidWorks does consider the surfaces to correspond, however it does find different dimensions. The red surfaces in the figure are unique faces, which means that SolidWorks does not find corresponding surfaces on both sides of

the plane. While it looks like those surfaces should correspond, the modelling is done in a slightly different way in the model, which results in two defined surfaces at this location on the left side of the plane and one defined surface at this location on the right side of the plane. These unique surfaces do not mean that this location is asymmetric.

While an asymmetry is detected, the model does look symmetric and the asymmetry seems to be small. The model has been cut in half and mirrored in the symmetry plane to obtain a symmetric model. Similar simulations were performed using both models and the results can be found in figure 6.23 in an attempt to quantify this asymmetry. In this comparison, both the simulation with the symmetric and the asymmetric model have an element size of  $dx = 0.038$ . The rest of the simulation details are given in table. 6.8.

In the ideal case with the symmetric model, the difference between the velocities in the symmetric outlets should be equal to zero. The result of the asymmetry should especially be observed in the difference between outlets 1 and 8, and also 2 and 7. In the figure, the biggest difference between the symmetric case and asymmetric case is in this outlet difference, so it can be concluded that there is indeed an asymmetry that could influence the results. Deviations are also observed in the other outlet velocities differences, which can be explained by the pressure boundary condition. If the length or the diameter is changed, the pressure gradient also changes. For instance, if the outlet becomes shorter due to the asymmetry, then near the bifurcation the pressure will not be equal and flow tends to go into the vessel with the lower pressure.

Although there is an influence by the asymmetry, this cannot explain the results in figure 6.20. From some further analysis using the symmetric model, a tracking error was found at outlet 8. While the definition of the tracking was similar at the other outlets, the error only occurred at outlet 8. Defining the same region in a different way solved the error, which gives the results in figure 6.24. In this figure, a grid with about 69 million elements is used, which is much lower compared to number of elements used for the finest simulation with the asymmetric model.

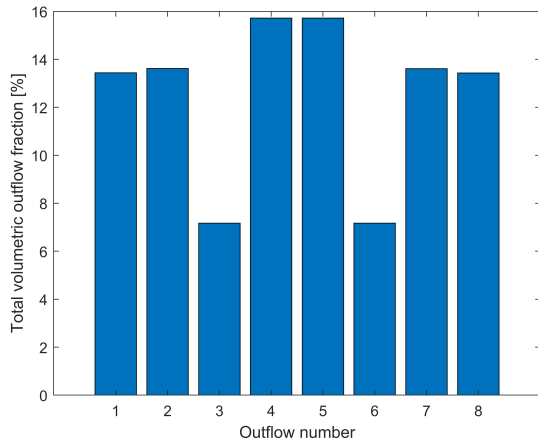


Figure 6.24: Fractional outflows with  $dx = 0.032$

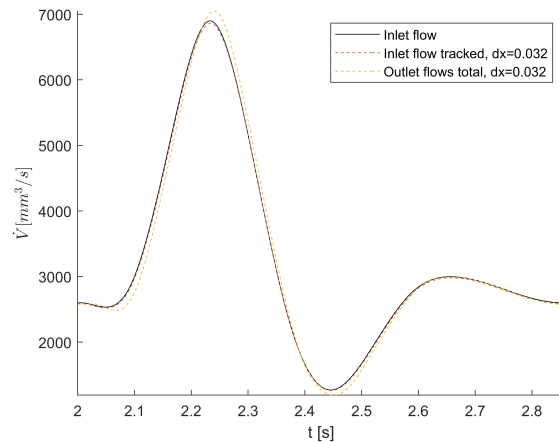


Figure 6.25: Tracked flows with  $dx = 0.032$

In the figure, it can be seen that the results are symmetric now, however this is mainly due to the fixed outlet tracking at outlet 8 and not due to the new symmetric model. Another difference between figure 6.20 and 6.24 is the volumetric outflow fraction at outlets 3 and 6, which is much lower for the finer grid. It seems that this difference becomes larger if the grid becomes finer, which is either a convergence issue or another problem in the simulation. In figure 6.25 the tracked inflow and outflows are given for the finest grid in table 6.8. The maximum difference between the inflow and outflow is about 2.5%, which can be explained by some compressibility, by the calculation of the average velocity or the numerical convergence of the simulation, which also influences the former two reasons. The tracking for these simulations is done by tracking points in a volume instead of on a plane as in the previous simulations, so the calculation of the average velocity

should be more accurate. Some simulations with coarser grids were performed to check the convergence, which can be found in table 6.8.

case	dx [mm]	dt [s]	N
1	0.038	$3.46 \cdot 10^{-6}$	$41.3 \cdot 10^6$
2	0.035	$2.94 \cdot 10^{-6}$	$52.9 \cdot 10^6$
3	0.032	$2.45 \cdot 10^{-6}$	$69.2 \cdot 10^6$

Table 6.8: Simulation details

Probe	x [mm]	y [mm]	z [mm]
1	33.0	0	0
2	43.5	0	-4.0
3	52.4	0	-7.3
4	62.4	0	-10.75

Table 6.9: Probe locations

Instead of using the outflows to investigate the convergence of the different grids, velocities at some probes were used. The probe values can be found in table 6.9, which are also plotted as yellow dots in the vasculature given by figure 6.26. The coordinates of the probes are given relative to the origin, which is located exactly in the middle of the model for the  $y$  and  $z$  coordinate, and in the middle at the top of the inlet for the  $x$  coordinate.

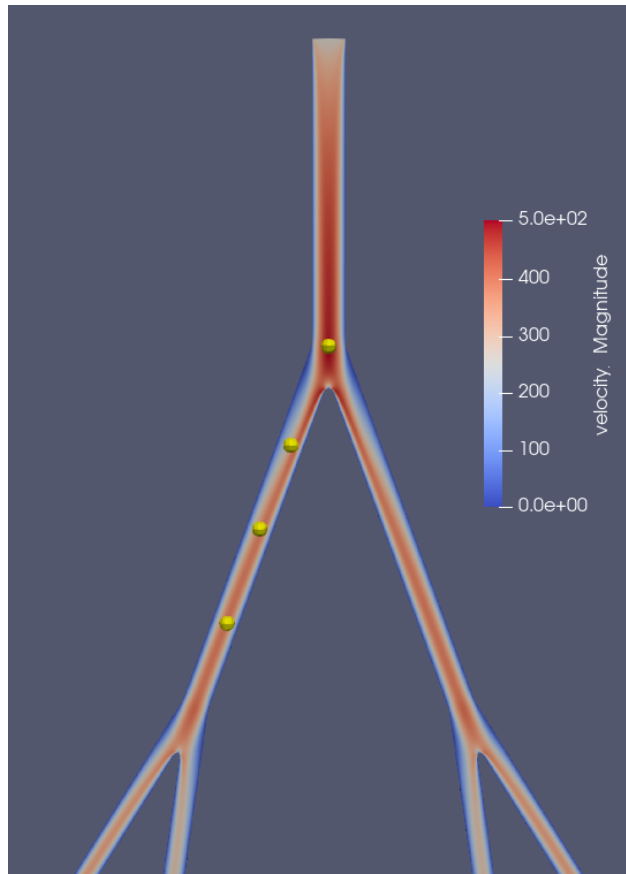


Figure 6.26: Velocity and pressure probe locations in the vasculature model, with the velocity field in  $mm/s$

For the three different grids, the probe velocities at the four different locations are given during the cardiac cycle by figure 6.27.

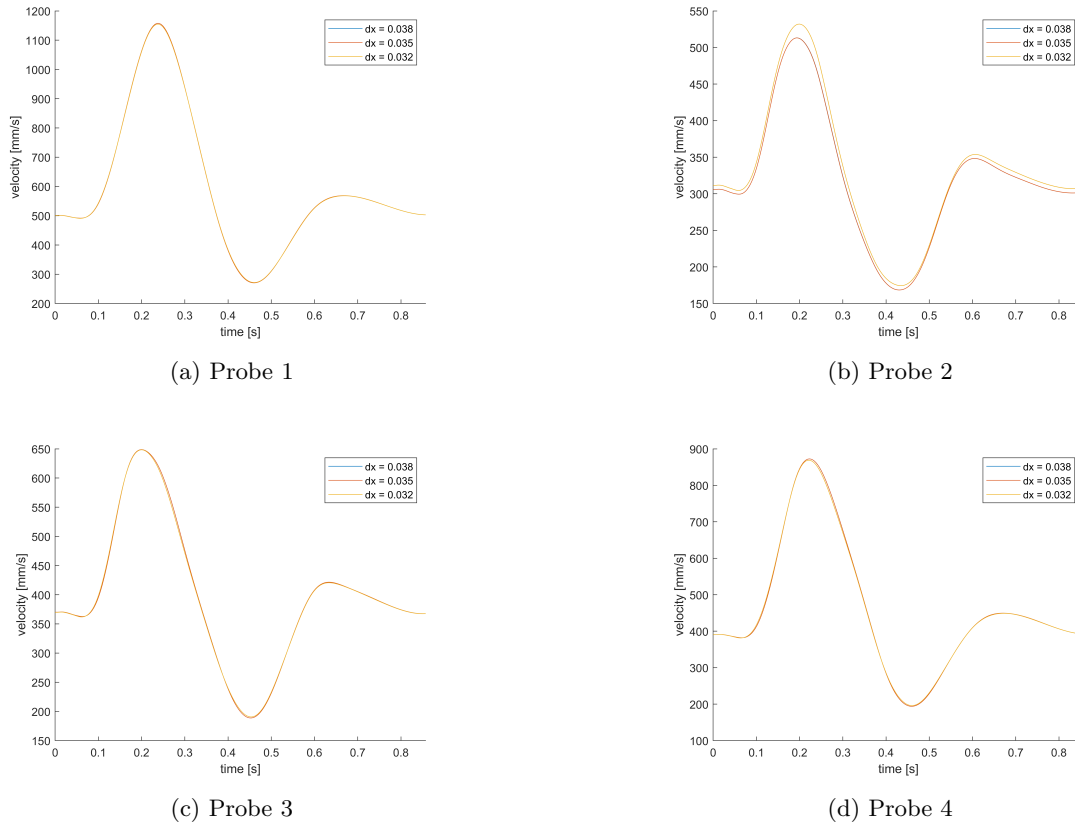
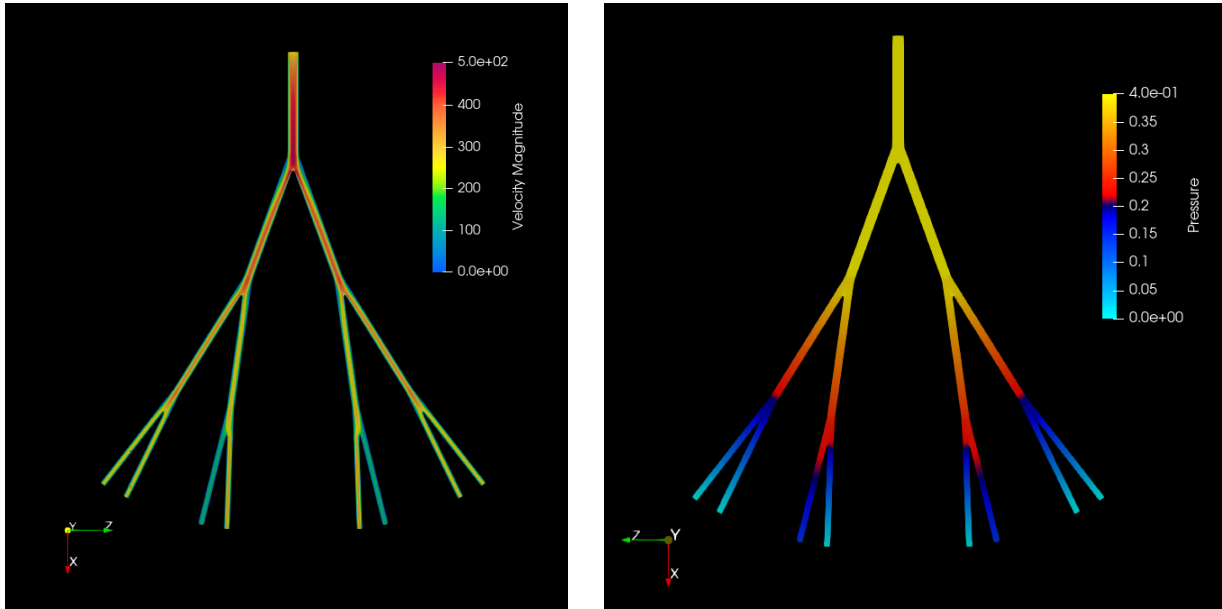


Figure 6.27: Velocity probe values over the cardiac cycle for multiple grids

For probes 1, 3 and 4, the lines are almost on top of each other. Only for probe 2 a difference in probe velocity can be seen for the finest grid. It could be possible that this is a convergence problem, however based on the results from the other probes it is more likely that something went wrong with the tracking at the probe in the simulation with the finest grid. A possible explanation could be that the second probe is located near the edge of the element and that it shifts to another element only for the finest grid. The probe velocity is shifted during the entire cardiac cycle and the tracking of a different element could explain this best.

It seems that the numerical error does not cause the relatively low outflows at outlets 3 and 6. For finer grids, these outflows even become lower instead of higher, so it is not a convergence issue. While in general a finer grid gives a better solution, this is not always the case. From the experiments, which will be compared to the simulations later in this section, this was also not observed, which means that there is still an error in the model that is unresolved. The results of the outflow plot in figure 6.24 can also be seen in the velocity and pressure plots, which means that the tracking errors are now fully resolved. These velocity and pressure plots are given by figure 6.28.

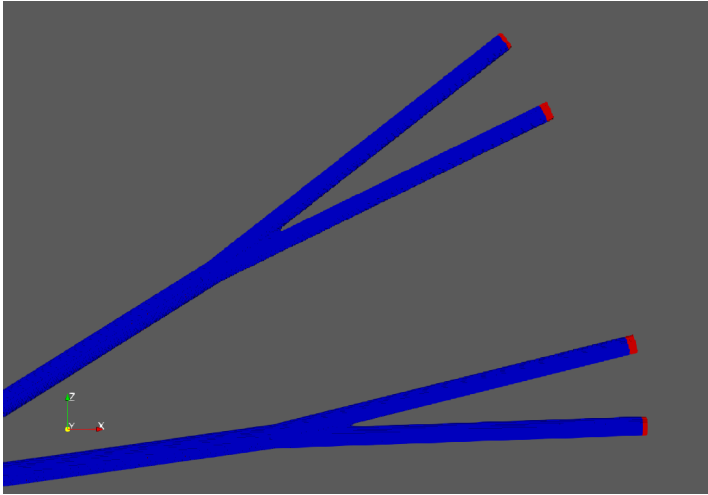


(a) Full scale velocity field in  $mm/s$

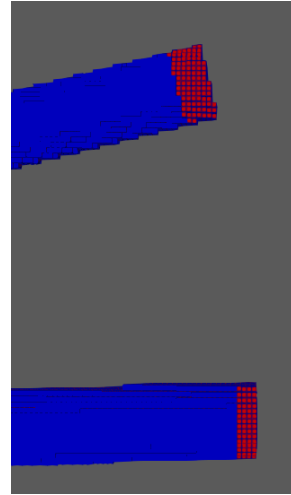
(b) Pressure field with adjusted scale, in  $mPa$

Figure 6.28: Planar scalar fields at the start of the cardiac cycle, inaccurate boundary condition placement

The velocity in figure 6.28a seems to be too low compared to the other outlets, however from the velocity plot alone it is difficult to draw conclusions. The pressure plot gives more information, which contains visibly different pressure gradients near outlets 3 and 6. Also, the pressure at the end of the vasculature is not equal to 0 here. Since a zero-pressure boundary condition is used, a pressure closer to zero would be expected. It turns out that the outflow difference is largely dependent on the pressure boundary condition placement. The placement precision could not be achieved in Seeder, so the model was adjusted again, in which STL files were placed at the end of the outlets. In Musubi, a boundary condition can be placed on an STL object defined by Seeder, so the precision from SolidWorks could be transferred to the simulation. In figure 6.29, a coarsened mesh with  $dx = 0.12$  is used for highlighting the difference between the new and old placement. With the new boundary placement, more elements are added to the model which gives a more accurate representation of the model, where the lengths of the outlets are more equal. Due to the precision of the old placement, more elements are added to some of the outlets, in particular to outlets 3 and 6. Although the difference seems to be small, it does have a large impact on the results. For finer meshes, the difference between the number of layers that are added between the outlets becomes larger, which explains the increasing differences in outflows for the grid refinements.



(a) Old (blue) and new (red) placement

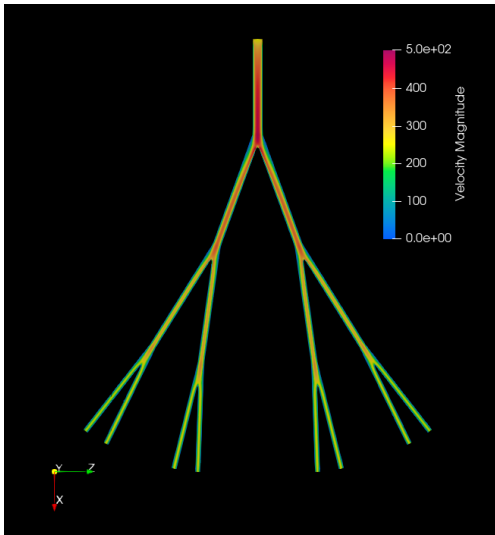


(b) Old and new placement, zoomed

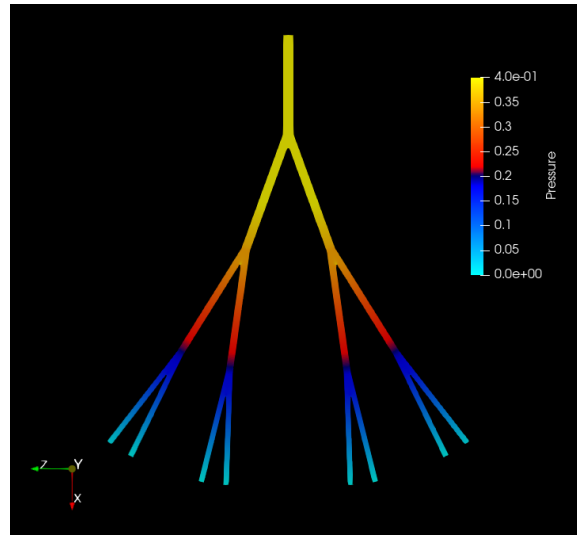
Figure 6.29: Element difference due to the placement of the boundaries

## 6.5 Small angle liver vasculature model, boundary correction

With the changes concerning symmetry and boundary placement, the second model is adjusted and the final model is obtained. The velocity and pressure plots with the improved boundary condition placement are given by figure 6.30. Here, the same element size is used as in figure 6.28 of  $dx = 0.038$ .



(a) Full scale velocity magnitude field in  $mm/s$



(b) Pressure field with adjusted scale in  $mPa$

Figure 6.30: Planar scalar fields at the start of the cardiac cycle, accurate boundary condition placement

Similar velocities and pressure gradients can now be seen in the velocity and pressure fields. The outflow is also much more evenly divided over the outlets, which was also observed in the experiments. Another grid refinement should not be required here, since the placement of the boundary condition will not change the flow too much in general and the geometry remains the same. Because of a limited computational capacity, the

coarsest grid in table 6.8 will be used for the remainder of the simulations, which should give accurate enough results based on the probe convergence study. The comparison to the experiments can be seen in figures 6.31 and 6.32. The simulation results are based on one cycle, while the experimental results are obtained from running multiple cycles through the phantom. The results are compared by using the percentual outflows, which should be equal for one and multiple cycles based on the type of flow in the model.

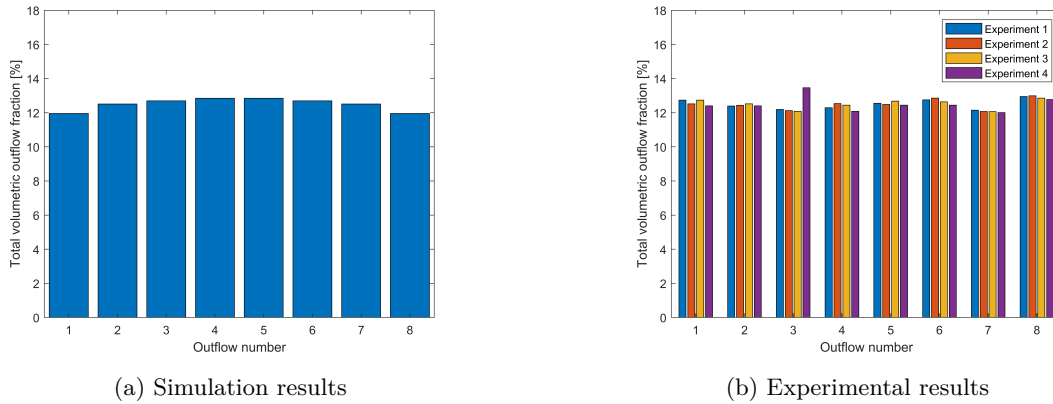


Figure 6.31: Comparison of fractional outflows from the simulations and experiments

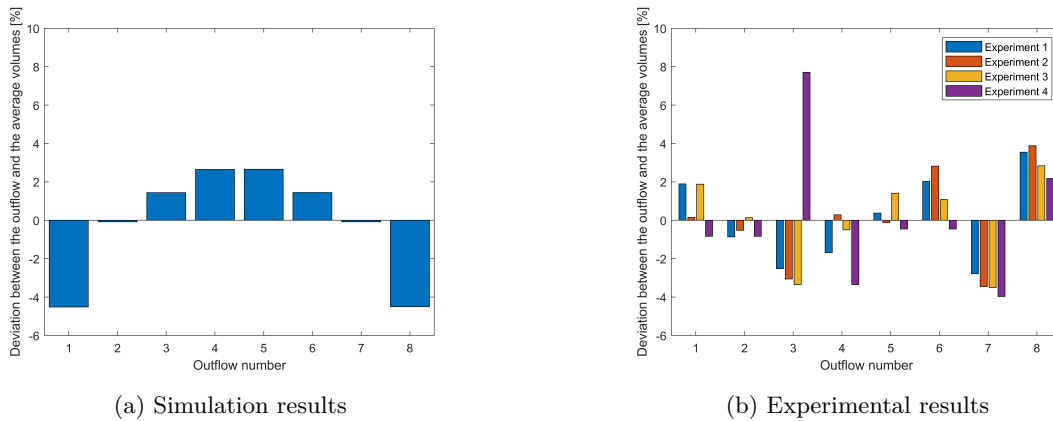
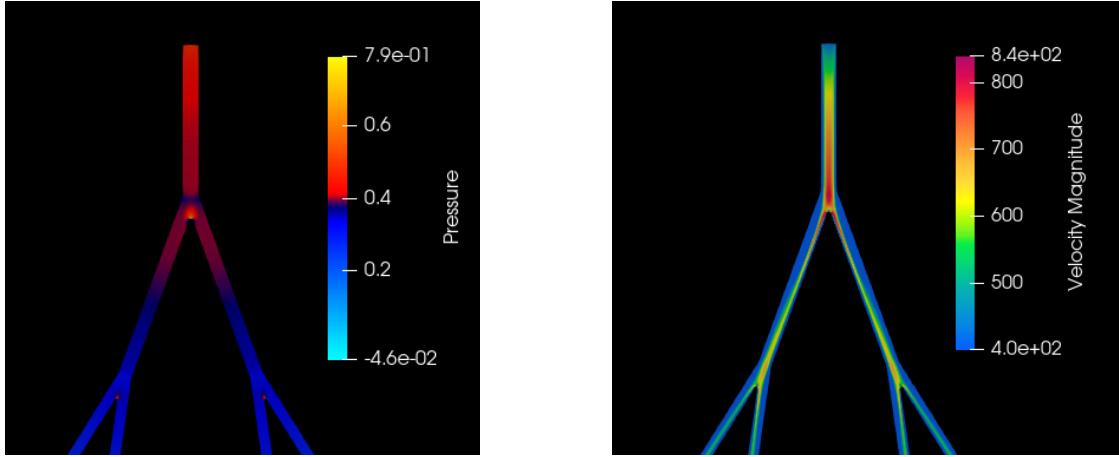


Figure 6.32: Comparison of outflow deviations from average outflow from the simulations and experiments

In the simulations, there is a minor trend visible in figure 6.31a. From the results it can be seen that the central outlets have a slightly higher outflow than the more peripheral outlets. It could be possible that the boundary placement still causes this difference and that another boundary condition for the pressure could reduce this difference. The difference between the volumetric rates between the simulations and experiments is within 5%.

This difference is comparable to the found deviations in the experiments. Here, even outflow should be observed in the symmetric outlets and an error can be defined based on this. For example, the flow rate difference is about 4% between outlets 3 and 6 for all conducted experiments, which can still be considered a relatively small error. The errors in the experiments become more apparent when looking at the outflow deviation plots in figure 6.32. Here, a symmetric profile like the simulations show in figure 6.32a is expected. Again in outlets 3 and 6, a large difference is clearly visible, but the total error is limited to a few percent. Although some differences between the experiments and simulations can be seen, quite an even flow distribution over the outlets is obtained in both the simulations and the experiments and it can be assumed that they match well enough for the purpose of the simulations.

From the simulations, it can be concluded that there is no turbulence and no backflow happening in the model at any time in the cardiac cycle. The most extreme flow with the largest velocity can be found near the first bifurcation. As the flow nears the bifurcation, the pressure increases and the flow is directed into one of the branches. This increase in pressure can be seen in figure 6.33a for the deceleration phase. The velocity field of the deceleration phase be seen in figure 6.33b. Here, the scale is set so velocities below 400  $mm/s$  are not in the figure, to visualise the high velocity regions.



(a) Pressure field in  $mPa$ , adjusted scale

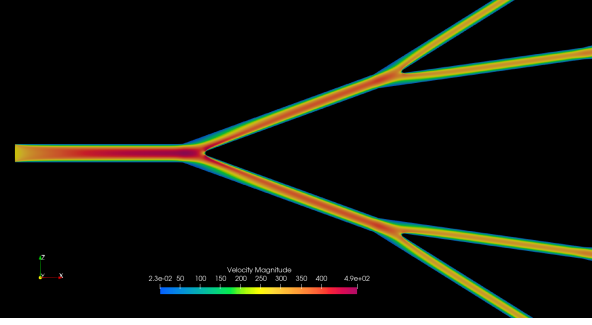
(b) Velocity magnitude field in  $mm/s$ , adjusted scale

Figure 6.33: Planar scalar fields during deceleration of the cardiac cycle

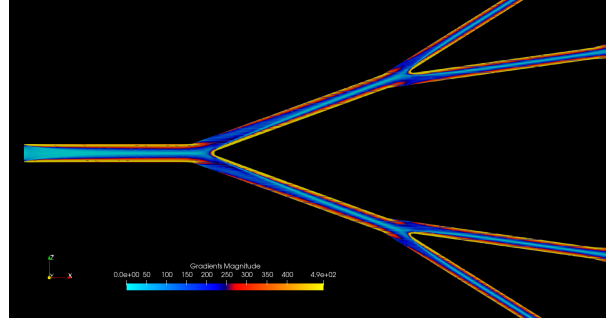
The velocity magnitude fields at all 6 time instances given in figure 6.4 can be found in Appendix B. The shape of the velocity field changes slightly over the cardiac cycle, mostly around the first bifurcation of the vasculature. This is best displayed by showing the gradient field of the velocity field. The gradient matrix is calculated by using equation 6.3:

$$G_{ij} = \nabla v_i = \frac{\partial v_i}{\partial x_j} \quad (6.3)$$

In the equation,  $v_i$  accounts for the velocity in three directions and  $x_j$  accounts for the three spatial directions, with  $i, j \in \{1, 2, 3\}$ . The full gradient matrix  $G_{ij}$  for a 3D vector field contains 9 components, where the magnitude of the matrix is also computed. The magnitudes of the velocity field and the gradient field are given in the figures 6.34 and 6.35 for the start of the cycle and during deceleration of the cycle. Since larger gradients are found for increased values of the velocity, the gradient field range is scaled with the velocity to highlight the changes in the velocity field form during the cycle.

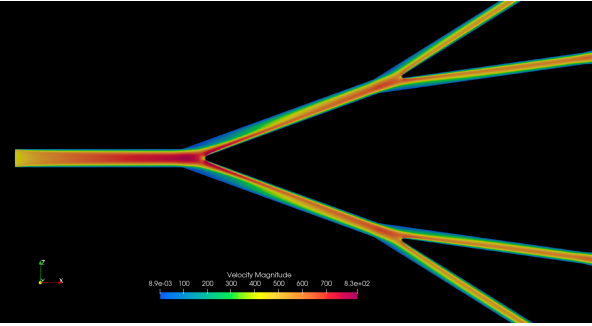


(a) Velocity magnitude field in  $mm/s$

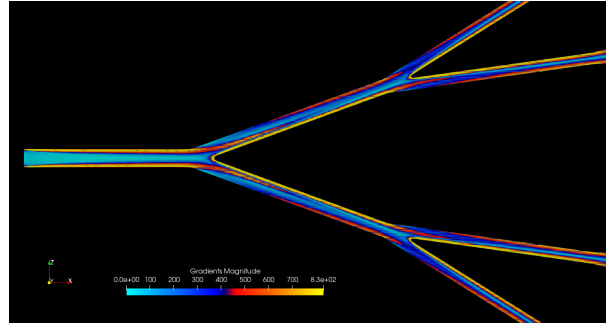


(b) Gradient magnitude field in  $1/s$

Figure 6.34: Magnitude planar fields at the start of the cardiac cycle



(a) Velocity magnitude field in  $mm/s$



(b) Gradient magnitude field in  $1/s$

Figure 6.35: Magnitude planar fields during deceleration of the cardiac cycle

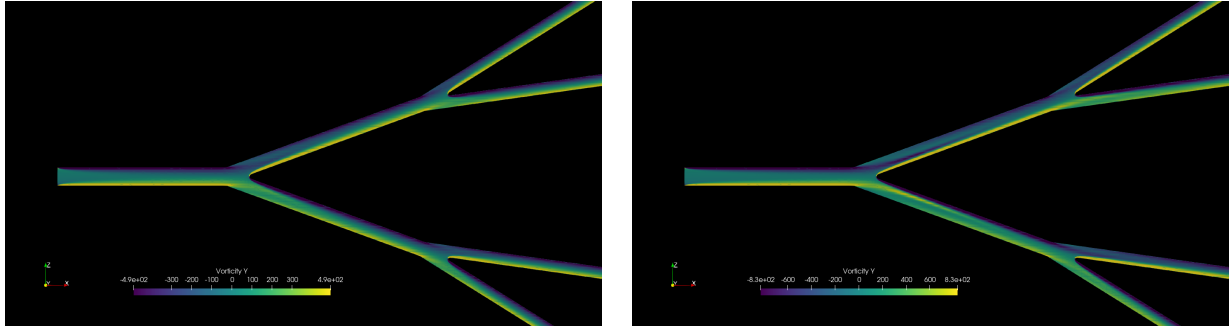
The unit of the velocity magnitude is  $mm/s$  and the unit of the gradient magnitude is  $1/s$ . It can be seen that the gradient field changes mostly around the first bifurcation, but also slightly around the second bifurcation during the cardiac cycle. Only the plots for the start of the cycle and the deceleration of the cycle are given, because from further analysis it is concluded that these plots also represent the shape of the field for the other time instances. For example, during acceleration the gradient field transforms from the start to the deceleration gradient field. At peak systole, the gradient field has the same shape as the deceleration gradient field. Interesting here is that the gradient field during deceleration with a certain velocity has a different shape than the gradient field during acceleration with the same velocity, which means that next to the magnitude of the velocity, the acceleration of the flow also has an effect on the shape of the field. The gradient fields for the other time instances can be found in Appendix B.

The change in the gradient field shows that the cardiac cycle time instance can have a large impact on the particle distribution in the vasculature. For a large change in the velocity field shape, the streamlines change over the cardiac cycle and the injection time and instance during the cycle become important parameters for a good particle distribution. With a known velocity field, streamlines can be calculated for the cardiac cycle. Based on the differences in the gradient fields during the cardiac cycle, differences in the streamlines can already be expected.

Streamlines are always tangent to the direction of the flow and if the direction of the flow changes, the streamlines change. The flow directions changes are governed by the rotation of the flow, which is related to the vorticity or curl of the flow. The vorticity of the velocity field can be calculated by using equation 6.4.

$$\omega_i = \nabla \times v_i \quad (6.4)$$

The result is a vector with three components, since for a 3D field  $i \in \{1, 2, 3\}$ . The magnitude of this vector gives the degree of rotation, but does not give information about the direction. The three components give the curl of the flow around the three axes. To understand the meaning of the vorticity, the right hand rule can be used. In figure 6.36, the vorticity field around the  $y$ -axis is given. For these plots, the right hand rule shows that a positive value gives a counter-clockwise rotation and a negative value gives a clockwise rotation. The unit of vorticity in this case is  $mrad/s$ . Again, the start and deceleration phase are given in the plots.



(a) Start of the cardiac cycle

(b) Deceleration during the cardiac cycle

Figure 6.36: Vorticity of the velocity field around the  $y$ -axis

The vorticity is scaled with the velocity, because a higher value is obtained if the velocity is the same for a similar flow field. From the gradient field plots differences in the vorticity are expected and these differences can be observed around the first bifurcation, however the differences are not apparent. Still, after inspection it can be seen that the vorticity is lower at the start of the cardiac cycle and a relatively smoother vorticity field is also observed around the bifurcation. From this, differences in the streamlines are expected, however the severity is still to be determined. Also, the acceleration seems to have a negligible impact on the form of the vorticity field. The plots for the other time instances can be found in Appendix B.

The streamlines are calculated using a Runge-Kutta 4-5 integration scheme on a constant velocity field at one time instance. The streamlines are coloured based on the outlet they eventually flow to. The streamlines are calculated from the outlets back to the inlet, where a sufficient amount of points are placed at the outlet to generate distinct regions. In figure 6.37 the streamlines with the colours based on their corresponding outlet are given. Here,  $z$  is the vertical axis and  $x$  is the horizontal axis.

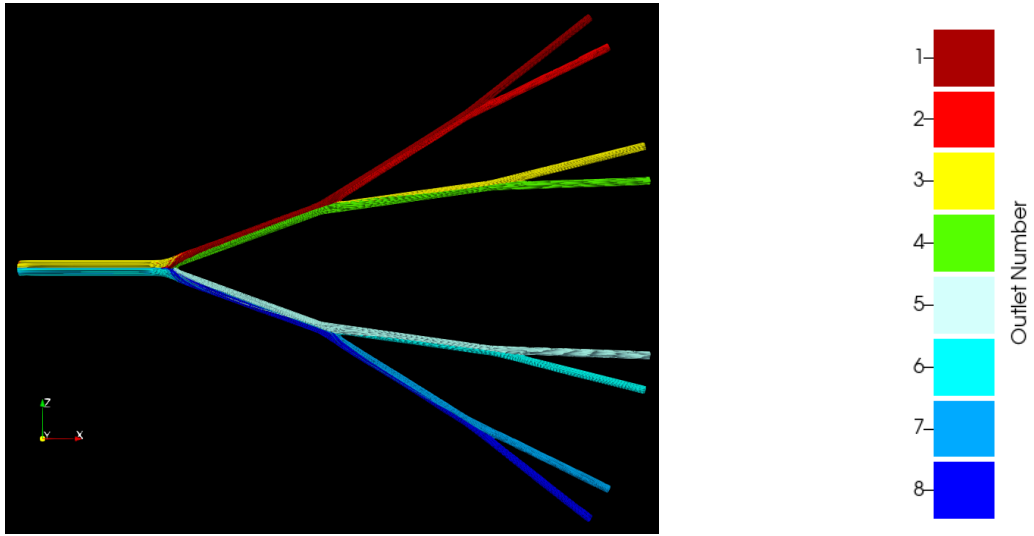


Figure 6.37: Streamlines in the vasculature model during deceleration, col-  
 Figure 6.38: Colourmap based on the outlets

Now, cross sections are made near the inlet to show the streamline distribution maps. The distributions at the inlet for the 6 time instances that are given by figure 6.4 are displayed in the plots in figure 6.39. Here the  $y$ - $z$  plane is given with  $z$  as the vertical axis.

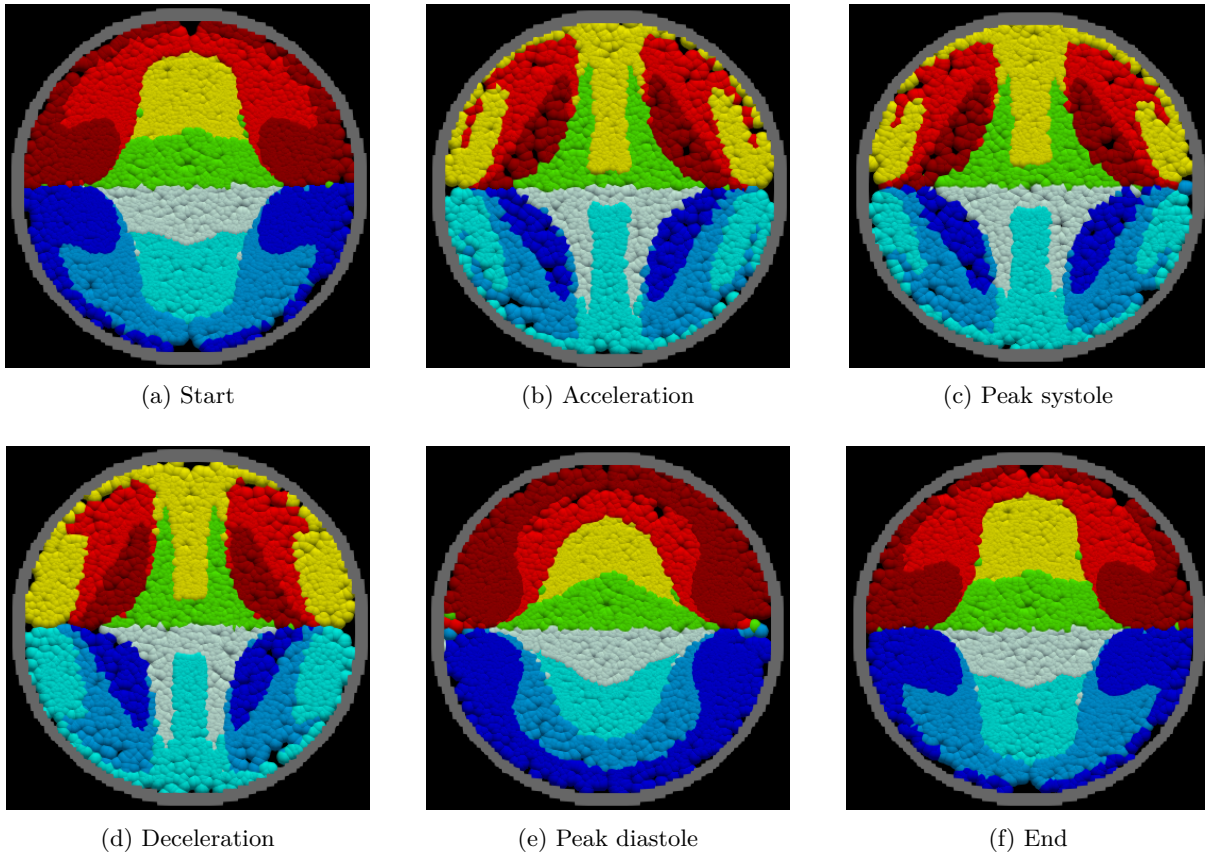


Figure 6.39: Streamline distribution at the inlet at various instances

In the streamline distribution maps, clear regions can be distinguished based on the outlet where the streamlines end up. This also means that the used Runge-Kutta integration scheme is very accurate: intersection of the streamlines is not constrained and calculation is done from the outlets to the inlet, where the largest error will consequently be found at the inlet. With a lower accuracy, a mix of the regions is expected and symmetry in both the vertical and horizontal plane would likely not be observed.

The obtained maps give a lot of information about particle distributions under some circumstances. If the streamlines remain constant sufficiently long, then a weightless particle that is released at the inlet at one of the regions in the map will flow to the corresponding outlet. From these maps, the start and end map are similar, which is expected since the velocities are similar and there are no residual flow effects due to the cardiac cycle in the model at the end of the cycle, which is largely due to the laminar flow. Also, the streamline maps from acceleration, peak systole and deceleration are quite similar. From this, it can be concluded that the velocity magnitude has the biggest influence on the streamlines and not the acceleration or deceleration of the flow. This observation is further substantiated by the peak diastole map, which is clearly different from the start and peak systole maps, with the only difference being the velocity magnitude.

The calculated streamline distribution map for the velocity at the start of the cycle can also be compared and verified to a steady state simulation in which particles are released. For such a simulation, particle trajectories should be similar to the streamlines if the particles are passive enough and if the inlet velocities are similar. At Ghent University, Ansys Fluent simulations have been conducted by T. Bomberna and N. Saikali on the same model. Particle Release Maps (PRMs) were calculated for different types of particles for both steady and transient flow. The steady state microbubble PRM from these simulations is given by figure 6.40a, where the inlet velocity of this simulation is the same as the velocity at the start of the cardiac cycle that is used in this chapter. Next to this figure, the streamline distribution map at this time instance in the cycle is given again, with an adjusted colour legend for comparison. Further comparison to the Ansys Fluent simulations can be found in Appendix C

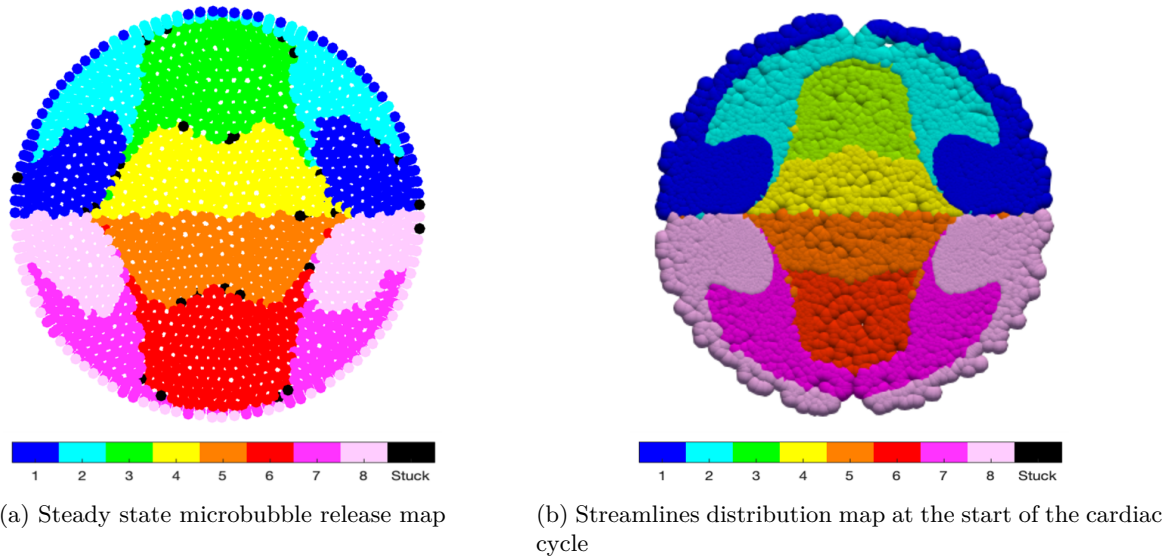


Figure 6.40: Comparison of the particle release map and the streamline distribution map for similar velocities

Microbubbles are very small particles that are often used as contrast agents in medical imaging. It is expected that the particles are sufficiently small and light, such that they will follow the streamlines of the flow quite well. In the simulation, particles are released at the inlet and tracked throughout the vasculature model. Based on the outlet they flow to, a colour is assigned to the microbubble. If they follow the streamlines, then the coloured cross-section of the streamlines at the start of the cardiac cycle should correspond to the PRM of the microbubbles. The comparison in figure 6.40 between the microbubble PRM and streamline

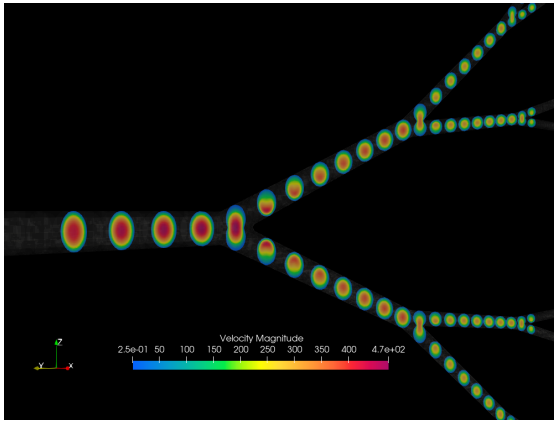
distribution can be considered quite good, as the outlet streaming regions can be found in the same locations and their shapes are similar. Some differences in the plots can be explained by the thickness of the points in the streamline distribution plot, which is used for visualization and gives an apparent larger thickness of the outer layer. Moreover, the microbubbles are not entirely passive and thus some differences are expected between the microbubble paths and the paths that passive tracers would follow. Still, the results can be considered quite good and the microbubble distribution can be predicted by looking at the streamlines for this case.

Based on this comparison, the conclusion can be expanded for transient flow behaviour. If the streamlines are more or less constant over a sufficient period of time such that the particles can reach the outlets, then the streamlines and the trajectories of the weightless and near-weightless particles should be quite similar. From the acquired maps, it can be stated that the velocity is especially important for the distributions. Also, for higher velocities the streamlines have to remain constant for a shorter amount of time, because particles reach the outlets faster in this case.

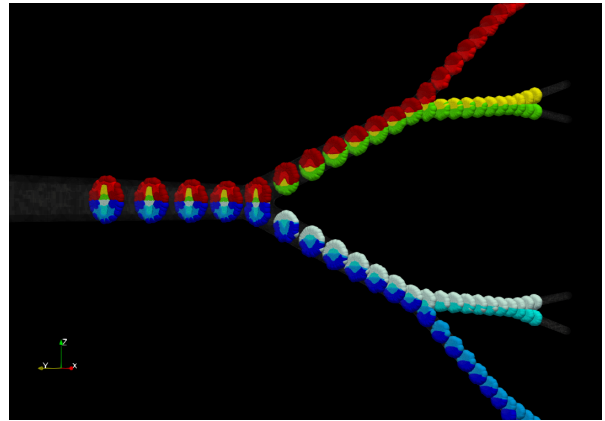
The particle time to reach the outlets versus the plane injection location should be studied for more information about the best injection location and time, however the calculated streamline plots already give an implication. For example, if particles should be directed to the more peripheral outlets, it seems that the best injection time is around peak diastole or around the start of the cardiac cycle. If the model is placed horizontally, the injection location should be as close as possible to the right or left side of the wall. For outlets 2 and 7, the best injection time would be around the start of cardiac cycle, near the top or the bottom of the outlet depending on the desired outlet.

One of the limitations here is the catheter precision, which is used for the injection of the particles in the blood stream. For this reason, only general conclusions can be drawn from the given plots, given that the velocity is the most important parameter for the distribution plot shape. During the diastolic phase, the velocities are in between the start/end of the cycle velocity and the peak diastolic phase velocity, which means that during this phase the distribution maps look similar to the found distribution maps for these three phases. For the outermost 4 outlets, distributions seem to be better during the diastolic phase, with injection preferably a bit closer to the wall. For the innermost 4 outlets, distributions seem to be better during the systolic phase. These conclusions are based on the sizes and locations of the found shapes.

The obtained results apply only for the simplified model with weightless particles, however it could already give an implication for any model based on the flow behaviour. During the cardiac cycle, streamlines change due to the increase and decrease in velocity for this model. From previous analysis it was seen that the vorticity field also changes with the velocity, so it implies that the vorticity and streamline development can be linked. The complete flow and streamline development is difficult to visualise using the previously used cross-section of the model, so a new approach will be used for this analysis. In figures 6.41 to 6.43, the development of the streamlines over the vasculature is given using several slices for three time instances. The velocity field developments are also given. The start, deceleration and peak diastole time instances account for the calculated streamline distribution maps at all the 6 important time instances.

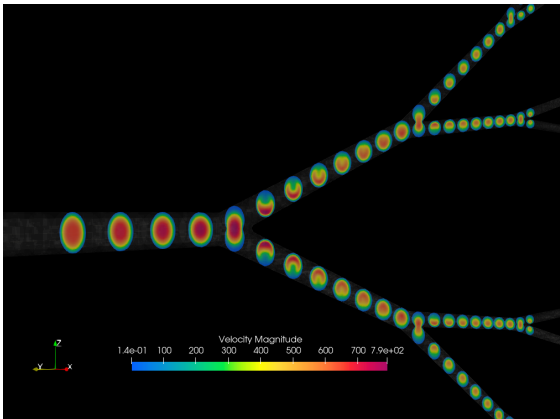


(a) Cross sections of the velocity field magnitude in  $mm/s$

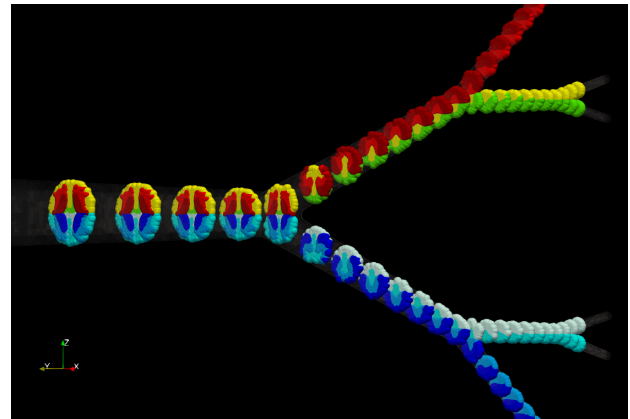


(b) Cross sections of the streamlines

Figure 6.41: Slices at the start of the cardiac cycle, with a slice interval of  $5mm$

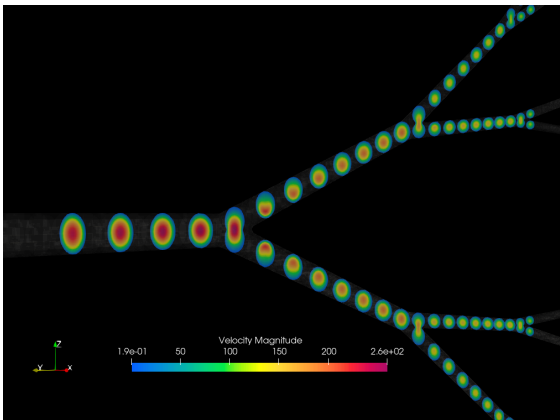


(a) Cross sections of the velocity field magnitude in  $mm/s$

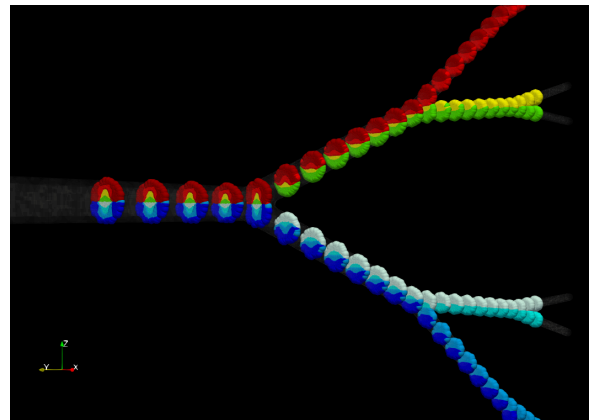


(b) Cross sections of the streamlines

Figure 6.42: Slices in the deceleration phase of the cardiac cycle, with a slice interval of  $5mm$



(a) Cross sections of the velocity field magnitude in  $mm/s$

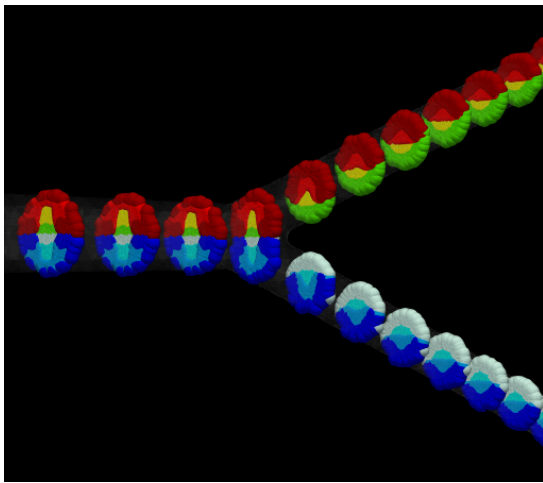


(b) Cross sections of the streamlines

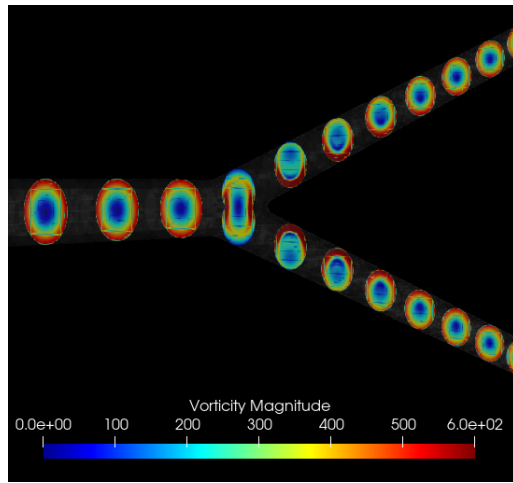
Figure 6.43: Slices at peak diastole of the cardiac cycle, with a slice interval of  $5mm$

From these plots, it is clear that the streamline development is quite different between the phases, especially during the deceleration phase. In the deceleration velocity plot, a v-shape velocity profile is observed, which is also slightly visible in the start of the cycle velocity plot. This flow velocity difference could explain the change in streamlines. In the deceleration phase, flow in this region is pushed upwards, causing the flow above to be pushed towards the lower velocity region in the middle, which can be seen for the yellow streamlines. Another relevant difference here is the development length to Poiseuille flow in the vessels after the bifurcation, which is much longer for the deceleration phase. When zooming in on the streamline development plots, it can also be seen that in the deceleration phase the streamline cross-sections are still changing further downstream relative to streamline plots of the other phases.

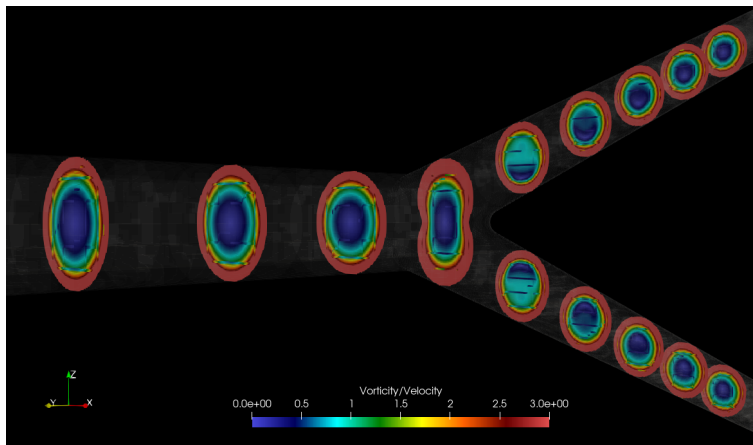
It is however difficult to draw conclusions on streamline development. The velocity field and streamline development plots are different, however the link between the differences is not clear from these plots. The vorticity plots of these three time instances should offer more information, as the change of the streamlines is governed by the vorticity. In figures 6.41 to 6.43, it can be seen that the largest changes occur around the first bifurcation, so in the next part of the analysis a closer at this area is taken. In figure 6.44, slices around the first bifurcation are given for the streamlines, velocity, vorticity and a newly defined variable that is the vorticity scaled by the velocity per point.



(a) Cross sections of the streamlines



(b) Cross sections of the vorticity magnitude field in  $mrad/s$

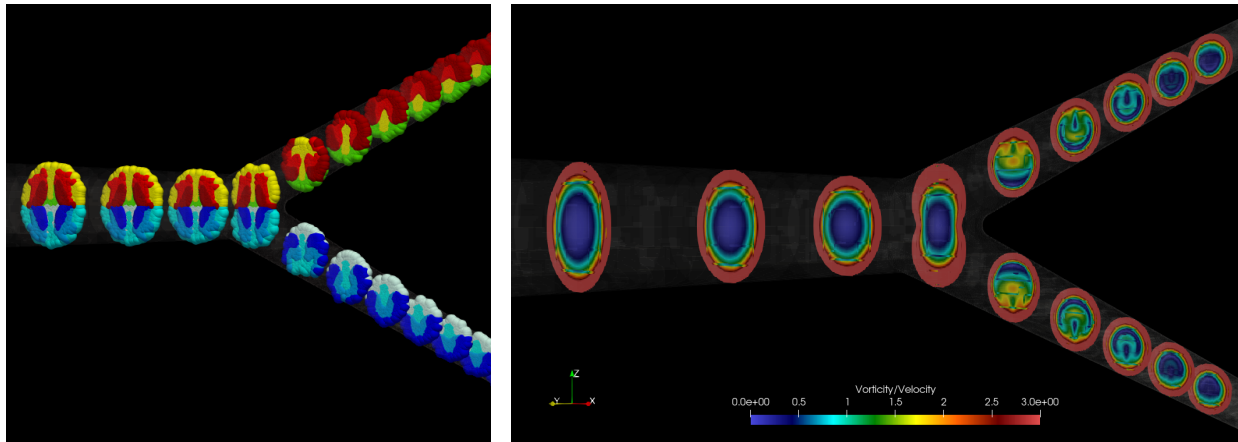


(c) Point scaled vorticity field by velocity magnitude ( $mm/s$ ) in  $mrad/mm$

Figure 6.44: Slices at the start of the cardiac cycle zoomed on the first bifurcation, with a slice interval of  $5mm$

In figure 6.44 the vorticity magnitude plot is given next to the streamline slices plot. It can be seen that the vorticity changes around the bifurcation, which can be linked to the changes in the streamlines. Still, this can only be seen from the vorticity slice changes relative to the vorticity at the start of the inlet, given by the first slice in the plot. While the streamline changes are influenced by the vorticity, the magnitude of the vorticity alone does not give enough information about the change. If the vorticity is similar over a whole region in a cross-section, then a region with a higher velocity is affected less by the vorticity due to the shorter period of time the fluid is in this region. The unit of the vorticity is in rotation per second, while for the streamline development it would be more interesting to see the rotation per unit of length. The vorticity magnitude is divided by the velocity magnitude at each point, which gives a vorticity like parameter with the unit  $mrad/mm$ . The result is given in figure 6.44c.

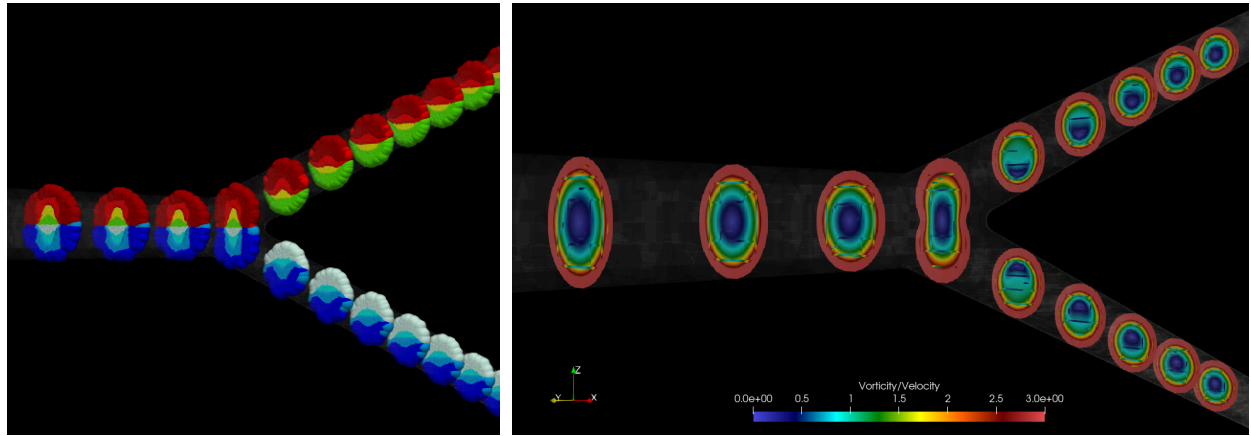
For the flow in the middle of the channel, it can be seen that the region of the higher adjusted vorticity coincides with the region in the streamline development plot where the streamlines are changing. For the flow at the sides of the channel, very high values of the vorticity are found which do not result in streamline changes. This wall-induced vorticity is an effect of the used no-slip boundary condition. This vorticity does however not result in flow rotation, which can be explained by imagining a particle near the wall of the vasculature. This particle will rotate due to the velocity gradient near the wall, even though the streamlines are parallel to the wall and do not experience rotation at all. The vorticity can be seen as a microscopic rotation of the fluid, which can result into macroscopic rotation if the flow has inertia. Near the walls, the flow inertia is very low, which does not result into flow rotation even though the vorticity can be very high here. The point velocity scaled vorticity can thus only give information about the flow rotation in the middle of the channel.



(a) Cross sections of the streamlines

(b) Point scaled vorticity field by velocity magnitude ( $mm/s$ ) in  $mrad/mm$

Figure 6.45: Slices during the deceleration phase of the cardiac cycle zoomed on the first bifurcation, with a slice interval of  $5mm$



(a) Cross sections of the streamlines (b) Point scaled vorticity field by velocity magnitude ( $mm/s$ ) in  $mrad/mm$

Figure 6.46: Slices at peak diastolic in the cardiac cycle zoomed on the first bifurcation, with a slice interval of  $5mm$

In figures 6.45 and 6.46 streamline and adjusted vorticity slices of the deceleration and peak diastolic phase are given. Again, the streamline changes coincide with the adjusted vorticity plots. Also, the changes in streamline direction in the deceleration phase are larger than at peak diastolic in the cardiac cycle, which can be seen in the adjusted vorticity plots by the larger values in the middle of the vessels. The direction of the vorticity is not given, however this can in turn be derived from the streamline plots.

In the deceleration phase plot, the region after the bifurcation on the outside of the model has a relatively high vorticity compared to the velocity. This region coincides with the yellow streamlines just after the bifurcation. In the plots, it looks almost like the red and dark red streamlines wrap around the yellow streamlines. Due to the high vorticity, the yellow streamlines disappear from this region after one slice already. Some more flow development happens after this until the known Poiseuille flow profile can be seen again, in which the streamlines become steady. The development to Poiseuille flow in the deceleration phase was already given by figure 6.42a.

The regions of interest are highlighted for further analysis from a particle dynamics perspective. Particle path deviations from the streamlines will be investigated in the future. The results in this chapter can be used for this and possible deviations are likely to take place in the highlighted regions. Also, the results can be used as a validation baseline for the activity of the particles. Similar results should be obtained for passive particles that are actually tracked in the flow by Musubi, while a difference in distribution will give a measure of the influence of the activity of the particles. The administration of the particles is done by a catheter, which will also have an influence on the flow. In the next chapter, the qualitative study on the catheter effect on the flow and a possible impact on the found flow characteristics in this chapter will be discussed.

# Chapter 7

## Catheter injection: a qualitative study

In the previous chapter the simplified RHA model was analysed, which offers more insight into the particle distributions. In SIRT, particles are administered into the blood flow by catheter injection. While the selective therapy offers some advantages with respect to ablative techniques like chemotherapy, catheter injection also has its own limitations. One important limitation for this technique is the catheter reach: the vasculature becomes smaller after bifurcations and eventually the vessels become too narrow for the catheter. To ensure a good distribution, which in practice means that most particles will be delivered to vessels near the tumour, a good understanding of the flow is required. In the previous chapter, the general flow in the simplified model was studied with an initial prediction of particle delivery regarding injection time and the planar particle release location. In the obtained streamline maps in figure 6.39, the influence of the catheter was initially neglected and the validity of the assumption has to be investigated. The goal of this study is to obtain more insight into the disturbance of the flow due to catheter injection. Therefore, the influence of the catheter flow on the vasculature flow will be investigated. In the analysis, the influence of the blood flow on the obtained flow fields will also be discussed to estimate the total impact that catheter injection could have. In this chapter, the blood flow will be referred to as external flow. With the results in this section, only a prediction of the results can be made and the influence of the blood flow can only be estimated. It is therefore a purely qualitative study which could be used as the groundwork for further research into catheter injection parameters.

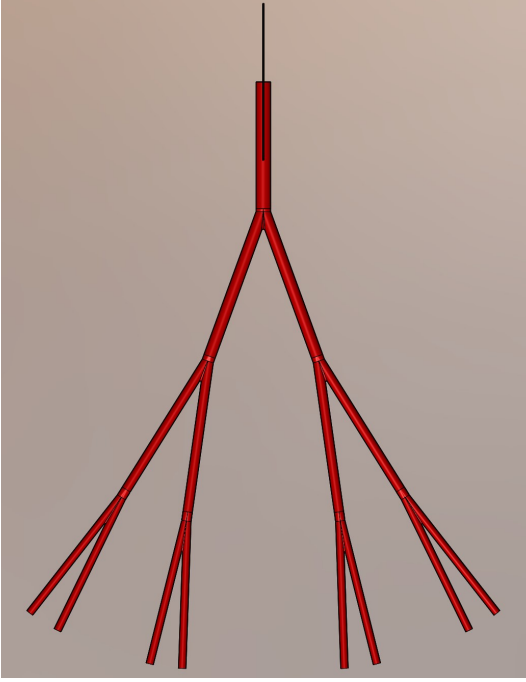
### 7.1 Catheter specifications and modelling

In this study a rigid catheter is placed in the vasculature, from which a flow is injected into a stationary fluid in the model. The catheter dimensions are based on the Progreat® microcatheter from Terumo [79]. The specification are given by figure 7.1.

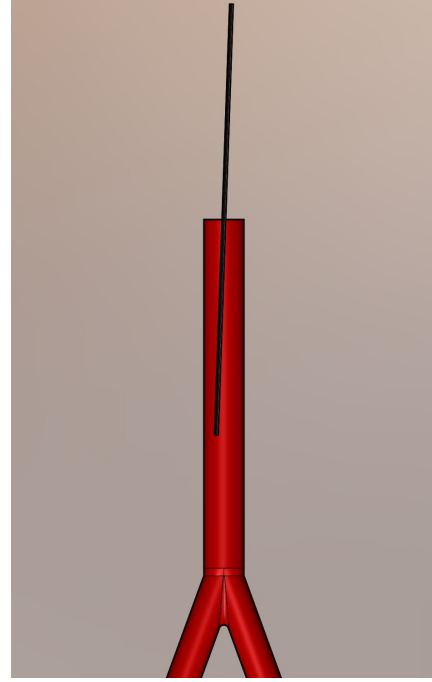
The model of the catheter can be found in figure 7.2. Here, the full model is given by figure 7.2a without a catheter angle and a zoom of the model is given by figure 7.2b for the model with a catheter angle of  $2^\circ$ . The simplest type of catheter is used for this study, while new and complex catheters are designed and show a real influence on distribution results [5]. In the simulations the catheter remains in the same place, but it should be noted that in the in-vitro experiments with a catheter injection performed at the University of Twente, large fluctuations in catheter position were visible during the injection. How large these fluctuations can be in practice and to what extent these fluctuations could influence the distribution results is not quantified and might be interesting for future research on catheter modelling in CFD.



Figure 7.1: Progreat® microcatheter 0.025" (0.65 mm) label



(a) Full catheter model, case 1: no catheter angle and inserted at the centre



(b) Full catheter model, case 2: tilted catheter, inserted at the centre

Figure 7.2: Cross-section of the catheter model for two different setups

In this chapter, the length of the catheter is also adjusted for the model, which should be clear from the corresponding velocity and vorticity plots. The information on the different catheter placement cases is given by table 7.1. The other parameters of the model are the same as in the previous model, with the dimension given in table 6.7.

Case	Length [mm]	Angle	Wall Thickness [mm]	Diameter (excl. wall thickness) [mm]
1	20	0	0.1	0.65
2	20	2	0.1	0.65
3	32	0	0.1	0.65
4	32	2	0.1	0.65

Table 7.1: Catheter cases and dimensions

In the table, the catheter length is the length of the catheter inside the model. The length to the bifurcation from the inlet is 37.6 mm. The wall thickness is the thickness of the catheter wall. First, a wall thickness of 0.01 mm was used, however this resulted in leaking of the catheter, which can be found in figure D.1 in Appendix D. For such a simulation to work, the element size should at least be of the same order, preferably smaller, which would result in the use of many elements if the uniform structured grid is used. For the new simulations a thickness of 0.1 mm is used. This thickness is also more realistic when looking at existing catheters, with wall thicknesses of new catheter being pushed to just below 0.1 mm [80]. The catheter diameter that is given in the table is excluding the wall thickness.

## 7.2 Catheter injection simulation results

Now the model is described, the results from the simulations can be discussed. From these simulations, only a prediction of the influence can be made. The performed analysis is based on steady state simulations, with the velocity boundary condition placed on the inlet of the catheter. The vasculature inlet is now closed and treated as a wall. The velocity is equal to the velocity at the start of the cardiac cycle in the previous section, given in table 7.2 with the other simulation parameters. The parameters are the same as in the previous section. The choice for the velocity is made such that a similar grid size can be used as in the previous section, where higher velocities could exceed the lattice velocity limit.

Parameter	Value
$\rho$	$1.1474 \cdot 10^{-6} [kg/mm^3]$
$\mu$	$4.3100 \cdot 10^{-6} [kg/(mm \cdot s)]$
$\omega$	1.9 [-]
$v$	255.0 [mm/s]

Table 7.2: Simulation parameters

case	$dx [mm]$	$dt [s]$	N
1	0.038	$3.46 \cdot 10^{-6}$	$41.1 \cdot 10^6$
2	0.035	$2.94 \cdot 10^{-6}$	$52.7 \cdot 10^6$
3	0.032	$2.45 \cdot 10^{-6}$	$69.0 \cdot 10^6$

Table 7.3: Simulation details

For catheter case 1, the convergence was analysed using several probes given in figure 7.3a. The probes are placed at the same locations as the previous model, with the dimensions given by table 6.9 in the previous chapter. Here the probes number is increasing from the outlet, which means that probe 1 is located in the middle of the model just before the bifurcation. The three different grids are also similar to the grids that were used in the previous section, which are given in table 7.3.

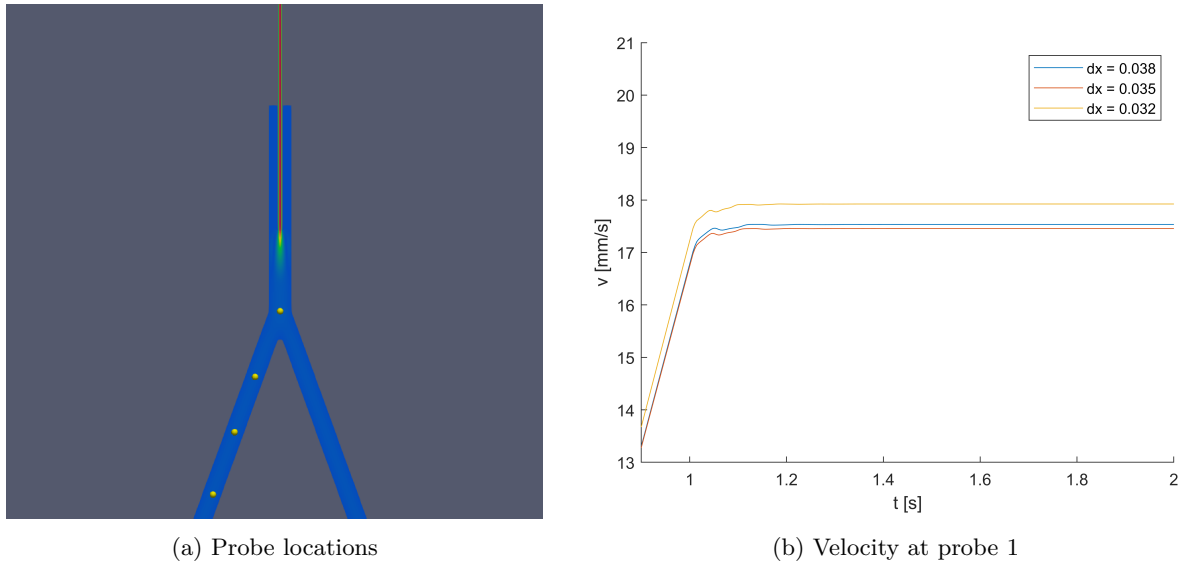


Figure 7.3: Convergence study using probes

Looking at the probe locations in figure 7.3a, one could argue that the placement could be better for checking the convergence. The region of interest is around the catheter and the biggest velocity and flow differences are expected in that region. Of all the probes, probe 1 is located the closest to the catheter and it is assumed that this probe can give information about the consistency in this region. Still, the rest of the field should also be consistent for different grids, so all the results are expected to give enough information about convergence. Only the probe values for the first probe are given, because similar results are obtained for the other probes. The other probe plots can be found in Appendix D.

In figure 7.3b, it can be seen that the finest grid probe values are slightly higher than the probe values for the two coarser grids. The difference between the finest and coarsest grid is about 3%, which is acceptable. Also, since this is a qualitative study, it is important that the flow behaviour is captured by the simulation. It can be assumed that this probe velocity difference will not result in major flow differences. The results in the plots below are all obtained using the coarsest grid in table 7.3.

First, case 1 is analysed. Here, the catheter is located a bit further from the bifurcation and it is placed horizontally in the vasculature model, so without an angle. The velocity and vorticity plots can be found in figure 7.4a. For all the four cases, four 2D plots are given to visualise the results. First, the velocity plot is given at full scale and at an adjusted scale to visualise the locations that are impacted by the catheter injection. The velocity magnitude plots are given, but also the velocity in  $x$  direction, which gives information about the backflow. From the velocity, the vorticity can be calculated. Here, the  $y$  component of the vorticity is given, which gives the 2D curl of the velocity field. In the previous chapter, high velocity and vorticity were linked with a change in streamlines. From the results below, regions with high values for both these quantities could result in changes in the flow.

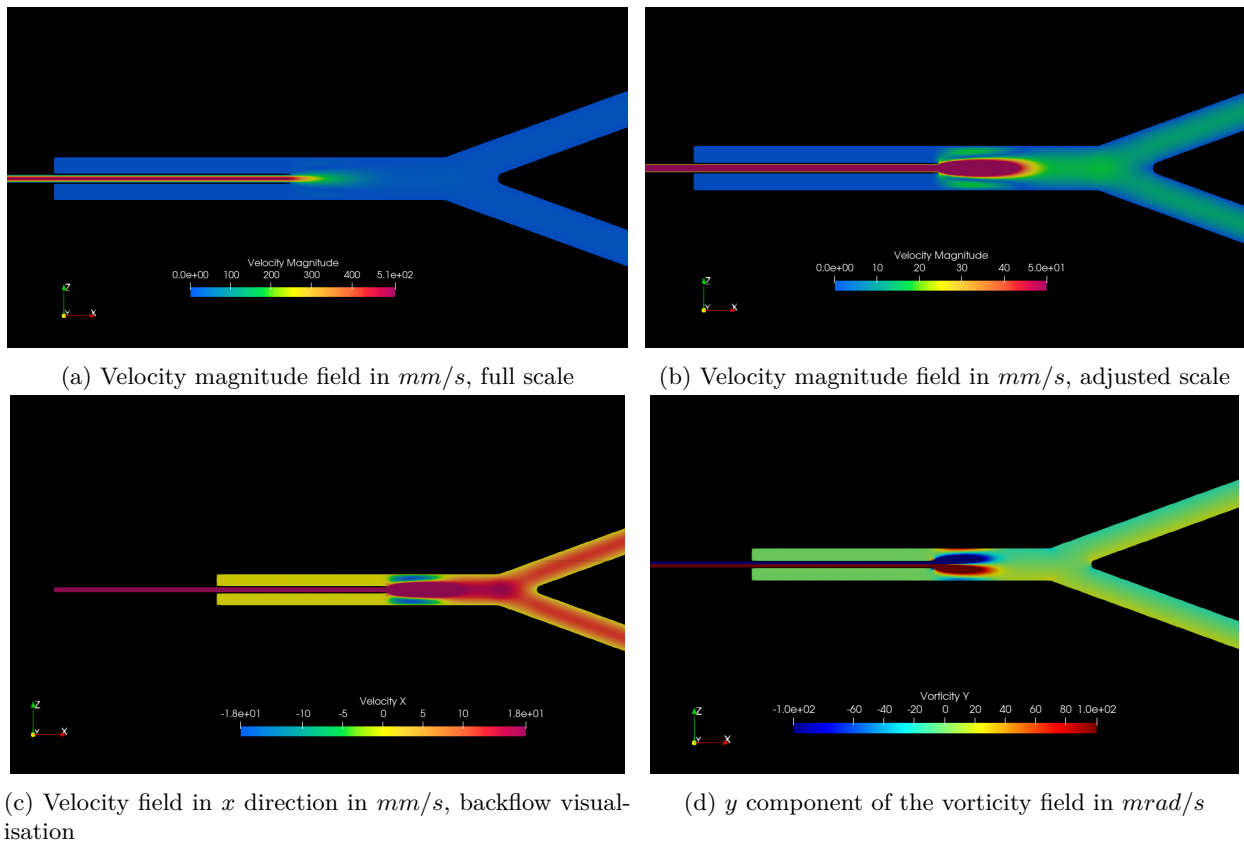


Figure 7.4: Catheter fields, case 1: no angle, far from the bifurcation

In the velocity plots of figure 7.4, it can be seen that a jet is coming out of the catheter. The jet spread out a bit, while the velocity decreases, until the jet vanishes. Above and below the jet similar flow is observed, which is expected from the symmetry in the model. In the backflow plot, it can be seen that after the outlet of the catheter the velocity reverses direction above and below the catheter. These results can be translated to the vorticity plots, where an increase in vorticity is observed near the walls. In the middle of the catheter, the vorticity is very low, which increases closer to the sides of the catheter. From this, it is expected that the streamlines in the middle of the catheter change only slightly, while the streamlines near the walls of the catheter do change direction. In figure 7.5, the streamlines for this case are given, coloured by the velocity.

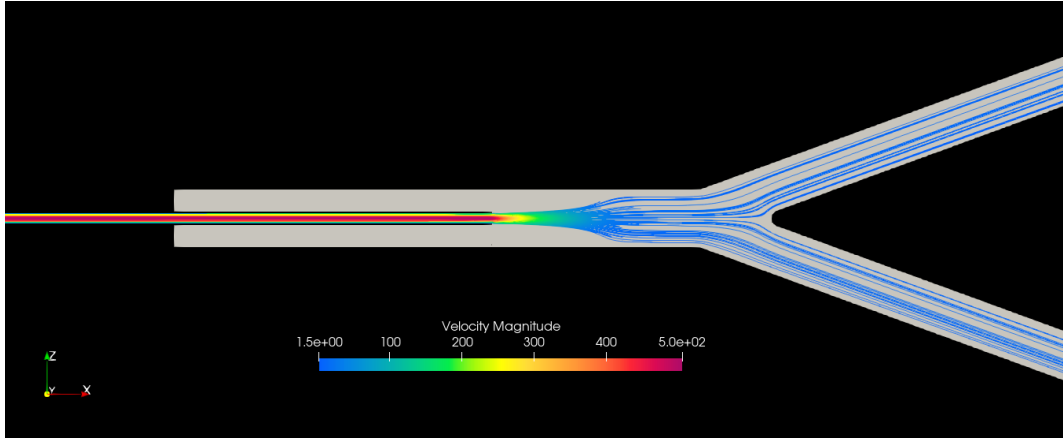


Figure 7.5: Streamlines from the catheter, case 1: no angle, far from the bifurcation

In the figure, it can be seen that the streamlines show the predicted behaviour. The divergence of the streamlines is expected to be less when an external flow is included. Only the inner vorticity regions in figure 7.4c are expected to have an influence on the flow. The outer vorticity regions are located in a region where the velocity is very low. These vorticity regions are not likely to be observed with the external blood flow, as this is expected to be a result of injection in a stagnant fluid. In figure 7.6 a glyph plot is given, including the vorticity and the glyphs coloured by the velocity magnitude.

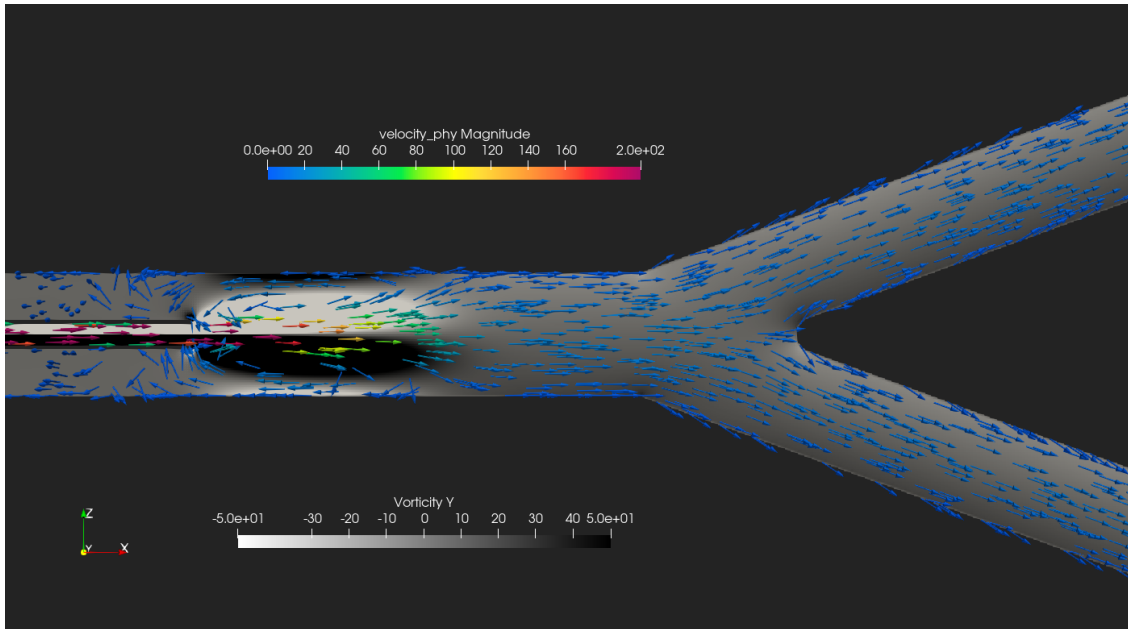
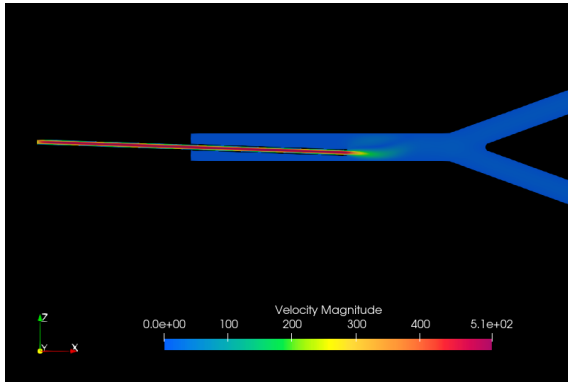
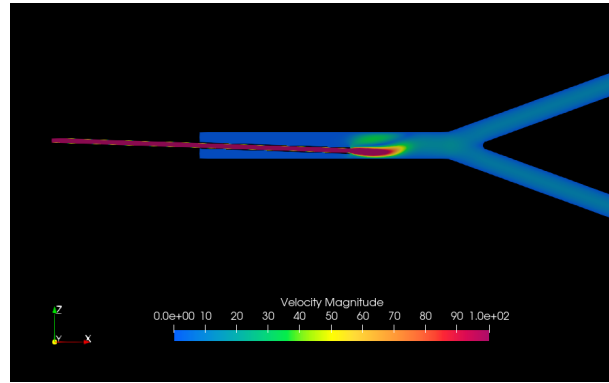


Figure 7.6: Velocity field visualisation using velocity magnitude ( $mm/s$ ) coloured glyphs and the  $y$  component of the vorticity ( $mrad/s$ ), case 1: no angle, far from the bifurcation

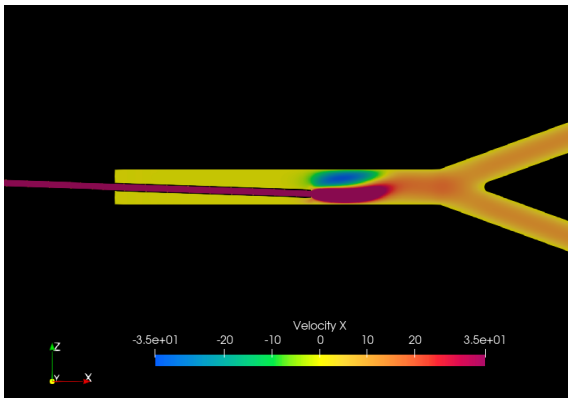
From this plot, an impact is only expected from the high velocity region, which is just after the catheter. From this analysis, the prediction is that straight catheter injection far from the bifurcation will give quite similar results as the earlier calculated distribution maps. The flow disturbance seems to be minor based on these results. Now, the catheter is put at an angle of  $2^\circ$ . The results are given by figure 7.7.



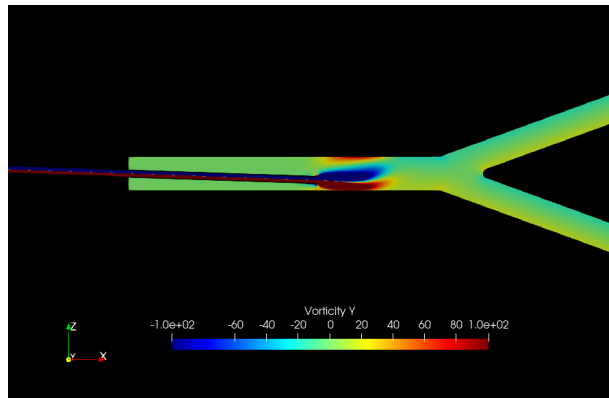
(a) Velocity magnitude field in  $mm/s$ , full scale



(b) Velocity magnitude field in  $mm/s$ , adjusted scale



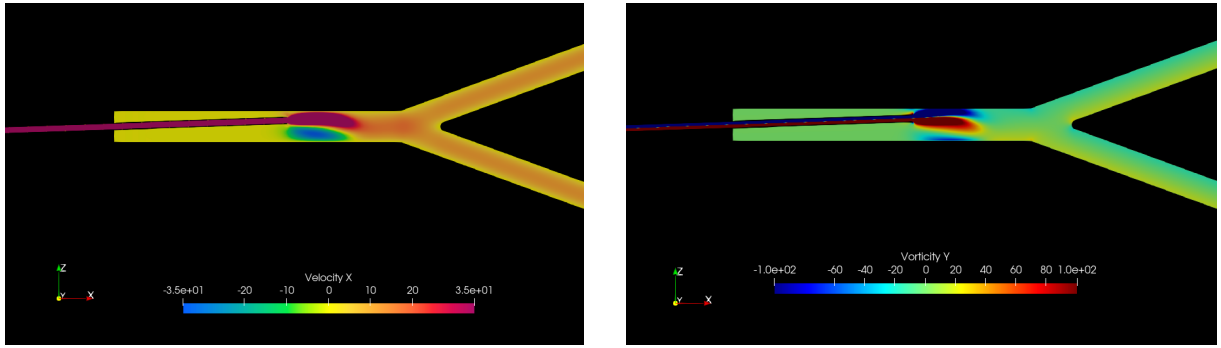
(c) Velocity field in  $x$  direction in  $mm/s$ , backflow visualisation



(d)  $y$  component of the vorticity field in  $mrad/s$

Figure 7.7: Catheter fields, case 2: tilted catheter, far from the bifurcation

In the velocity plots in figure 7.7, the jet coming out of the catheter is again clearly visible. In the backflow plot, the main difference compared to the previous case is that there is now only one region with backflow above the catheter. The value of the backflow is also higher, which means that the influence on the external flow by the catheter injection is higher for the inclined catheter. The angle of the catheter causes the jet to bounce off the wall, which also changes the direction of the high velocity region. The vorticity plots are similar to the previous case, however the tilted catheter does alter the region of the lower high red vorticity region slightly. The backflow and vorticity plot correspond again and circulation is again observed in this simulation. An extra test to ensure consistency of the results was carried out by running a simulation with a mirrored model. The results for the backflow and vorticity can be found in figure 7.8.



(a) Velocity field in  $x$  direction in  $mm/s$ , backflow visualisation

(b)  $y$  component of the vorticity field in  $mrad/s$

Figure 7.8: Catheter fields, mirrored case 2: tilted catheter, far from the bifurcation

In figure 7.8 the same flow patterns and values are observed as in 7.7. This means that the used grid gives a consistent simulation and it also gives some information about the accuracy based on similar velocity and vorticity values. In figure 7.9 some streamlines are plotted for this case.

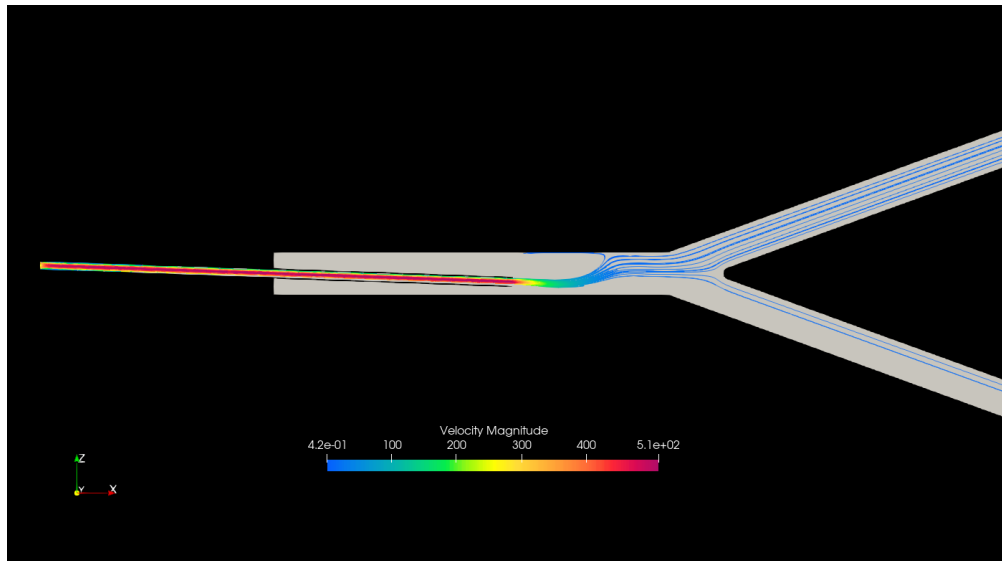


Figure 7.9: Streamlines from the catheter, case 2: tilted catheter, far from the bifurcation

In the figure, it can be seen that most streamlines go to the upper region of the vasculature, which contradicts with the catheter placement. This can be explained as an effect of the static fluid simulation and the low velocity streamlines will likely not have the same rotation as observed in the simulation. The streamlines are affected by the vorticity, however the results is difficult to see due to the high velocity and relatively low vorticity. In figure 7.10 the velocity field is visualised using glyphs that are coloured by the velocity magnitude again. The vasculature cross section itself is coloured by the vorticity. The scale here is a bit different compared to figure 7.6 regarding the velocity, which is used to highlight the impact of the catheter injection on the region above the catheter outlet.

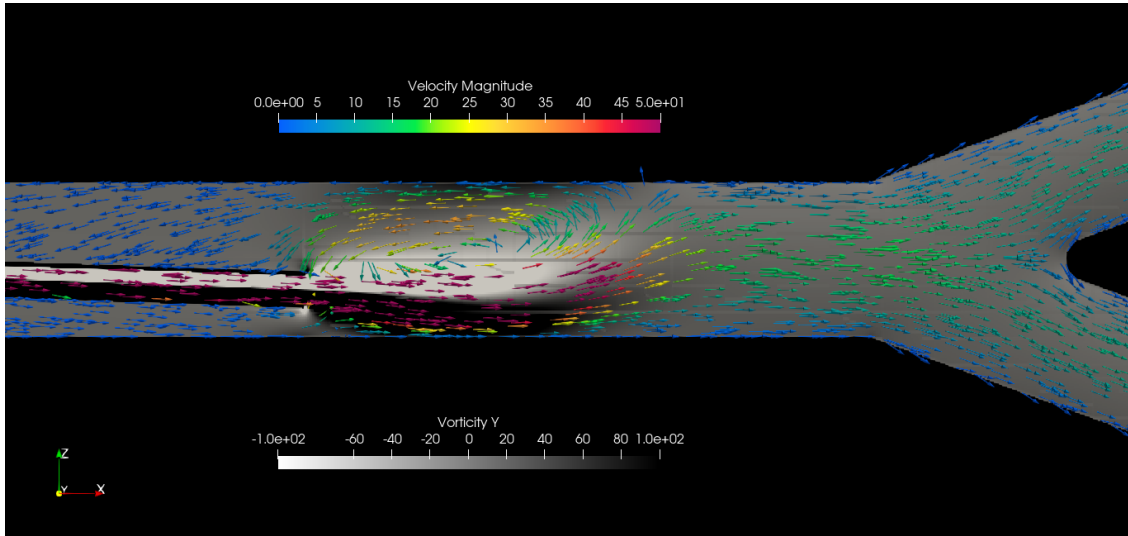
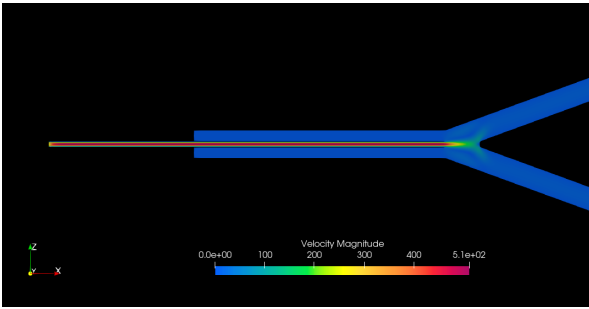


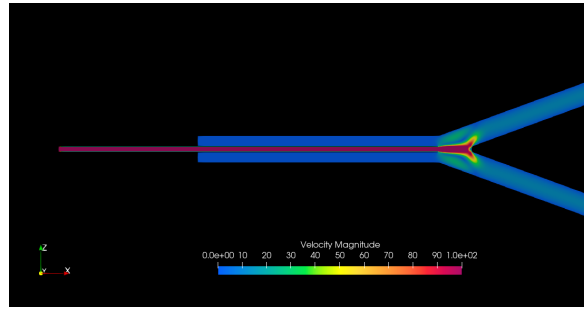
Figure 7.10: Velocity field visualisation using velocity magnitude ( $mm/s$ ) coloured glyphs and the  $y$  component of the vorticity ( $mrad/s$ ), case 2: tilted catheter, far from the bifurcation

In the figure, it can be seen that the streamlines are affected by the vorticity. Flow that remains in this high vorticity region is affected more, which results in the circulation above the catheter. For higher velocities, the vorticity values are too low and they only have a small effect on the direction of the flow. The backflow region will likely not be found with the external flow, as it is expected that this is an effect due to the injection in a stagnant fluid. In the simulation, the extra vorticity implies more flow rotation. The geometry of the catheter could also cause extra rotation to the flow as it is not parallel to the flow. The jet that bounces off the wall will likely still be visible with the external flow, which could cause a different particle distribution compared to a horizontal catheter with the outlet at the same location. Especially the injection speed could be interesting in this case, as it could have an especially large impact on the distribution with a tilted catheter.

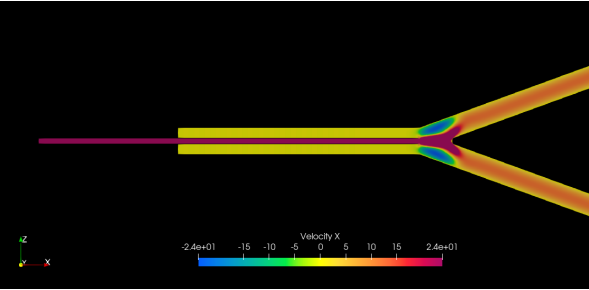
For the next case, the catheter is placed closer to the bifurcation. First, the results of this case without a catheter angle will be discussed. The results are given by figure 7.11.



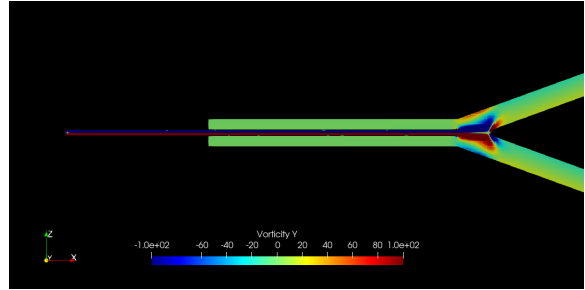
(a) Velocity magnitude field in  $mm/s$ , full scale



(b) Velocity magnitude field in  $mm/s$ , adjusted scale



(c) Velocity field in  $x$  direction in  $mm/s$ , backflow visualisation



(d)  $y$  component of the vorticity field in  $mrad/s$

Figure 7.11: Catheter fields, case 3: no angle, close to the bifurcation

In figure 7.14 it can be seen that the jet that comes out of the catheter is really affected by the proximity of the wall. A splitting effect of the jet can be seen in the figures, with some high velocity regions on the inside on both sides of the bifurcation. Due to this high velocity region and the static fluid, a large backflow area is created around the catheter. The more peripheral flow that comes out of the catheter is affected most by the vorticity, because of the combination of relatively low velocity and high vorticity. The backflow region is likely again caused by the injection in a stagnant fluid. In figure 7.12, some streamlines are plotted for this case.

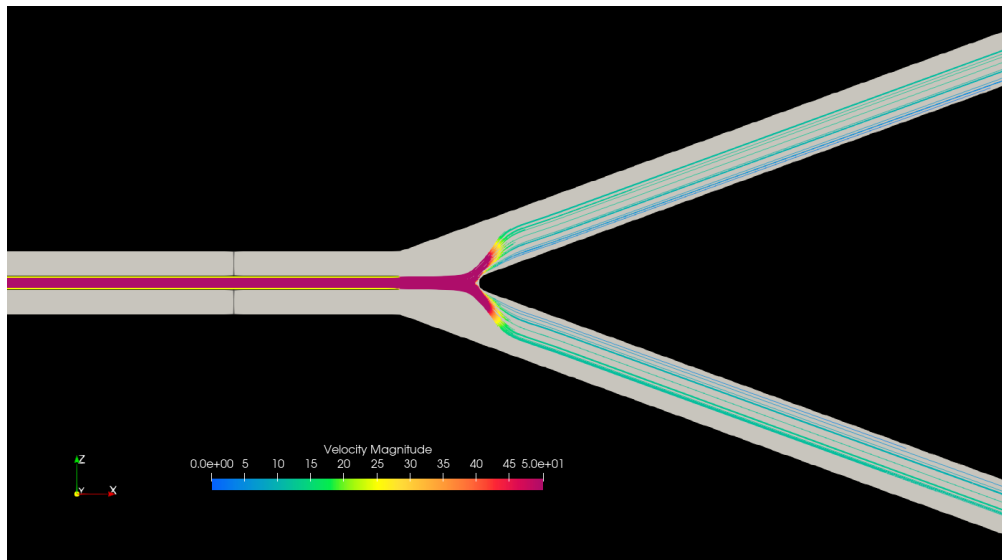


Figure 7.12: Streamlines from the catheter, case 3: no angle, close to the bifurcation

In figure 7.12 it can be seen that putting the catheter closer to the bifurcation leads to the splitting of the jet. Due to the splitting, a high velocity region is created that pushes the flow more to the centre of the vessels after the bifurcation. For case 1, it is expected that the streamlines will go mostly through the middle, around the bifurcation and close to the inner walls after the bifurcation. For case 3, it is expected that the streamlines flow further away from the inner walls after the bifurcation due to the high velocity of the splitted jet. It is expected that the streamlines from the catheter in case 1 will mostly flow to the central outlets 4 and 5, while the streamlines from the catheter in case 3 could also flow to more peripheral outlets like outlets 3 and 6. The glyphs and vorticity are given for this case, by figure 7.13.

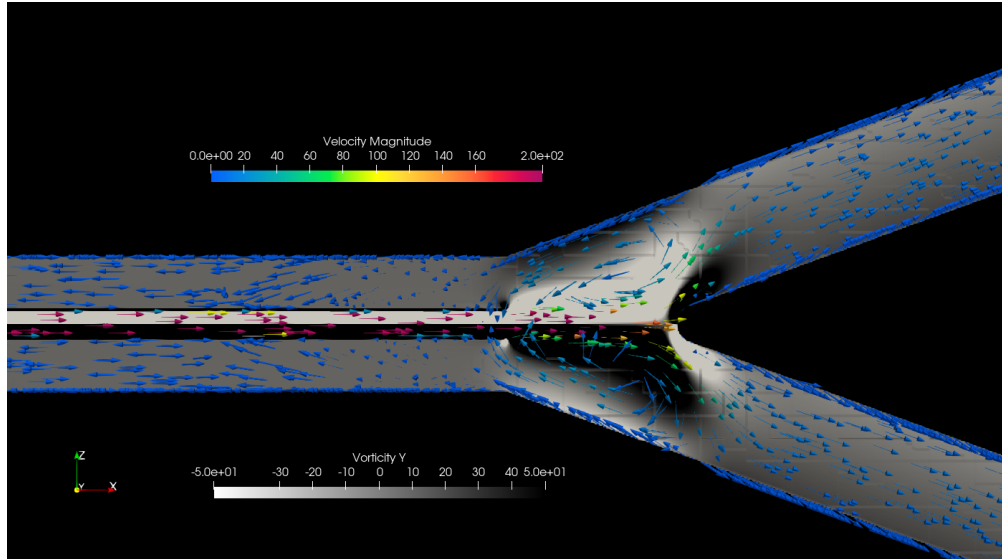
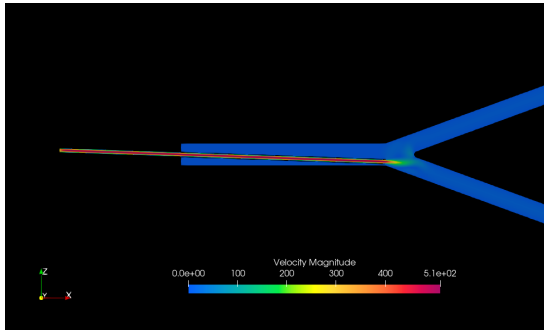
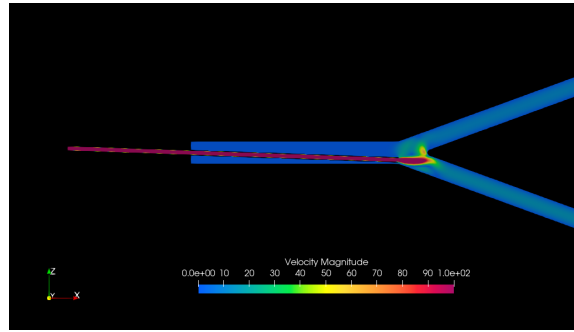


Figure 7.13: Velocity field visualisation using velocity magnitude ( $mm/s$ ) coloured glyphs and the  $y$  component of the vorticity ( $mrad/s$ ), case 3: no angle, close to the bifurcation

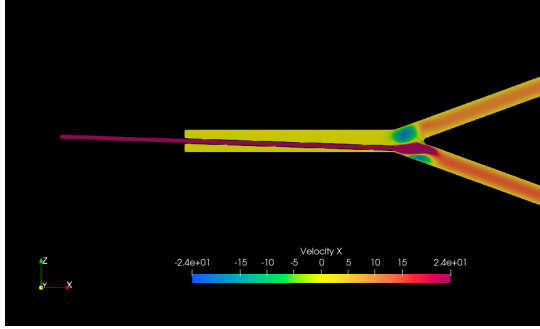
From this figure, it can be seen that there are some large vorticity regions around the bifurcation created by the injection jet. It is expected that placing the catheter closer to the bifurcation will cause a larger flow disturbance compared to an injection location further upstream. For the last case, the elongated catheter is put at an angle that is the same as in case 2. The results can be found in figure 7.14.



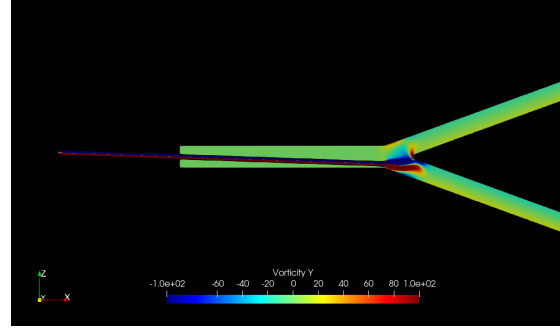
(a) Velocity magnitude field in  $mm/s$ , full scale



(b) Velocity magnitude field in  $mm/s$ , adjusted scale



(c) Velocity field in  $x$  direction in  $mm/s$ , backflow visualisation



(d)  $y$  component of the vorticity field in  $mrad/s$

Figure 7.14: Catheter fields, case 4: tilted catheter, close to the bifurcation

In the last case, the catheter injection is really focused on the lower vessel in the bifurcation. The entire jet from the catheter develops in the direction of this vessel. It looks like a part of this jet goes to the other vessel in the velocity magnitude plot in figure 7.14b, however in the backflow plot it can be seen that this is part of the backflow region above the catheter. From these plots it is expected that most if not all of the streamlines will go into the lower section of the vasculature. The streamlines can be found in figure 7.15.

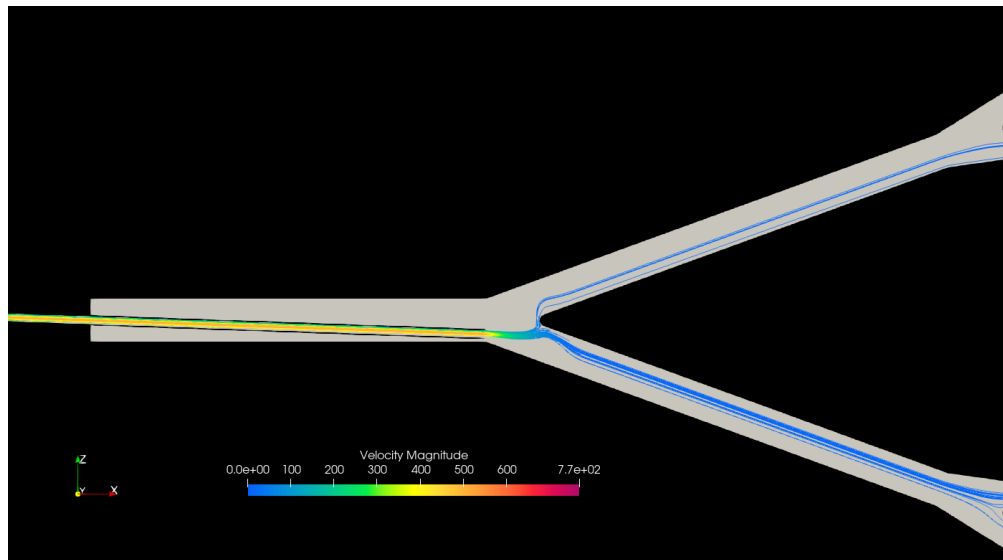


Figure 7.15: Streamlines from the catheter, case 4: tilted catheter, close to the bifurcation

Most of the streamlines follow the predicted path to the lower section of the vasculature. The streamlines that go to the upper section will most likely not follow the same path and are caused by the injection in the stagnant fluid. In figure 7.16 the flow field is again visualised using glyphs and the vorticity.

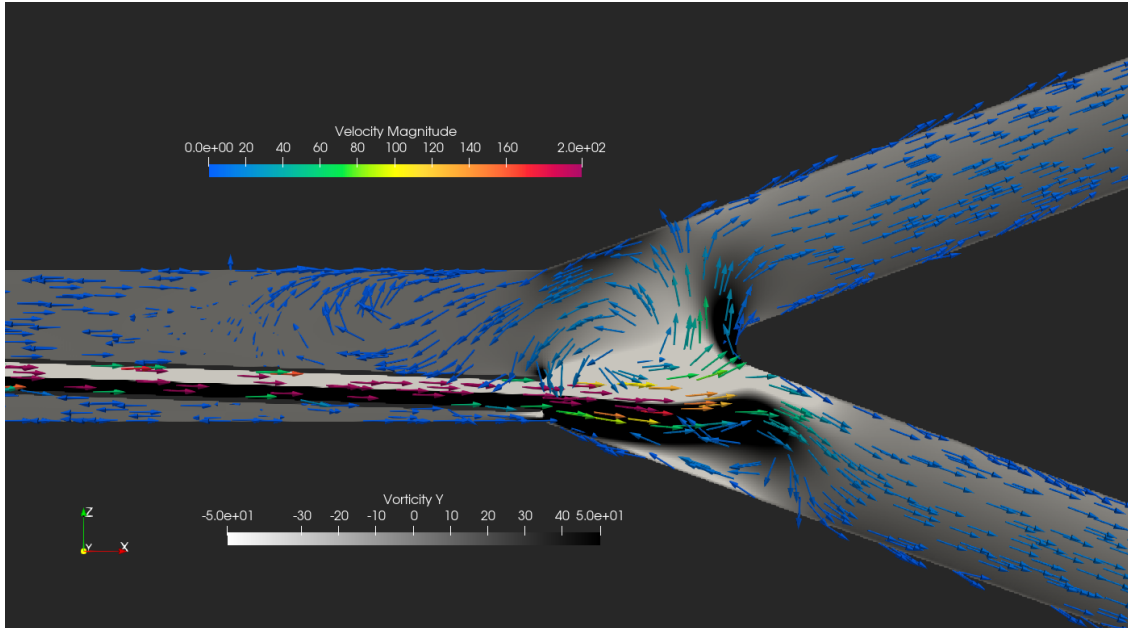


Figure 7.16: Velocity field visualisation using velocity magnitude ( $mm/s$ ) coloured glyphs and the  $y$  component of the vorticity ( $mrad/s$ ), case 4: tilted catheter, close to the bifurcation

In the figure it can be seen that the region around the bifurcation is again influenced. The region above the catheter has quite a low velocity in general, which will likely only cause a minor flow disturbance. It is expected that the flow is also disturbed by the geometry of the catheter, because the placement is again not parallel to the flow. The streamline plots of case 2 and 4 imply that the streamline distribution to the lower section of the vasculature is higher for case 4. For case 2, it is uncertain how the streamlines will develop with an external flow, while for case 4 it is clear that the streamlines will go to the lower section.

In general, it can be concluded that the catheter setup has a large influence on the streamlines and thus the microspheres distributions. The different cases already give some implications on the streamline development. While it is possible to plot streamlines, quantification of the streamlines in a stationary fluid does not mean anything physical and conclusions on the exact particle distributions should not be drawn based on those results.

## Chapter 8

# Discussion, conclusions and recommendations

In this chapter the results will be discussed by focusing on the research question and sub questions that were stated in the introduction. In an attempt to assess the results, comparisons will be made to similar studies. Based on the discussion, conclusions will be drawn and recommendations will conclude the chapter. In this chapter, the degree of uncertainty in the results will be covered to give a clear indication of which aspects are conclusive and which aspects require further research.

### 8.1 Discussion

In this section different aspects of the results will be discussed. First, the validity of the model is discussed. After that, the results are discussed, with the focus on microsphere distribution. Lastly, the catheter study will be discussed.

Large deviations exist in the hepatic artery networks in patients. The variations exist in the RHA itself, but also on a larger scale with as an example differences in where the RHA originates from [81]. The choice for a simplified model can be substantiated from this information, as the simple model could function as a baseline for future models. The simplified model has been analysed and the results have been verified by experiments. From this, important aspects could be identified which should really speed up the process of correctly setting up LB simulations with more complex models. Also, some results of the simplified model could be used to assess the results from the patient specific models regarding streamline and possible some types of microsphere distributions. With these results, conclusions might be drawn in the future on the degree to which patient specific models should be represented accurately for a good indication of microsphere distribution. Also, complexity changes in the model can be analysed to see which changes really influence the microsphere distribution. While the model does show promise, it is not expected that the results now could already be applied in practice because of too many unknowns in the results.

In the simulations and experiments, the Newtonian fluid BMF is used to represent the blood flow. While the choice for this fluid decreases the complexity in the simulations, a perfect representation of the flow is not achieved since blood is a non-Newtonian fluid. The dynamic viscosity changes with the shear rate and thus the velocity of the flow for blood, which results in differences in reported viscosity values for blood. In healthy adults, Yousif et al. report a dynamic viscosity of  $4.4 \pm 0.6$  cP [82]. Three values of the dynamic viscosity are reported by Yazdi et al., with the dynamic viscosity given as  $3.26 \pm 0.43$  cP,  $4.37 \pm 0.60$  cP and  $5.46 \pm 0.84$  cP. for shear rates of 100, 50 and  $1 \text{ s}^{-1}$  respectively [83]. The BMF that is used in the experiments is made at Fisher Scientific in the Netherlands and has a viscosity of 4.2 cP, which should be in the appropriate viscosity range for the flow in the RHA. Large changes in the shear rates are mostly observed in smaller vessels like capillaries and it is expected that the shear thinning effect is less pronounced in vessels with larger dimensions. Also, the choice for using the Newtonian fluid BMF for the simulations is substantiated as it allows comparison to the in-vitro experiments. The effect of the shear thinning in the vasculature model may be studied in future research.

In the model, the walls of the vessels are rigid. In CFD it is possible to obtain results with moving vessel walls by using Fluid Structure Interaction (FSI) models, however the simulation time increases drastically if this is used [84]. In most of these models, a new mesh has to be generated if the wall is moved. In the study by Siogkas et al. it is concluded that deformable walls increase the CPU drastically, which can only be justified if a clinician needs accurate results regarding the vessel wall location. The high correlation between the flow results from a rigid model and a elastic walls model substantiates the choice for the rigid walls and it is expected that the effect will be small on the velocity field.

The results in this report are mostly judged based on the outflow and point values at probes. From the convergence study on the final model, it can be concluded that the numerical accuracy is high enough. One aspect that really influenced the simulation results is the placement of the boundary condition at the outlets. The accuracy of the placement has improved, which drastically changed the results and forms a good comparison with the in-vitro experimental work performed with the same model at the University of Twente. However, the deviations in the experiments are relatively large and the agreement in results is based on these deviations, which are larger than the difference between the simulations and experiments. While the simulations results are good enough for the analysis, other boundary conditions might be interesting if a higher accuracy is desired.

Recently, a CFD study on  $^{90}\text{Y}$  radioembolization has been performed by Antón et al., with the main purpose of developing a microsphere distribution tool to optimise radioembolization on a patient specific level [85]. It shows that CFD modelling is an option to improve personalised radioembolization treatments and it can be used as a very nice comparison to the work in the entire project that this thesis is a part of. In this study, a difference between the blood flow and the microsphere distribution is observed, which gives an indication that the yttrium-90 microspheres are not passive particles. This behaviour is still to be investigated for holmium-166 particles, however an indication is given that these particles will also not follow the streamlines perfectly. The comparison between the streamlines and the microbubble distribution in figure 6.40 is quite good however and comparison with other particle types could give very interesting results. Also, the streamline distribution maps could again form a baseline for the microsphere distribution, where the degree of activity of the particles could be assessed by using the maps.

The catheter type effect on microsphere distribution has been analysed in a hepatic arterial model by Van den Hoven et al. [5]. It is concluded that the catheter type has a significant effect on the microsphere distribution and administration in a vascular network. While a different type of catheter is used, it is shown that an off-centre placement of the catheter resulted in a difference in microsphere distribution, which is in accordance with the qualitative catheter study. Yttrium-90 microsphere deposition is also affected by parameters such as the distance between the catheter tip and an arterial bifurcation, the radial position of the catheter in the artery, the catheter injection speed and the type of catheter tip, stated in the work by Antón et al. [85]. The effects of the former two have been studied in the catheter study and the other mentioned parameters could also be studied by simulating in a similar way by adding more catheter setups. From the results of the catheter study, it is concluded that the two studied parameters disturb the flow in different ways and indeed yield different streamlines and thus microsphere distributions.

Different models have been used for the simulations in this chapter, which have offered a lot of insight into the Musubi software. By resolving the errors in the models and simulation, more confidence in the results of the simulations is achieved. On the other hand, errors in the models and the simulations have resulted in the usage of more computational hours than expected beforehand, which have also consumed a lot of time. Moreover, problems with the supercomputer itself wasted a lot of the used CPU hours and acquiring results often took much longer than expected with these problems. The LB simulations were largely ran on the Dutch national supercomputer Cartesius. Many simulations were performed, ranging from 20 million elements to 400 million elements. Results for simulations with a large number of elements especially took very long due to a lack of stability of the supercomputer and segmentation errors. The relatively smaller simulations with about 40 million elements eventually ran reliably and Cartesius has improved a lot regarding stability during this research. Also, Cartesius will be replaced by a new system called Snellius, which is expected to guarantee a higher computational stability. After optimisation, like reducing the simulation time, results are obtained using a simulation with 40 million element in about 30 minutes on 80 nodes (1920 cores), which is about

1000 CPU hours. The steady state simulations for the catheter use about half the CPU hours. The whole thesis has cost about 3 million CPU hours.

## 8.2 Conclusions

This research aims to answer the question: *To what extent can we predict and identify the clinical aspects that influence the microsphere distribution in the liver vasculature using computational modelling?* To answer this question, LBM simulations were performed on a simplified RHA model which were verified by experiments. From the simulations, a prediction of the microsphere distribution has been made based on the streamlines of pure flow. Also, the effects of the catheter injection have been studied and results show that the catheter injection will have an effect on the distribution.

The biggest problem that was experienced in LBM simulations concerns the pressure boundary condition. It was shown that the placement of the boundary condition is very important for an accurate flow distribution that corresponds to the experiments. The implemented boundary condition placement by defining a plane in Seeder is very prone to placement imprecision and the boundary condition should be imposed on a separate object that can be defined in CAD software. Next to the placement, it was also shown that the outlet lengths have a large impact on the pressure gradient, which yields outflow results that deviate from the outflows found in the experiments. Regarding the future switch to patient specific models, LBM can be a very suitable CFD method for flow simulations in these often complex vasculature networks if the pressure at the outlets is known.

For the final RHA model, simulation results are in agreement with the experimental results. The difference between the outflow rates found in the simulations and experiments is within 5%, which is a good match considering the accuracy of the experimental results.

With the validation of the simulations, streamlines of the flow have been computed at different time instances to predict the microsphere distribution. It is found that the velocity has a large impact on the distribution, while the impact of the acceleration is negligible. The biggest changes happen around the first bifurcation where clear differences in streamline shapes can be distinguished for the different time instances.

The pure flow streamlines should match with weightless particle trajectories, however particles with a mass might follow different trajectories. A steady state simulation that tracks microbubble trajectories is compared to the predicted distribution from the streamlines of the flow, which shows a good comparison. For Holmium-166 particles, the validity of the streamlines for the distribution is still to be investigated.

For the catheter influence, four different positions were simulated to predict the impact that the injection location could have on the distribution. This is done by analysing the resulting streamlines from the catheter, together with the velocity and vorticity fields. The velocity fields are also visualised by using glyphs to see the direction of the velocity. From this study, it can be concluded that the injection location distance from the bifurcation and the bifurcation angle are important parameters that influence the flow, streamlines and thus microsphere distributions. Quantification of the streamlines in a stationary fluid is however not possible and the impact of these setups can only be estimated.

In radioembolization, the microsphere distribution is determined by pre-treatment in-vivo simulation, where surrogate particles are released in an hepatic artery to predict the distribution. In this thesis, the first steps of in-silica simulations to improve or even replace this pre-treatment procedure have been made. The Lattice Boltzmann Method is a suitable CFD method to study the flow in a vasculature. While there are still many aspects to be studied, computational modelling could provide the results to improve radioembolization outcomes in the future.

## 8.3 Recommendations

Based on the conclusions and the goals of the project and this report, several recommendations for future research can be made.

In the simulations some assumptions are made which mostly simplify the complexity and computational requirements, like the usage of a Newtonian fluid model and the assumption of the inelastic walls. While these assumptions might have some effect on the results, it was already mentioned in the discussion that these assumptions will likely not have a big effect on the results. For future research, the focus should lie on the expansion of this model to patient specific models and active particle tracking in the vasculature rather than on showing the validity of these assumptions.

It took quite a long time to get correct results for the last vasculature model. From the errors in the model, the pressure boundary condition had the largest impact on the results. It was found that the placement was crucial for the outflows, which might give problems for future models with a more complex geometry and outlets of uneven length. The pressure boundary condition used is the *pressure\_expol* boundary condition. Other boundary conditions exist like the *pressure\_eq* condition, which might have a higher tolerance for the placement and better results for the pressure gradients for uneven outlet lengths. The option was tested in this thesis, however due to other errors in the model the new boundary condition type seemed to have no effect. To test the effects of other boundary condition types, the final model with the old placement could be used. If the results are more similar to the final model with the new placement, then the boundary condition gives more tolerance for the placement and could be a better option for any new models.

For future research with computational modelling, LBM has proven to be a suitable method for solving flow problems in vasculatures, based on the results that have been presented in this report. One of the advantages of LBM is the possibility for fluid simulations in complex geometries. The patient specific models are often quite complex and Musubi can be recommended for CFD analysis of flow in these models. Also, due to the nature of LBM, implementation of particle coupling can be done to study the behaviour of holmium-166 particles. This is also currently being implemented in Musubi by T. Vlogman, which will hopefully give more insights into the behaviour of these particles.

# Bibliography

- [1] K. J. Lafaro, A. N. Demirjian, and T. M. Pawlik, “Epidemiology of Hepatocellular Carcinoma,” *Surgical Oncology Clinics of North America*, vol. 24, no. 1, 1 2015.
- [2] G. C. Sotiropoulos, H. Lang, A. Frilling, E. P. Molmenti, A. Paul, S. Nadalin, A. Radtke, E. I. Brokalaki, F. Saner, P. Hilgard, G. Gerken, C. E. Broelsch, and M. Malagò, “Resectability of hepatocellular carcinoma: evaluation of 333 consecutive cases at a single hepatobiliary specialty center and systematic review of the literature,” *Hepato-gastroenterology*, vol. 53, pp. 322–329, 2006.
- [3] J. Fletcher, “Liver metastases: Symptoms, diagnosis, and prognosis,” 6 2019. [Online]. Available: <https://www.medicalnewstoday.com/articles/325379>
- [4] A. I. Valderrama-Treviño, B. Barrera-Mera, J. C. Ceballos-Villalva, and E. E. Montalvo-Javé, “Hepatic Metastasis from Colorectal Cancer,” *Euroasian Journal of Hepato-Gastroenterology*, vol. 7, no. 2, p. 166, 2017. [Online]. Available: [/pmc/articles/PMC5670263/](https://pubmed.ncbi.nlm.nih.gov/pmc/articles/PMC5670263/)[https://www.ncbi.nlm.nih.gov/pmc/articles/PMC5670263/](https://pubmed.ncbi.nlm.nih.gov/pmc/articles/PMC5670263/?report=abstracthttps://www.ncbi.nlm.nih.gov/pmc/articles/PMC5670263/)
- [5] A. F. van den Hoven, M. G. Lam, S. Jernigan, M. A. van den Bosch, and G. D. Buckner, “Innovation in catheter design for intra-arterial liver cancer treatments results in favorable particle-fluid dynamics,” *Journal of Experimental & Clinical Cancer Research*, vol. 34, no. 1, 12 2015.
- [6] S. A. Padia, R. J. Lewandowski, G. E. Johnson, D. Y. Sze, T. J. Ward, R. C. Gaba, M. O. Baerlocher, V. L. Gates, A. Riaz, D. B. Brown, N. H. Siddiqi, T. G. Walker, J. E. Silberzweig, J. W. Mitchell, B. Nikolic, and R. Salem, “Radioembolization of Hepatic Malignancies: Background, Quality Improvement Guidelines, and Future Directions,” *Journal of Vascular and Interventional Radiology*, vol. 28, no. 1, 1 2017.
- [7] E. Jafargholi Rangraz, X. Tang, C. Van Laeken, G. Maleux, J. Dekervel, E. Van Cutsem, C. Verslype, K. Baete, J. Nuyts, and C. M. Deroose, “Quantitative comparison of pre-treatment predictive and post-treatment measured dosimetry for selective internal radiation therapy using cone-beam CT for tumor and liver perfusion territory definition,” *EJNMMI Research*, vol. 10, no. 1, 12 2020.
- [8] R. J. Lewandowski and R. Salem, “Yttrium-90 Radioembolization of Hepatocellular Carcinoma and Metastatic Disease to the Liver,” *Seminars in Interventional Radiology*, vol. 23, no. 1, p. 64, 2006. [Online]. Available: [/pmc/articles/PMC3036309/](https://pubmed.ncbi.nlm.nih.gov/pmc/articles/PMC3036309/)[https://www.ncbi.nlm.nih.gov/pmc/articles/PMC3036309/](https://pubmed.ncbi.nlm.nih.gov/pmc/articles/PMC3036309/?report=abstracthttps://www.ncbi.nlm.nih.gov/pmc/articles/PMC3036309/)
- [9] M. L. Smits, J. F. Nijsen, M. A. v. d. Bosch, M. G. Lam, M. A. Vente, J. E. Huijbregts, A. D. v. h. Schip, M. Elschot, W. Bult, H. W. d. Jong, P. C. Meulenhoff, and B. A. Zonnenberg, “Holmium-166 radioembolization for the treatment of patients with liver metastases: design of the phase I HEPAR trial,” *Journal of Experimental & Clinical Cancer Research* 2010 29:1, vol. 29, no. 1, pp. 1–11, 6 2010. [Online]. Available: <https://jccr.biomedcentral.com/articles/10.1186/1756-9966-29-70>
- [10] M. C. Sukop and D. T. Thorne, *Lattice Boltzmann modeling : an introduction for geoscientists and engineers*, 2nd ed. Springer, 2006.
- [11] J. Wu, X. Meng, R. Chu, S. Yu, Y. Wan, C. Song, G. Zhang, and T. Zhao, “Molecular Dynamics Simulation of the Implantation of b-Oriented ZSM-5 Film Modified  $\alpha$ -Quartz Substrate Surface With Different Modifiers,” *Frontiers in Chemistry*, vol. 7, p. 746, 11 2019. [Online]. Available: <https://www.frontiersin.org/article/10.3389/fchem.2019.00746/full>

- [12] A. A. Mohamad, "Lattice Boltzmann Method Fundamentals and Engineering Applications with Computer Codes Second Edition," University of Calgary, Calgary, Tech. Rep., 2019.
- [13] D. Lincoln, "Why Ideal Gas Law Is Not That Ideal," 6 2020. [Online]. Available: <https://www.thegreatcoursesdaily.com/why-ideal-gas-law-is-not-that-ideal/>
- [14] K. Banoo, "DIRECT SOLUTION OF THE BOLTZMANN TRANSPORT EQUATION IN NANO-SCALE SI DEVICES," Ph.D. dissertation, Purdue University, West Lafayette, 2000.
- [15] B. D. Rodriguez, M. T. Vilhena, and B. E. Bodmann, "An overview of the Boltzmann transport equation solution for neutrons, photons and electrons in Cartesian geometry," *Progress in Nuclear Energy*, vol. 53, no. 8, 11 2011.
- [16] A. Paussa and D. Esseni, "An exact solution of the linearized Boltzmann transport equation and its application to mobility calculations in graphene bilayers," *Journal of Applied Physics*, vol. 113, no. 9, p. 093702, 3 2013. [Online]. Available: <https://aip.scitation.org/doi/abs/10.1063/1.4793634>
- [17] J. McEvoy and O. Zarate, *Introducing Quantum Theory: A Graphic Guide to Science's Most Puzzling Discovery*. Icon Books, 10 2013.
- [18] M. Hill, "The Maxwell-Boltzmann Distribution." [Online]. Available: [http://www.hk-phy.org/contextual/heat/tep/trans01\\_e.html](http://www.hk-phy.org/contextual/heat/tep/trans01_e.html)
- [19] A. Maley, "3.1.2: Maxwell-Boltzmann Distributions - Chemistry LibreTexts," 8 2020. [Online]. Available: [https://chem.libretexts.org/Bookshelves/Physical\\_and\\_Theoretical\\_Chemistry\\_Textbook\\_Maps/Supplemental\\_Modules\\_\(Physical\\_and\\_Theoretical\\_Chemistry\)/Kinetics/03%3A\\_Rate\\_Laws/3.01%3A\\_Gas\\_Phase\\_Kinetics/3.1.02%3A\\_Maxwell-Boltzmann\\_Distributions](https://chem.libretexts.org/Bookshelves/Physical_and_Theoretical_Chemistry_Textbook_Maps/Supplemental_Modules_(Physical_and_Theoretical_Chemistry)/Kinetics/03%3A_Rate_Laws/3.01%3A_Gas_Phase_Kinetics/3.1.02%3A_Maxwell-Boltzmann_Distributions)
- [20] P. Young, "Physics 112 Maxwell distributions for the speed and velocity of molecules in a gas (Kittel and Kroemer, p. 392-3)," Oxford University, Tech. Rep., 2 2012.
- [21] M. C. Sukop and D. Or, "Lattice Boltzmann method for modeling liquid-vapor interface configurations in porous media," *Water Resources Research*, vol. 40, no. 1, 1 2004.
- [22] A. Augier, F. Dubois, and B. Graille, "ISOTROPY CONDITIONS FOR LATTICE BOLTZMANN SCHEMES. APPLICATION TO D2Q9 \*," *ESAIM: PROCEEDINGS*, pp. 1–10, 2011.
- [23] H. Chen, I. Goldhirsch, and S. A. Orszag, "Discrete rotational symmetry, moment isotropy, and higher order lattice Boltzmann models," *Journal of Scientific Computing*, vol. 34, no. 1, pp. 87–112, 1 2008.
- [24] S. MARCONI, B. CHOPARD, and J. LATT, "REDUCING THE COMPRESSIBILITY OF A LATTICE BOLTZMANN FLUID USING A REPULSIVE FORCE," *International Journal of Modern Physics C*, vol. 14, no. 08, 10 2003.
- [25] X. He and L. S. Luo, "Lattice Boltzmann model for the incompressible Navier-Stokes equation," *Journal of Statistical Physics*, vol. 88, no. 3-4, pp. 927–944, 1997. [Online]. Available: <https://link.springer.com/article/10.1023/B:JOSS.0000015179.12689.e4>
- [26] Y. Bao, Y. Bill Bao, and J. Meskas, "Lattice Boltzmann Method for Fluid Simulations," New York University, New York, Tech. Rep., 2011. [Online]. Available: <https://www.researchgate.net/publication/265077140>
- [27] J. Li, "Chapman-Enskog Expansion in the Lattice Boltzmann Method," 12 2015. [Online]. Available: <http://arxiv.org/abs/1512.02599>
- [28] A. Mohamad and A. Kuzmin, "A critical evaluation of force term in lattice Boltzmann method, natural convection problem," *International Journal of Heat and Mass Transfer*, vol. 53, no. 5-6, 2 2010.
- [29] I. C. Kim, "Second Order Bounce Back Boundary Condition for the Lat-ice Boltzmann Fluid Simulation," Kunsan National University, Kunsan, Tech. Rep. 1, 2000.

- [30] Y. G. Lai, C.-L. Lin, and J. Huang, “Accuracy and efficiency study of Lattice Boltzmann Method for steady-state flow simulations,” *ACCURACY AND EFFICIENCY STUDY OF LATTICE BOLTZMANN METHOD FOR STEADY-STATE FLOW SIMULATIONS*, *Numerical Heat Transfer: Part B: Fundamentals*, vol. 39, no. 1, pp. 21–43, 2001. [Online]. Available: <https://www.tandfonline.com/action/journalInformation?journalCode=unhb20>
- [31] X. Nie and N. S. Martys, “Breakdown of Chapman-Enskog expansion and the anisotropic effect for lattice-Boltzmann models of porous flow,” *Physics of Fluids*, vol. 19, no. 1, 1 2007.
- [32] Z. Guo and T. S. Zhao, “Lattice Boltzmann model for incompressible flows through porous media,” *PHYSICAL REVIEW*, vol. 66, 9 2002.
- [33] G. Peeters, “Modelling the Degenerative Adaptation of the Liver Vasculature and Perfusion in Cirrhosis,” Ph.D. dissertation, Universiteit Gent, Gent, 2018.
- [34] K. L. Moore, A. F. Dalley, and A. M. Agur, *Clinically Oriented Anatomy*, 7th ed. Baltimore: Lippincott Williams & Wilkins, 2014.
- [35] Z. Ahmed, U. Ahmed, S. Walayat, J. Ren, D. K. Martin, H. Moole, S. Koppe, S. Yong, and S. Dhillion, “Liver function tests in identifying patients with liver disease,” *Clinical and Experimental Gastroenterology*, vol. 11, pp. 301–307, 2018. [Online]. Available: [/pmc/articles/PMC6112813//pmc/articles/PMC6112813/?report=abstracthttps://www.ncbi.nlm.nih.gov/pmc/articles/PMC6112813/](https://pubmed.ncbi.nlm.nih.gov/36112813/)
- [36] “What is liver cancer?” 2019. [Online]. Available: <https://www.cancer.org/cancer/liver-cancer/about/what-is-liver-cancer.html>
- [37] “Abdominal Cavity.” [Online]. Available: <https://www.earthslab.com/anatomy/abdominal-cavity/?dc=ThoraxMuscle-Interface&rm=true>
- [38] “Liver: Anatomy and Functions.” [Online]. Available: <https://www.hopkinsmedicine.org/health/conditions-and-diseases/liver-anatomy-and-functions>
- [39] N. Chudgar and G. Nandakumar, “Anatomic Resections of the Liver,” in *Evidence-Based Practices in Gastrointestinal, Colorectal and Hepatobiliary Surgery*. Jaypee Brothers Medical Publishers (P) Ltd., 2017.
- [40] “Structure and Function of Blood Vessels — Anatomy and Physiology II.” [Online]. Available: <https://courses.lumenlearning.com/suny-ap2/chapter/structure-and-function-of-blood-vessels/>
- [41] “Hematology Glossary - Hematology.org.” [Online]. Available: <https://www.hematology.org/education/patients/blood-basics>
- [42] “CV Physiology — Viscosity of Blood.” [Online]. Available: <https://www.cvphysiology.com/Hemodynamics/H011>
- [43] L. Lanotte, J. Mauer, S. Mendez, D. A. Fedosov, J.-M. Fromental, V. Clavería, F. Nicoud, G. Gompper, and M. Abkarian, “A new look at blood shear-thinning,” *arXiv e-prints*, 8 2016. [Online]. Available: <https://arxiv.org/abs/1608.03730v1>
- [44] “Liver Metastases (Secondary Liver Cancer).” [Online]. Available: <https://www.mskcc.org/cancer-care/types/liver-metastases>
- [45] “The Netherlands Source: Globocan Incidence, Mortality and Prevalence by cancer site,” 2020.
- [46] “Global Source: Globocan Incidence, Mortality and Prevalence by liver cancer site,” 2020. [Online]. Available: <https://geo.iarc.fr/today/data/factsheets/cancers/11-Liver-fact-sheet.pdf>
- [47] “Understanding the different types of liver cancer,” 4 2015. [Online]. Available: <https://utswmed.org/medblog/liver-cancer-types/>
- [48] “Liver Cancer — CDC.” [Online]. Available: <https://www.cdc.gov/cancer/liver/index.htm>

- [49] “Selective internal radiation therapy (SIRT).” [Online]. Available: <https://www.cirse.org/patients/ir-procedures/selective-internal-radiation-therapy-sirt/>
- [50] A. A. Alsultan, A. J. Braat, M. L. Smits, M. W. Barentsz, R. Bastiaannet, R. C. Bruijnen, B. de Keizer, H. W. de Jong, M. G. Lam, M. Maccauro, and C. Chiesa, “Current Status and Future Direction of Hepatic Radioembolisation,” *Clinical Oncology*, vol. 33, no. 2, pp. 106–116, 2 2021.
- [51] L. Bester, B. Meteling, D. Boshell, T. C. Chua, and D. L. Morris, “Transarterial chemoembolisation and radioembolisation for the treatment of primary liver cancer and secondary liver cancer: A review of the literature,” *Journal of Medical Imaging and Radiation Oncology*, vol. 58, no. 3, 6 2014.
- [52] R. Stubbs and S. Wickremesekera, “Selective internal radiation therapy (SIRT): a new modality for treating patients with colorectal liver metastases,” *HPB*, vol. 6, no. 3, 9 2004.
- [53] B. Sangro, M. Iñarrairaegui, and J. I. Bilbao, “Radioembolization for hepatocellular carcinoma,” *Journal of Hepatology*, vol. 56, no. 2, 2 2012.
- [54] E. G. Giannini, F. Farinati, F. Ciccarese, A. Pecorelli, G. L. Rapaccini, M. Di Marco, L. Benvegnù, E. Caturelli, M. Zoli, F. Borzio, M. Chiaramonte, and F. Trevisani, “Prognosis of untreated hepatocellular carcinoma,” *Hepatology*, vol. 61, no. 1, 1 2015.
- [55] R. Hickey, R. J. Lewandowski, T. Prudhomme, E. Ehrenwald, B. Baigorri, J. Critchfield, J. Kallini, A. Gabr, B. Gorodetski, J.-F. Geschwind, A. Abbott, R. Shridhar, S. B. White, W. S. Rilling, B. Boyer, S. Kauffman, S. Kwan, S. A. Padia, V. L. Gates, M. Mulcahy, S. Kircher, H. Nimeiri, A. B. Benson, and R. Salem, “90-Y Radioembolization of Colorectal Hepatic Metastases Using Glass Microspheres: Safety and Survival Outcomes from a 531-Patient Multicenter Study,” *Journal of Nuclear Medicine*, vol. 57, no. 5, 5 2016.
- [56] G. Maleux, C. Deroose, A. Laenen, C. Verslype, S. Heye, K. Haustermans, G. De Hertogh, X. Sagaert, B. Topal, R. Aerts, H. Prenen, D. Vanbeckevoort, V. Vandecaveye, and E. Van Cutsem, “Yttrium-90 radioembolization for the treatment of chemorefractory colorectal liver metastases: Technical results, clinical outcome and factors potentially influencing survival,” *Acta Oncologica*, vol. 55, no. 4, 4 2016.
- [57] R. Drescher, P. Seifert, F. Gühne, R. Aschenbach, C. Kühnel, and M. Freesmeyer, “Radioembolization With Holmium-166 Polylactic Acid Microspheres: Distribution of Residual Activity in the Delivery Set and Outflow Dynamics During Planning and Treatment Procedures,” *Journal of Endovascular Therapy*, vol. 28, no. 3, pp. 452–462, 6 2021.
- [58] C. van Roekel, R. Bastiaannet, M. L. Smits, R. C. Bruijnen, A. J. Braat, H. W. de Jong, S. G. Elias, and M. G. Lam, “Dose–Effect Relationships of  $^{166}\text{Ho}$  Radioembolization in Colorectal Cancer,” *Journal of Nuclear Medicine*, vol. 62, no. 2, 2 2021.
- [59] “Adaptable Poly-Engineering Simulator (APES) — Adaptable Poly-Engineering Simulator.” [Online]. Available: <https://apes.osdn.io/>
- [60] “Motivation for the TreElm Library – Treelm.” [Online]. Available: <https://geb.sts.nt.uni-siegen.de/doxy/treelm/page/motivation.html>
- [61] University of Siegen, “Seeder,” 2020. [Online]. Available: <https://geb.sts.nt.uni-siegen.de/doxy/seedler/index.html>
- [62] J. Latt, “Choice of units in lattice Boltzmann simulations,” University of Geneva, Tech. Rep., 2008.
- [63] —, “Hydrodynamic Limit of Lattice Boltzmann Equations,” Université de Genève, Genève, Tech. Rep., 2007.
- [64] A. S. Dukhin and P. J. Goetz, “Bulk viscosity and compressibility measurement using acoustic spectroscopy,” *The Journal of Chemical Physics*, vol. 130, no. 12, 3 2009.

- [65] Z. Yan, X. Yang, S. Li, and M. Hilpert, “Two-relaxation-time lattice Boltzmann method and its application to advective-diffusive-reactive transport,” *Advances in Water Resources*, vol. 109, pp. 333–342, 11 2017.
- [66] M. Bouzidi, M. Firdaouss, and P. Lallemand, “Momentum transfer of a Boltzmann-lattice fluid with boundaries,” *Physics of Fluids*, vol. 13, no. 11, pp. 3452–3459, 10 2001. [Online]. Available: <https://doi.org/10.1063/1.1399290>
- [67] “About SURF Cooperation — SURF.nl.” [Online]. Available: <https://www.surf.nl/en/about-surf>
- [68] S. M. Richardson, “POISEUILLE FLOW,” 3 2011. [Online]. Available: <https://www.thermopedia.com/content/1042/>
- [69] tec-science, “Energetic analysis of the Hagen-Poiseuille law - tec-science,” 4 2020. [Online]. Available: <https://www.tec-science.com/mechanics/gases-and-liquids/energetic-analysis-of-the-hagen-poiseuille-law/>
- [70] B. Owolabi, *Characterisation of Turbulent Duct Flows*, 1st ed. Basel: Springer, Cham, 2019. [Online]. Available: <https://doi.org/10.1007/978-3-030-19745-2>
- [71] F. J. Gijsen, F. N. Van De Vosse, and J. D. Janssen, “The influence of the non-Newtonian properties of blood on the flow in large arteries: steady flow in a carotid bifurcation model,” *Journal of Biomechanics*, vol. 32, no. 6, pp. 601–608, 6 1999. [Online]. Available: <https://linkinghub.elsevier.com/retrieve/pii/S0021929099000159>
- [72] H. Mirgolbabaee, “In-vitro studies on Womersley flow and microsphere (Holmium-166) distribution in the liver vasculature using Laser PIV,” University of Twente, Enschede, Tech. Rep., 8 2019.
- [73] J. Aramburu, R. Antón, N. Bernal, A. Rivas, J. C. Ramos, B. Sangro, and J. I. Bilbao, “Physiological outflow boundary conditions methodology for small arteries with multiple outlets: A patient-specific hepatic artery haemodynamics case study,” *Proceedings of the Institution of Mechanical Engineers, Part H: Journal of Engineering in Medicine*, vol. 229, no. 4, pp. 291–306, 4 2015. [Online]. Available: <http://journals.sagepub.com/doi/10.1177/0954411915578549>
- [74] N. Maurits, G. Loots, and A. Veldman, “The influence of vessel wall elasticity and peripheral resistance on the carotid artery flow wave form: A CFD model compared to in vivo ultrasound measurements,” *Journal of Biomechanics*, vol. 40, no. 2, 1 2007.
- [75] M. Junk and Z. Yang, “Asymptotic analysis of lattice Boltzmann outflow treatments,” *Communications in Computational Physics*, vol. 9, no. 5, pp. 1117–1127, 2011.
- [76] T. F. Sherman, “On Connecting Large Vessels to Small The Meaning of Murray’s Law,” Department of Biology, Oberlin College, Oberlin, Tech. Rep., 10 1981.
- [77] L. O. Schwen and T. Preusser, “Analysis and Algorithmic Generation of Hepatic Vascular Systems,” *International Journal of Hepatology*, vol. 2012, pp. 1–17, 2012.
- [78] G. S. Krenz and C. A. Dawson, “Flow and pressure distributions in vascular networks consisting of distensible vessels,” *American Journal of Physiology-Heart and Circulatory Physiology*, vol. 284, no. 6, 6 2003.
- [79] “Progreat® Micro Catheter System.” [Online]. Available: <https://www.terumo-europe.com/en-emea/products/progreat%C2%AE-micro-catheter-system>
- [80] “Pushing the Boundaries of Catheter Wall Thickness to Improve Patient Outcomes — Arrotek.” [Online]. Available: <https://www.arrotek.com/pushing-the-boundaries-of-catheter-wall-thickness-to-improve-patient-outcomes/>
- [81] J. R. Hiatt, J. Gabbay, and R. W. Busuttill, “Surgical Anatomy of the Hepatic Arteries in 1000 Cases,” *Annals of Surgery*, vol. 220, no. 1, 7 1994.

- [82] M. Yousif, D. Holdsworth, and T. Poepping, “Deriving a blood-mimicking fluid for particle image velocimetry in sylgard-184 vascular models,” in *2009 Annual International Conference of the IEEE Engineering in Medicine and Biology Society*. IEEE, 9 2009.
- [83] S. G. Yazdi, P. H. Geoghegan, P. D. Docherty, M. Jermy, and A. Khanafer, “A Review of Arterial Phantom Fabrication Methods for Flow Measurement Using PIV Techniques,” *Annals of Biomedical Engineering* 2018 46:11, vol. 46, no. 11, pp. 1697–1721, 7 2018. [Online]. Available: <https://link.springer.com/article/10.1007/s10439-018-2085-8>
- [84] P. K. Siogkas, A. I. Sakellarios, T. P. Exarchos, K. Stefanou, D. I. Fotiadis, K. Naka, L. Michalis, N. Filipovic, and O. Parodi, “Blood flow in arterial segments: rigid vs. deformable walls simulations,” *Serbian Society for Computational Mechanics*, vol. 5, no. 1, pp. 69–77, 1 2011. [Online]. Available: [https://www.researchgate.net/publication/265569957\\_Blood\\_flow\\_in\\_arterial\\_segments\\_rigid\\_vs\\_deformable\\_walls\\_simulations](https://www.researchgate.net/publication/265569957_Blood_flow_in_arterial_segments_rigid_vs_deformable_walls_simulations)
- [85] R. Antón, J. Antoñana, J. Aramburu, A. Ezponda, E. Prieto, A. Andonegui, J. Ortega, I. Vivas, L. Sancho, B. Sangro, J. I. Bilbao, and M. Rodríguez-Fraile, “A proof-of-concept study of the in-vivo validation of a computational fluid dynamics model of personalized radioembolization,” *Scientific Reports*, vol. 11, no. 1, 12 2021.

## Appendix A

# Right Hepatic Artery: initial wrong results

In the figures below, the results for the initial wrong small angle vasculature model are given. These plots contain errors like the boundary placement, tracking and asymmetry which are all explained in the text. A very fine mesh is used for these simulations with about 300 million elements.

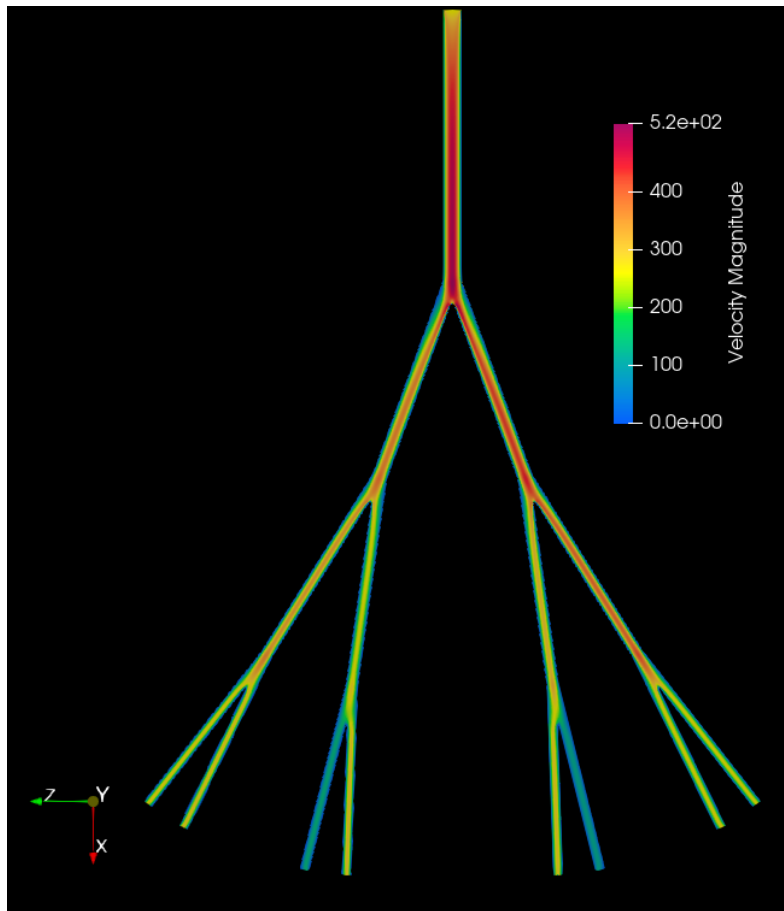


Figure A.1: Velocity field in  $mm/s$  at the start of the cardiac cycle

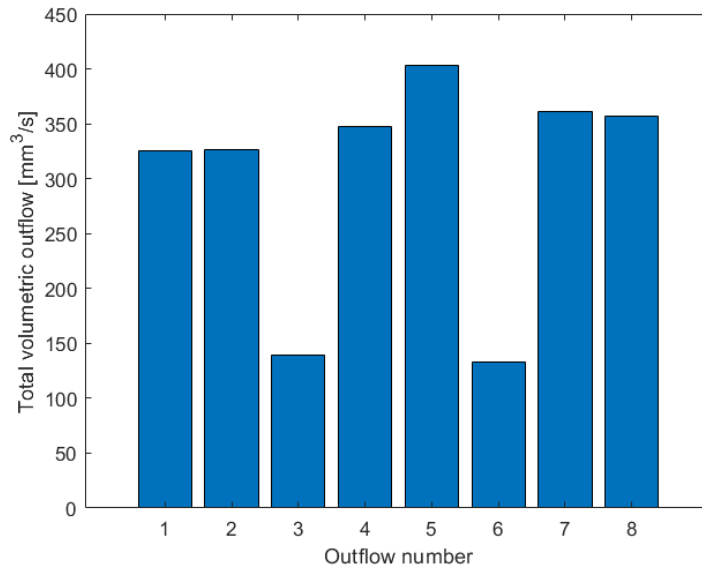


Figure A.2: Tracked volumetric outflows over one cardiac cycle

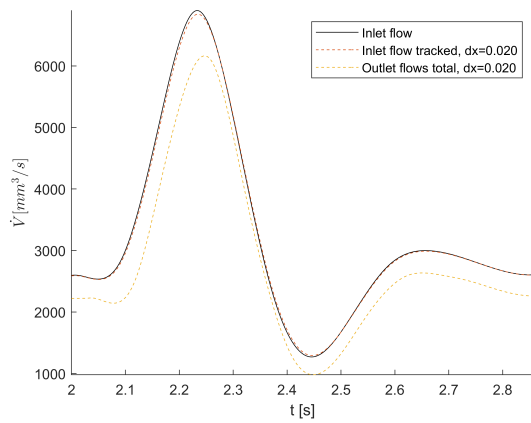


Figure A.3: Tracked inflow and outflows compared to the prescribed inflow during the cardiac cycle

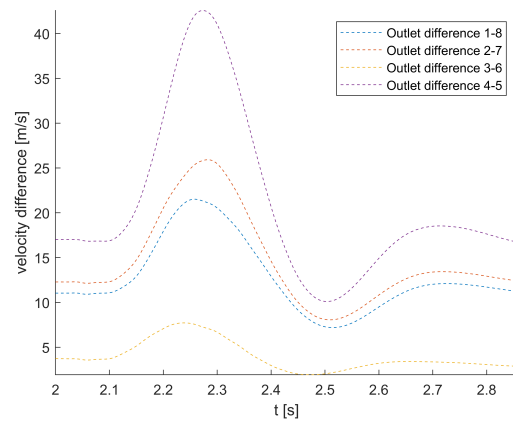


Figure A.4: Velocity differences between the symmetric outlets during the cardiac cycle

## Appendix B

# Right Hepatic Artery: more scalar and vector field results

In the figures below, the velocity fields for all 6 time instances identified in figure 6.4 are given. The full range of the velocity fields is displayed.

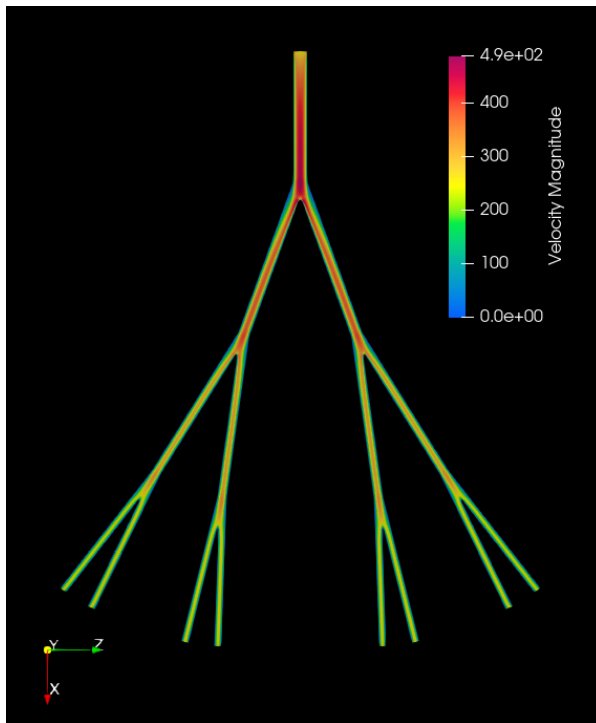


Figure B.1: Velocity magnitude field at the start of the cardiac cycle, in  $mm/s$

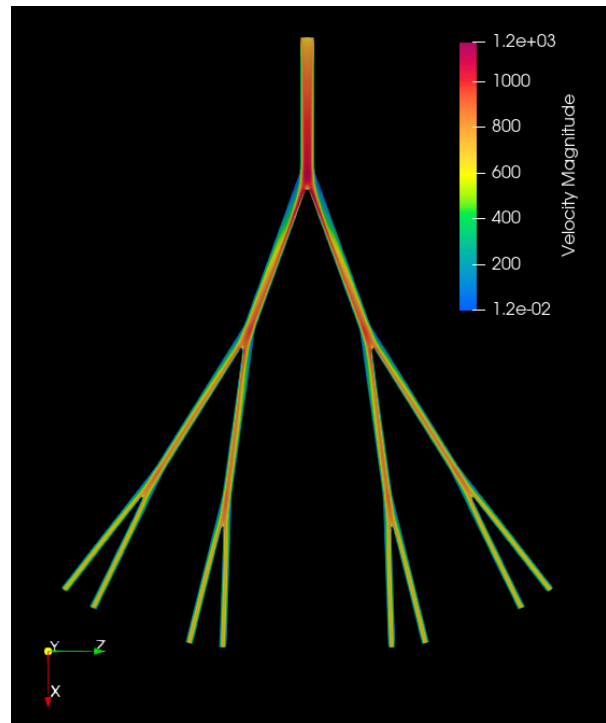


Figure B.2: Velocity magnitude field during the acceleration phase of the cardiac cycle, in  $mm/s$

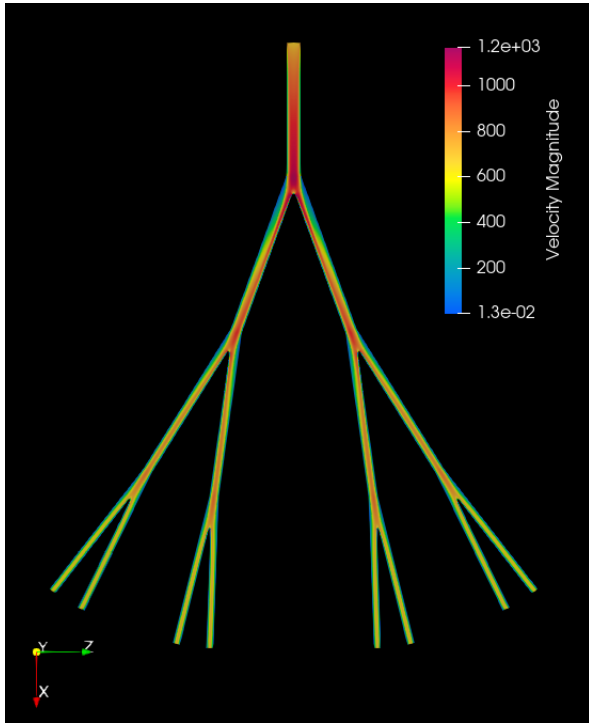


Figure B.3: Velocity magnitude field at peak systole in the cardiac cycle, in  $mm/s$

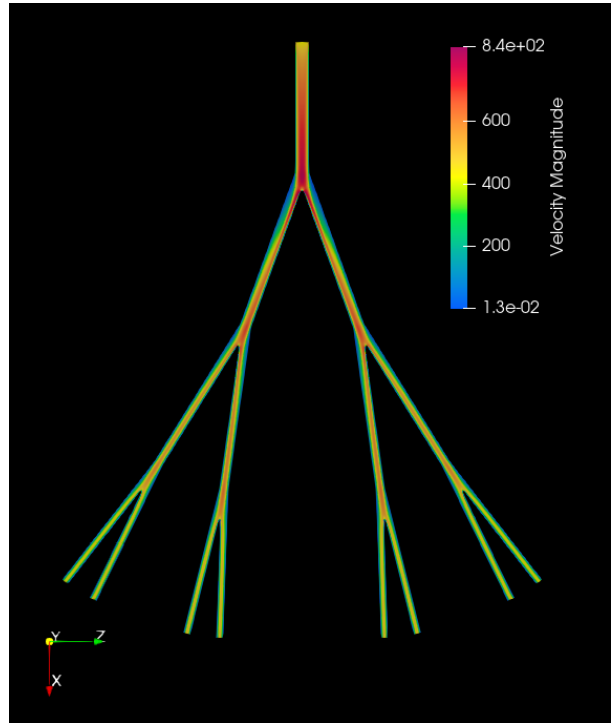


Figure B.4: Velocity magnitude field during the deceleration phase of the cardiac cycle, in  $mm/s$

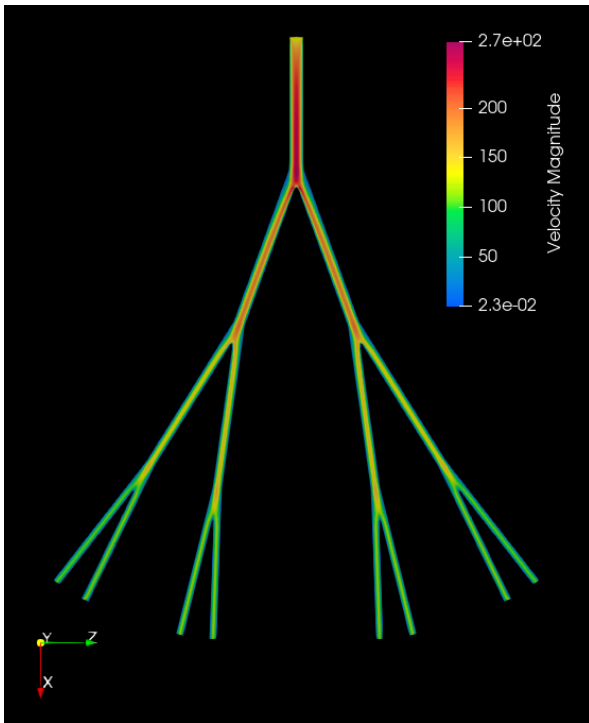


Figure B.5: Velocity magnitude field at peak diastole in the cardiac cycle, in  $mm/s$

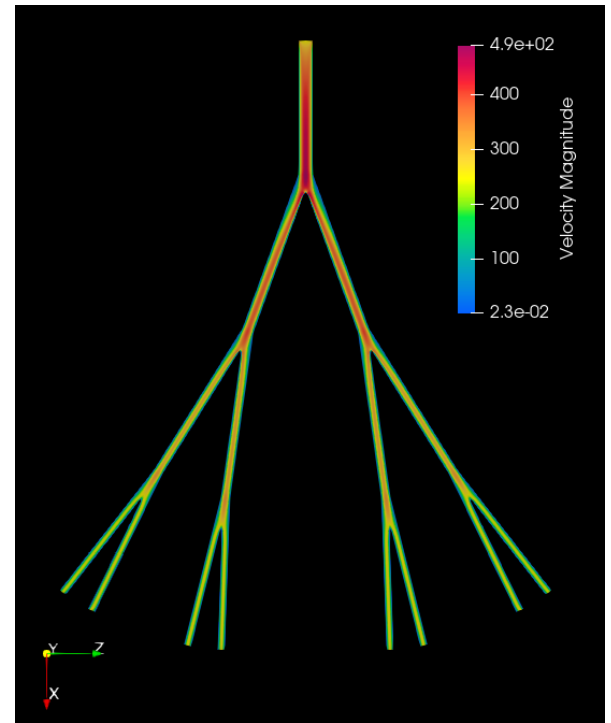


Figure B.6: Velocity magnitude field at the end of the cardiac cycle, in  $mm/s$

In the figures below, the gradient fields for 4 time instances identified in figure 6.4 are given. The other 2 time instances are already given in the text. The gradient magnitude fields are scaled by the velocity magnitude.

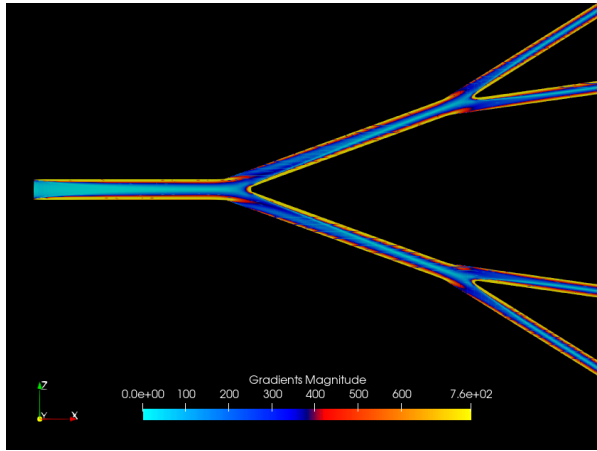


Figure B.7: Gradient magnitude field in  $1/s$  during the acceleration phase in the cardiac cycle

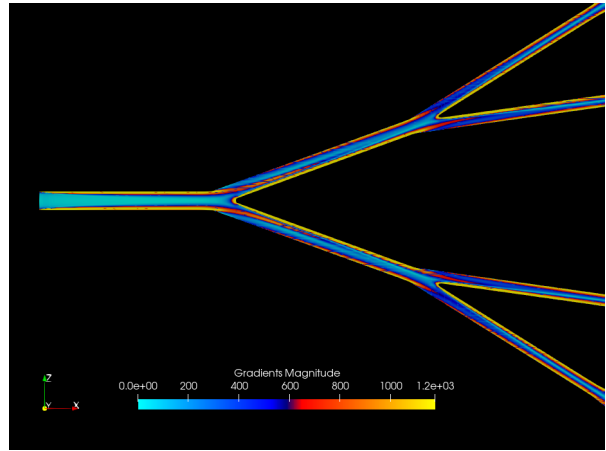


Figure B.8: Gradient magnitude field in  $1/s$  at peak systole in the cardiac cycle

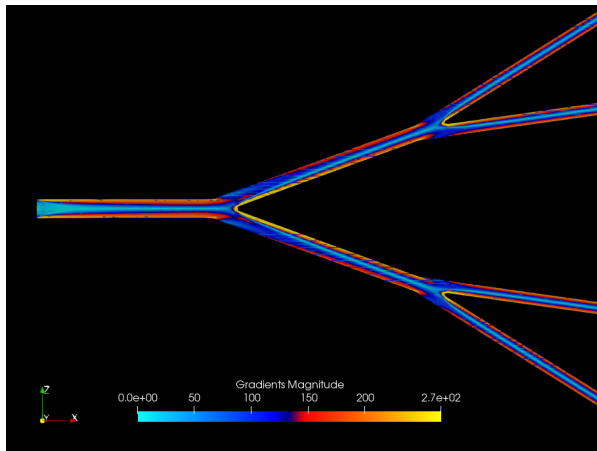


Figure B.9: Gradient magnitude field in  $1/s$  at peak diastole in the cardiac cycle

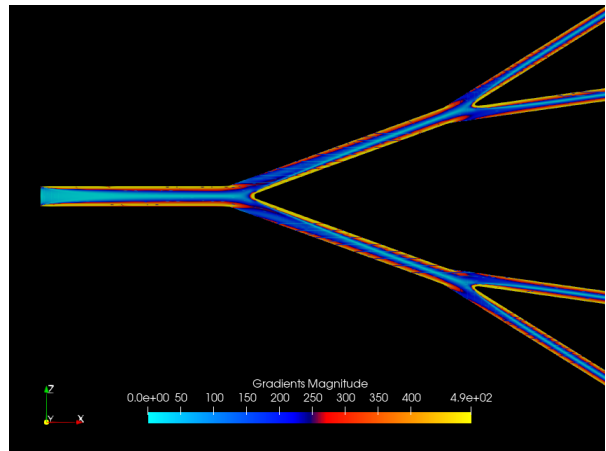


Figure B.10: Gradient magnitude field in  $1/s$  at the end of the cardiac cycle

In the figures below, the  $y$  components of the vorticity for 4 time instances identified in figure 6.4 are given. The other 2 time instances are already given in the text. The vorticity is scaled by the velocity magnitude.

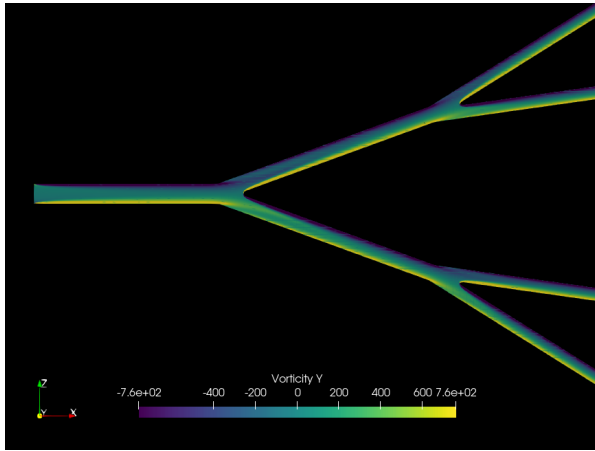


Figure B.11:  $y$  component of the vorticity field in  $mrad/s$  during the acceleration phase in the cardiac cycle

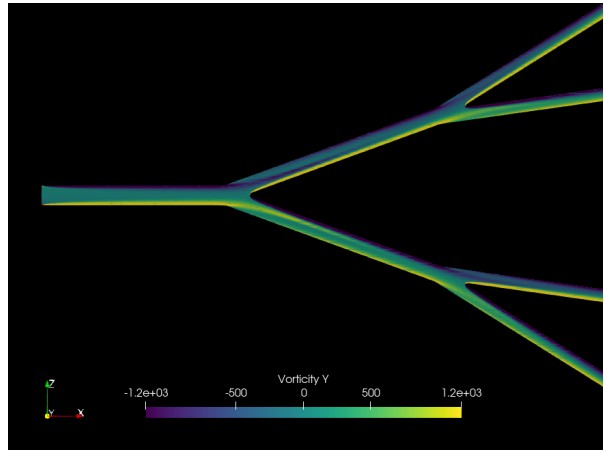


Figure B.12:  $y$  component of the vorticity field in  $mrad/s$  at peak systole in the cardiac cycle

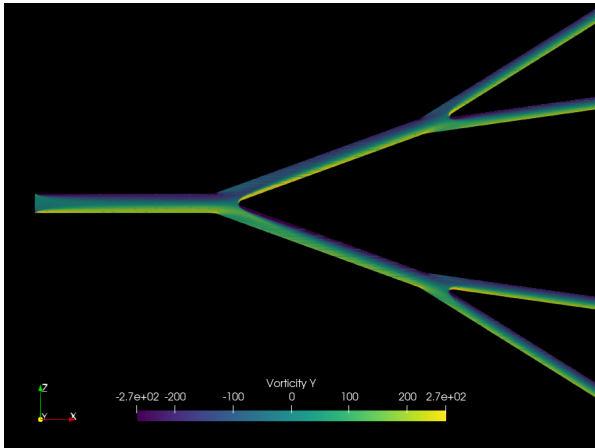


Figure B.13:  $y$  component of the vorticity field in  $mrad/s$  at peak diastole in the cardiac cycle

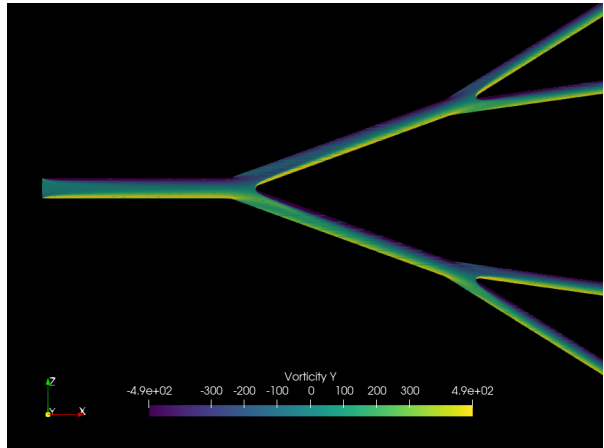


Figure B.14:  $y$  component of the vorticity field in  $mrad/s$  at the end of the cardiac cycle

## Appendix C

# Comparison to Ansys Fluent simulation results

In the figures below, a comparison between the LBM simulations and Ansys Fluent simulations performed at Ghent University can be found based on the outflows. The results are valid for the final small angle model. As can be seen in figure C.2, the outflow deviations from the average outflow are smaller in the Ansys Fluent simulations. Still, both results have quite an even flow distribution.

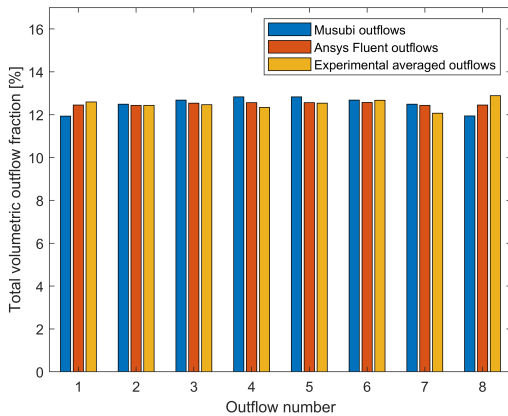


Figure C.1: volumetric outflow comparison

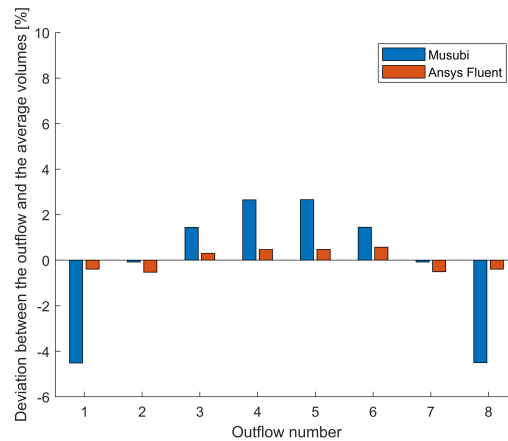


Figure C.2: Outflow deviation comparison to Ansys Fluent simulations

# Appendix D

## Catheter study: more results

In the figures below, more results from the catheter study can be found.

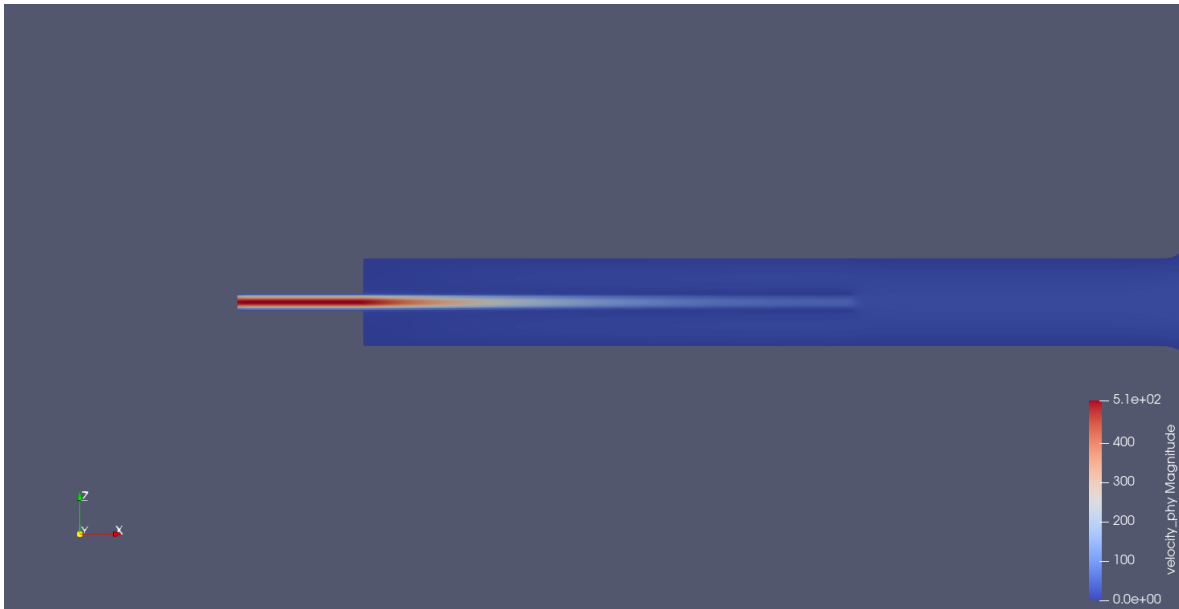


Figure D.1: Catheter observed 'leaking': velocity magnitude field in  $mm/s$

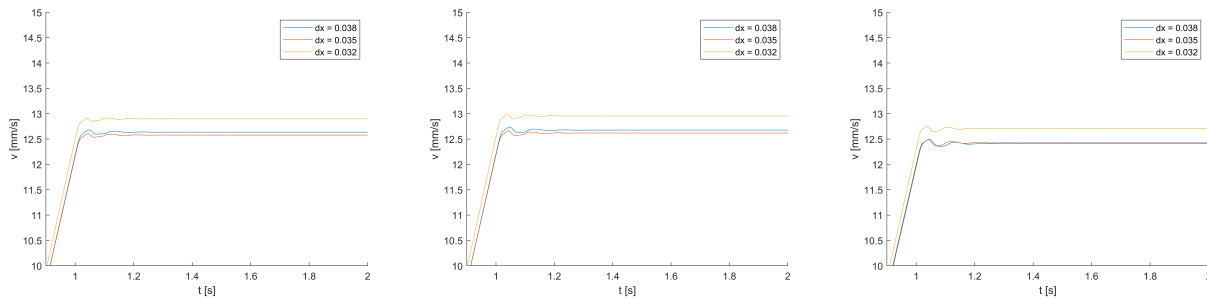


Figure D.2: Catheter velocity at probe 2 in  $mm/s$

Figure D.3: Catheter velocity at probe 3 in  $mm/s$

Figure D.4: Catheter velocity at probe 4 in  $mm/s$